UNIVERSITA' DEGLI STUDI DI PARMA

Dottorato di ricerca in Fisica

Ciclo XXVIII

Effects of cation substitutions on the physical properties of M2M1T_2O_6 pyroxenes

Coordinatore:
Chiar.mo Prof. Cristiano Viappiani

Tutors:
Chiar.mo Prof. Pier Paolo Lottici
Chiar.mo Prof. Mario Tribaudino

Dottoranda: Erica Lambruschi

Ai sogni avverati, ai sogni infranti, ai sogni presenti e a quelli futuri…

TABLE OF CONTENTS

PART 1: VIBRATIONAL PROPERTIES

PART 2: MAGNETIC PROPERTIES

Chapter I

INTRODUCTION

New materials, with higher performances and lower impact on the environment, are essential for the current developments in electronics, ceramic sciences and in material science in general. Most of the inorganic compounds, used in these fields, belong to mineral groups that are well known for most of the Earth scientists. The approaches of Earth sciences and material sciences for studying these compounds are quite different. While Earth sciences are mainly focused in understanding the geological evolution of the host rocks, material sciences research is focused on the measurement and optimization of the physical properties aiming at technological applications. In both cases, detailed characterization of the physical properties of minerals with different compositions, at different pressure and temperature conditions, is required in order to predict their behaviour and to engineer the best composition for their exploitation.

Pyroxenes are a class of minerals among the main constituents (approximately 25 wt.%) of the Earth's upper mantle, down to a depth of 400 km and occur in different types of rocks. A recently discovered phase change in pyroxenes, accompanied by a significant volume variation, is now accepted as the origin of some deep-focus earthquakes, which are clustered at a depth of approximately 225 km.

Some pyroxenes have been recently reported as a new class of multiferroic materials, which can be simultaneously ferroelectric and magnetic. The importance of this discovery is that pyroxenes will represent novel materials in the market, in which the relative ease of synthesis combines with considerable potential applications.

This project will be mainly focused on the study of the physical properties of some pyroxenes with the aim of their use as new materials for ceramic pigments and electronics applications.

In particular, pyroxenes with different distribution of cations will be studied in order to investigate:

- the stability fields of the system $CaCoGe_2O_6$-$Co_2Ge_2O_6$, in order to use the Ge-pyroxenes in ceramic processes instead of the Si-counterpart which needs high pressure synthesis. Cobalt pyroxenes are potential advanced materials in the field of ceramic pigments: Co is a good analogue of Fe, and the synthesis of Co-pyroxenes is much easier than that of Fe-pyroxenes because it does not involve the control of the oxidation process.
- the vibrational properties by Raman spectroscopy of Ca pyroxenes, $CaCoSi_2O_6$ and $CaMgSi_2O_6$, in comparison with the Ge-analogues, to monitor the effect of tetrahedral substitution both at room and high pressure;
- the vibrational properties by Raman spectroscopy of Ca pyroxenes with Ge^{4+} in (tetrahedral) T site, but different cations in (octahedral) M1 site;
- the magnetic properties of the $CaCoSi_2O_6$-$Co_2Si_2O_6$ system at different Co content. The investigations planned for Co-pyroxenes will clarify the effect of the magnetic properties related to the Co in the structure and the magnetic interactions between the octahedral chains.

Below, the working plan:

- ✓ Synthesis of crystal powders of pyroxenes along the compositional join $CaCoGe_2O_6$-$Co_2Ge_2O_6$, (in collaboration with the University of Salzburg). Structural characterization by to X-ray powder diffraction and Rietveld refinement. Comparison of the room pressure phase diagrams with those already available for $CaCoSi_2O_6$-$Co_2Si_2O_6$ join.
- ✓ Study the vibrational properties by means of Raman spectroscopy.
- ✓ Characterization of the magnetic properties of $CaCoSi_2O_6$-$Co_2Si_2O_6$ pyroxenes (in collaboration with the University of Salzburg) by means of SQuID measurements.

Chapter II

PYROXENES

2.1 Nomenclature

The pyroxenes are a group of important rock-forming inosilicate minerals found in many igneous and metamorphic rocks. They make up almost 25% by volume of some mineralogical models of the Earth's upper mantle to a depth of 400 km (Ringwood, 1975).

The name comes from the Greek words for fire (πυρ) and stranger (ξένος), because pyroxenes are present in volcanic lavas.

The chain silicate structure of the pyroxene offers chemical flexibility thanks to the incorporation of different cations: the name of pyroxenes depends primarily on their chemical composition, within the broader families of clinopyroxenes and orthopyroxenes. The range of the possible chemical substitutions in pyroxene depends on the size of the available sites in the structure and the charge of the substituting cations.

Twenty minerals of the pyroxene family are recognized by the International Mineralogical Association (IMA) Commission on New Minerals and Mineral Names (Morimoto, 1989).

The modern pyroxene nomenclature follows the scheme adopted by Deer et al. (1978). The divisions are based on the occupancy of the M2 site (Table 2.1).

Table 2.1: major chemical subdivision of pyroxenes, from Cameron and Papike, 1981.

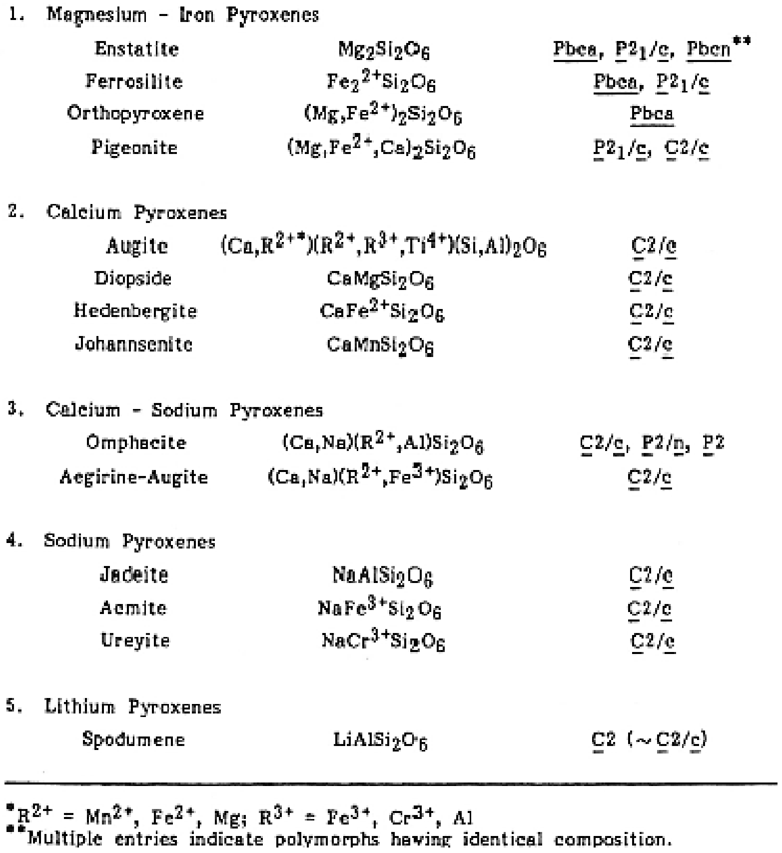

1. Magnesium - Iron Pyroxenes		
Enstatite	$Mg_2Si_2O_6$	$Pbca$, $P2_1/c$, $Pbcn$**
Ferrosilite	$Fe_2{}^{2+}Si_2O_6$	$Pbca$, $P2_1/c$
Orthopyroxene	$(Mg,Fe^{2+})_2Si_2O_6$	$Pbca$
Pigeonite	$(Mg,Fe^{2+},Ca)_2Si_2O_6$	$P2_1/c$, $C2/c$
2. Calcium Pyroxenes		
Augite	$(Ca,R^{2+*})(R^{2+},R^{3+},Ti^{4+})(Si,Al)_2O_6$	$C2/c$
Diopside	$CaMgSi_2O_6$	$C2/c$
Hedenbergite	$CaFe^{2+}Si_2O_6$	$C2/c$
Johannsenite	$CaMnSi_2O_6$	$C2/c$
3. Calcium - Sodium Pyroxenes		
Omphacite	$(Ca,Na)(R^{2+},Al)Si_2O_6$	$C2/c$, $P2/n$, $P2$
Aegirine-Augite	$(Ca,Na)(R^{2+},Fe^{3+})Si_2O_6$	$C2/c$
4. Sodium Pyroxenes		
Jadeite	$NaAlSi_2O_6$	$C2/c$
Acmite	$NaFe^{3+}Si_2O_6$	$C2/c$
Ureyite	$NaCr^{3+}Si_2O_6$	$C2/c$
5. Lithium Pyroxenes		
Spodumene	$LiAlSi_2O_6$	$C2$ ($\sim C2/c$)

*$R^{2+} = Mn^{2+}, Fe^{2+}, Mg$; $R^{3+} = Fe^{3+}, Cr^{3+}, Al$

**Multiple entries indicate polymorphs having identical composition.

Most naturally-occurring pyroxenes are described in $Mg_2Si_2O_6$ (Enstatite – En) - $Fe_2Si_2O_6$ (Ferrosilite - Fs) - $Ca_2Si_2O_6$ (Wollastonite - Wo) system and can be figured in the pyroxene quadrilateral shown in Figure 2.1. The four end-members are:

- ***Diopside $CaMgSi_2O_6$ (Di)***
- ***Hedenbergite $CaFeSi_2O_6$ (Hd)***
- ***Enstatite $Mg_2Si_2O_6$ (En)***
- ***Ferrosilite $Fe_2Si_2O_6$ (Fs).***

Since the pyroxene structure with higher amount of calcium than that of the intermediate components diopside ($CaMgSi_2O_6$) and hedenbergite ($CaFeSi_2O_6$) doesn't exist, the field of the possible compositions of pyroxenes is confined within the quadrilateral given by the end members diopside-enstatite and hedenbergite-ferrosilite. As shown in Figure 2.1, the composition of natural "quadrilateral" pyroxenes is limited by a miscibility gap between

Ca-poor and Ca-rich pyroxenes. This is due to the larger cation radius of Ca (1.0 Å), that inhibits complete solid solution.

The pyroxene quadrilateral can be characterized chemically by (Wo, En, Fs) percentages. Intermediate members of the solid solution series near the diopside-hedenbergite join are named augite or ferroaugite. All calcium pyroxenes along or near this join have *C*2/*c* symmetry; magnesium-iron pyroxenes along the base of quadrilateral are called orthopyroxenes, when have *Pbca* symmetry or pigeonite if they have $P2_1/c$ symmetry.

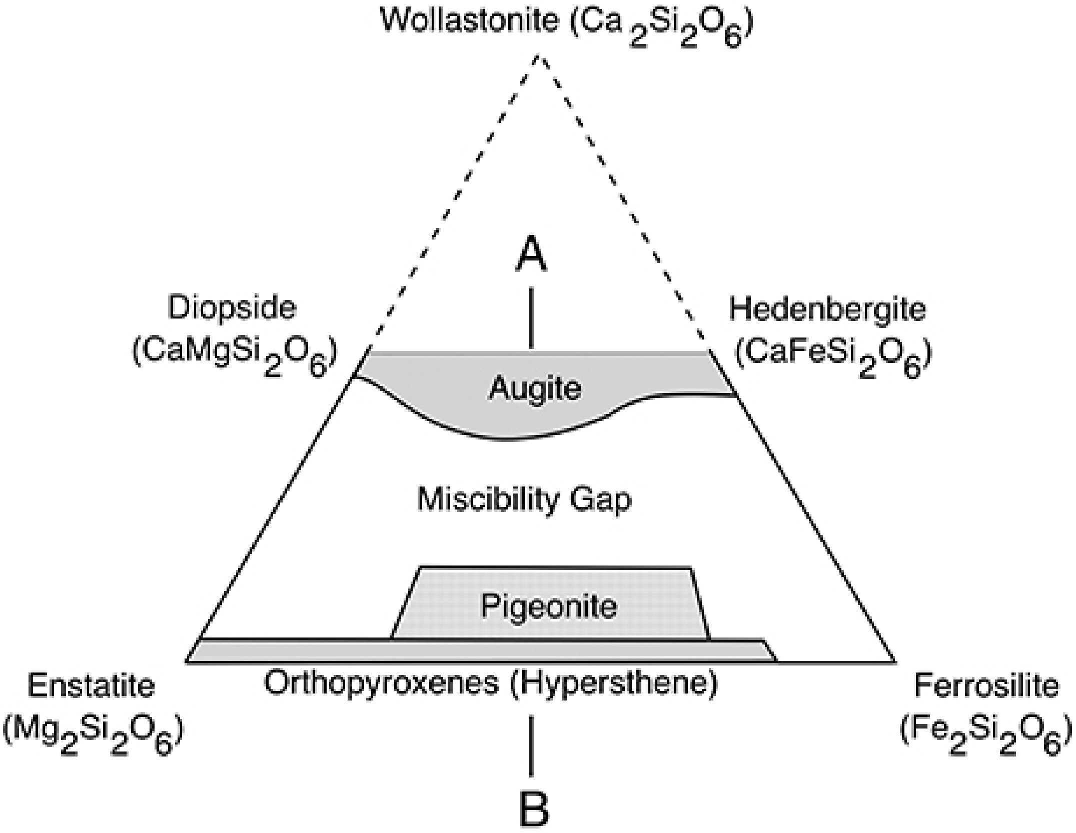

Figure 2.1: the pyroxene quadrilateral, showing the approximate compositions of common pyroxene minerals (after Brown, 1967, modified). The shaded areas represent the extent of solid solution in naturally occurring pyroxenes. At high temperature there is complete solid solution between augite and pigeonite.

A detailed investigation was done on the Di-En system (Boyd and Schairer, 1964). On the Ca rich side, it was found that monoclinic *C*2/*c* pyroxene was present. Quite complex polymorphism is found at low pressure in Ca-poorer pyroxenes, with monoclinic $P2_1/c$ and orthorhombic *Pbca* present at different temperatures and Ca content.

Along Fs-Hd join, pyroxene is present at room pressure only in the Ca richer side of the join; the orthopyroxene phase with high amount of iron is not stable at room pressure. This point explains why natural pyroxenes are generally on the Mg richer side of the quadrilateral (Lindsley and Munoz, 1969).

At higher pressure, the phase diagram strongly simplifies in both joins: only the $C2/c$, $Pbca$ and $P2_1/c$ phases are present (Mantovani, 2013) and there is larger miscibility between Ca rich and Ca poor pyroxenes.

2.2 Structure

The general formula for pyroxene can be expressed as **$\mathbf{M2M1T_20_6}$**, where M2 is the distorted 6- to 8-coordinated site populated by Na, Ca, Mn^{2+}, Fe^{2+}, Mg, Li and other transition metals, M1 site is a regular octahedral site, hosting Mn^{2+}, Fe^{2+}, Mg, Fe^{3+}, Al, Cr, Ti, Co^{2+}, Ni, Zn etc. ions and T represents Si, Al or Ge in the tetrahedral site (Figure 2.2 and 2.3). Ferric iron also enters in the tetrahedral site under certain bulk composition, temperature, pressure, and oxygen fugacity conditions.

The cations mentioned above are the most common ones in the rock-forming pyroxenes; however, other elements occur in trace amounts or as major constituents in synthetic pyroxenes. The flexibility of the chain is able to provide stable geometrical configurations with a very extensive range of cations and over a wide range of temperature and pressure conditions.

Recently, pyroxene materials with the general formula $AMSi_2O_6$ have been reported as multiferroic materials. This family of materials, where A may be an alkali or alkaline-earth element, M various metals with valence state 2+ or 3+ and Si^{4+} can be replaced by Ge^{4+} , provides a large playground for physicists in condensed matter, due to the presence of chains of octahedra that can show magnetic interactions, and has indeed attracted much attention. These synthetic materials exhibit interesting properties such as $NaTiSi_2O_6$ and $LiVGe_2O_6$ (Nénert et al., 2009), and may be tailored in order to achieve particular physical properties.

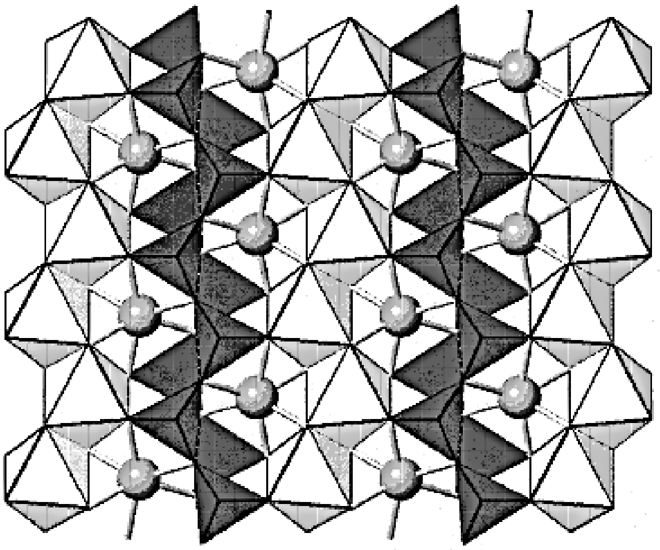

Figure 2.2: the structure of a pyroxene along a axis. M1 atoms are shown as white octahedra. TO_4 tetrahedra are dark gray. M2 atoms shown as gray spheres bonded in six positions. Oxygen atoms are at the apices of each of the polyhedra. This figure shows the connectivity of the atoms in a pyroxene (from Pommier, 2003).

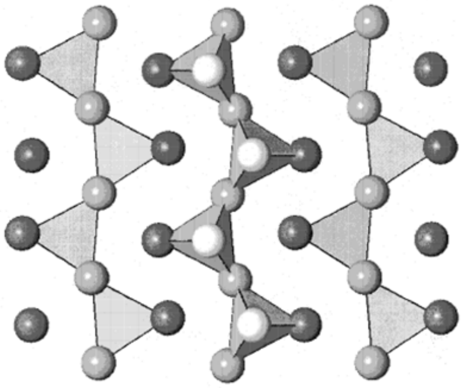

Figure 2.3: tetrahedral chains and oxygens along a axis. TO_4 tetrahedra are linked by O3 atoms (medium gray spheres). Apical O1 atoms are shown as white spheres. O2 atoms are shown as dark gray spheres. This figure displays the positions of the symmetrically nonequivalent oxygen atoms in relation to the chains (from Pommier, 2003).

The structure of all pyroxenes can be ideally described in terms of alternating tetrahedral and octahedral layers that lie parallel to the (100) plane. Within the tetrahedral layer, each T tetrahedron shares two corners with adjacent tetrahedra to form infinite chains parallel to the *c* axis (Figure 2.2) and defining the *c* parameter of the unit cell (~ 5.2 Å) (Figure 2.4).

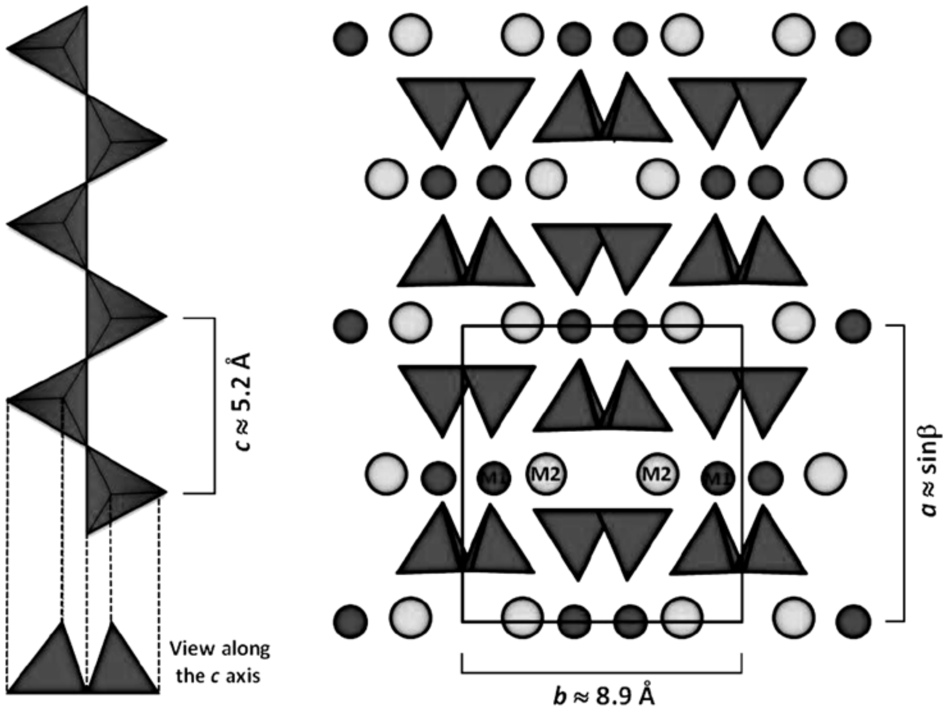

(a) **(b)**

Figure 2.4: (a) the pyroxene chain extending along the a axis; below, the chain viewed along the c axis. (b)The arrangement of TO$_4$ chains and M sites in the monoclinic C2/c pyroxene, viewed along c axis (from Putnis, 1992).

The base of each tetrahedron lies approximately in the (100) plane and the repeat unit in each chain consists of two tetrahedra with the formula $(TO_3)^{-2}$. The tetrahedra within a single chain point in the same direction, marked by the O1 oxygen at the tetrahedral vertex, and the bases of all tetrahedra within a chain lie approximately onto the plane formed by the two O3 bridging oxygen and the O2 non bridging oxygen (Burnham et al., 1967). The angle formed by the bridging oxygens (O3-O3-O3°) is called “kinking” angle.

The octahedral layer contains 6- to 8-coordinated M cations. The cation positions in pyroxenes are M1 and M2 site. M1 sites, smaller and more regular octahedra, lie between the apices of opposing tetrahedra (view along *c* axis) (Figure 2.4); M2 sites, larger and more distorted with 6 or 8 coordination, lie between their bases. The M sites form edge-sharing chains which run parallel to the silicate chains: this structure determines the magnetic and electric properties, when M site is occupied by transition metals.

The *b* axis repeat of pyroxene (~ 8.9 Å) corresponds to the distance of two tetrahedral chains on the same layer pointing on the same direction. The *a* axis is the distance of corresponding tetrahedra in a direction normal to the *b* axis. The layers of tetrahedral chains onto (100) are stacked, and shifted to each other, so that the angle between *a* and the chain direction, i.e. *c* axis, is between 100 and 110°. In clinopyroxenes this corresponds to the β angle (Mantovani, 2013).

The different symmetries among the various structure types are a result of different stacking sequences of the octahedral layers and/or of symmetrically-distinct tetrahedral chains.

This structure is common to all pyroxenes but the arrangement of the chains and the differences within the chains originate various symmetries.

There is a variety of symmetries exhibited by pyroxenes, most notably *C*2*/c, P*2_1*/c, Pbca,* and the new discovered symmetries *Pbcn, P*2_1*/n (*Redhammer et al., 2012b), and *P2/cn* and pyroxenes appear to undergo phase transitions between these various symmetries.

Clinopyroxene structure

Figures 2.4 and 2.5 show the structure of the monoclinic *C*2/*c* pyroxene. The orientation and repeat of the *a* axis is 9.7 Å. The unit cell is monoclinic and the β angle is ~ 106°. Ideally the chains are identical and are symmetrically related. There is C-centring of the (100) face of unit cell and a diad axis through the M1 and M2 sites. The way the silicate chain links to cation polyhedral is important in order to understand its behaviour to changes in composition, temperature and pressure.

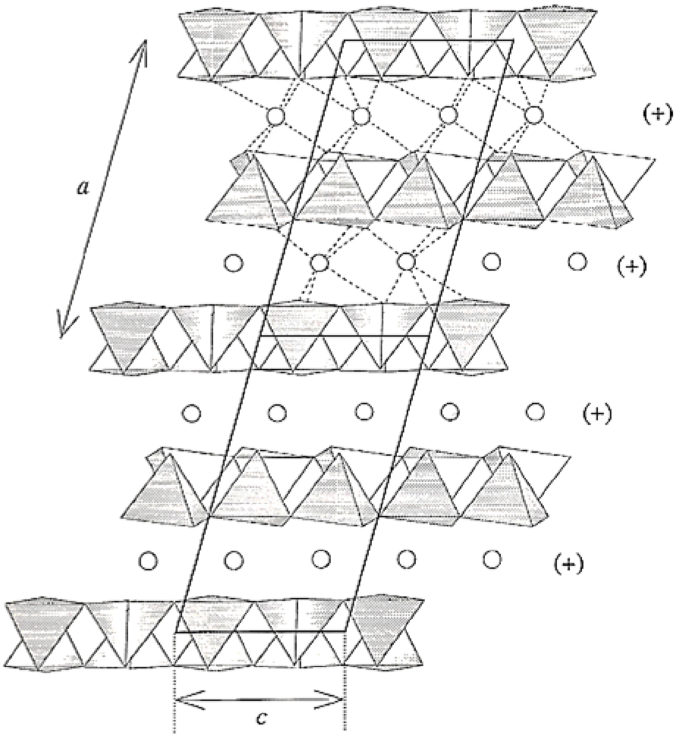

Figure 2.5: view of the clinopyroxene structure C2/c along the b axis. The chains form layers parallel to (100) planes. These layers are staggered along the c axis giving the monoclinic unit cell (two unit cells). The octahedral are oriented in the same direction (Putnis, 1992).

The size of the tetrahedron remains the same over a wide temperatures and pressure range, while M site expands and contracts significantly, and so the chain must change its length to accommodate it. The chain can be completely straight but a change in sizes of the octahedra causes the rotation and shortening of the chain length. Alternate tetrahedra always rotate in opposite senses, but there are only two rotations possible: O-chain and S-chain. In the *C*2/*c* structure the chains are all equivalent by symmetry and O-rotated (Putnis, 1992). This structure is found in the diopside $CaMgSi_2O_6$ – hedenbergite $CaFeSi_2O_6$ solid solution.

If adjacent chains are not of the same type they lose their equivalence and the symmetry is reduced (Figure 2.6). This occurs in $P2_1/c$ pyroxenes, in response to a decrease in the size of the M2 cation.

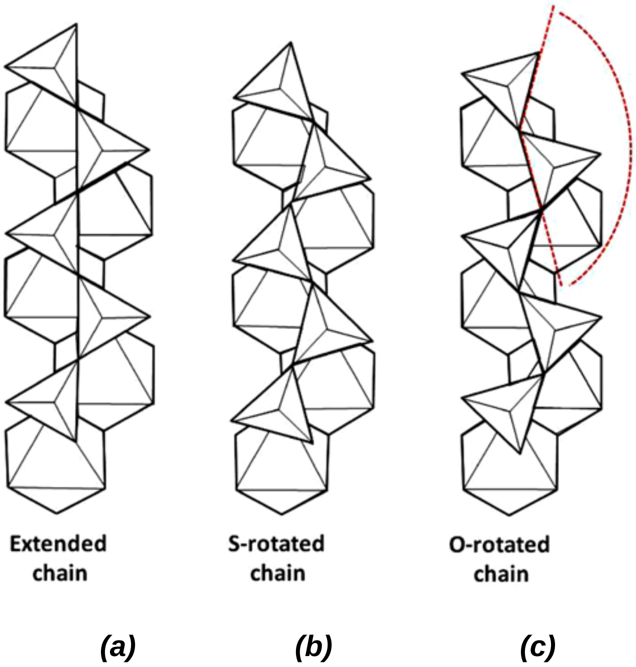

Figure 2.6: the linkage between a single TO_4 chain and a chain of octahedra along a axis: (a) extended chain; (b) and (c) when the octahedra become smaller, the tetrahedral chains shorten by rotation of the individual tetrahedra to achieve successful linkage. There are two possible rotations: S and O rotations (from Putnis, 1992).

In $P2_1/c$ (Figure 2.7) the chains are rotated in opposite sense, one S-rotated and the other O-rotated. The diad axes through the M1 and M2 sites are also lost and the symmetry is reduced, as the diad axis becomes a screw 2_1 axis.

In $P2_1/c$, however, the stacking is the same as in *C2/c* pyroxenes, and along the *a* direction all layers are stacked in the same way.

A comparison between clinopyroxenes with space groups *C*2/*c* and *P*2$_1$/*c* in (100) plane is shown in Figure 2.8.

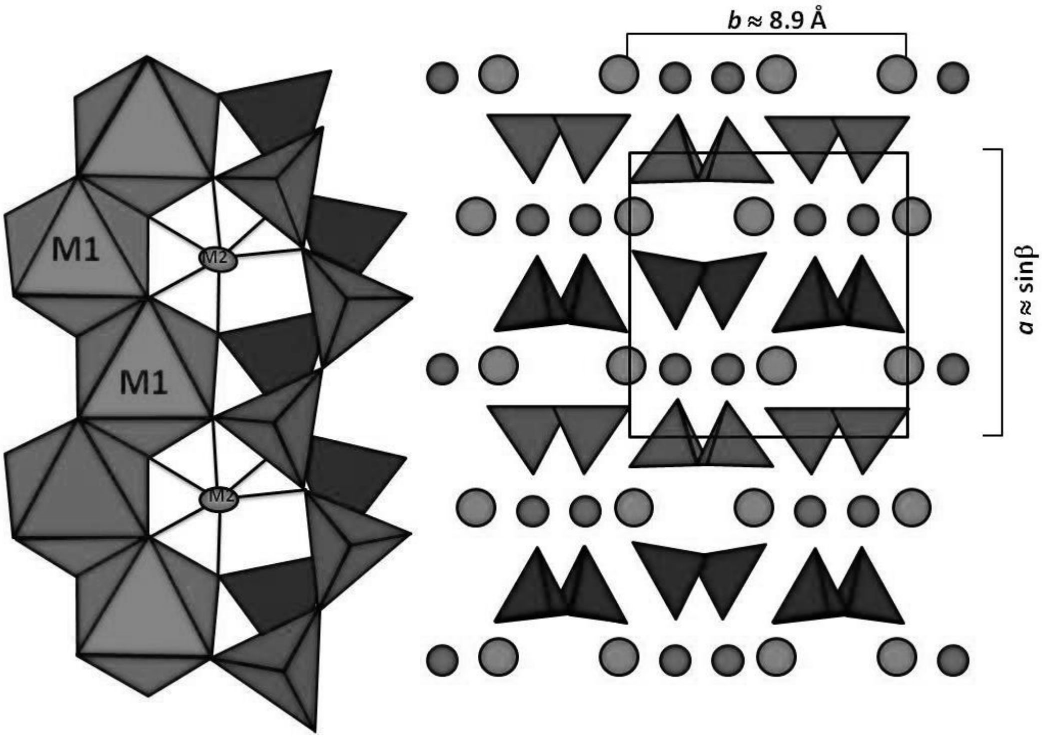

(a) (b)

Figure 2.7: representation of P2$_1$/c pyroxenes: a) light grey and dark grey represent different rotation of the two tetrahedral chain in P2$_1$/c pyroxene (S-rotated and O-rotated) along a axis; (b) projection of the structure along the c axis (from Putnis, 1992).

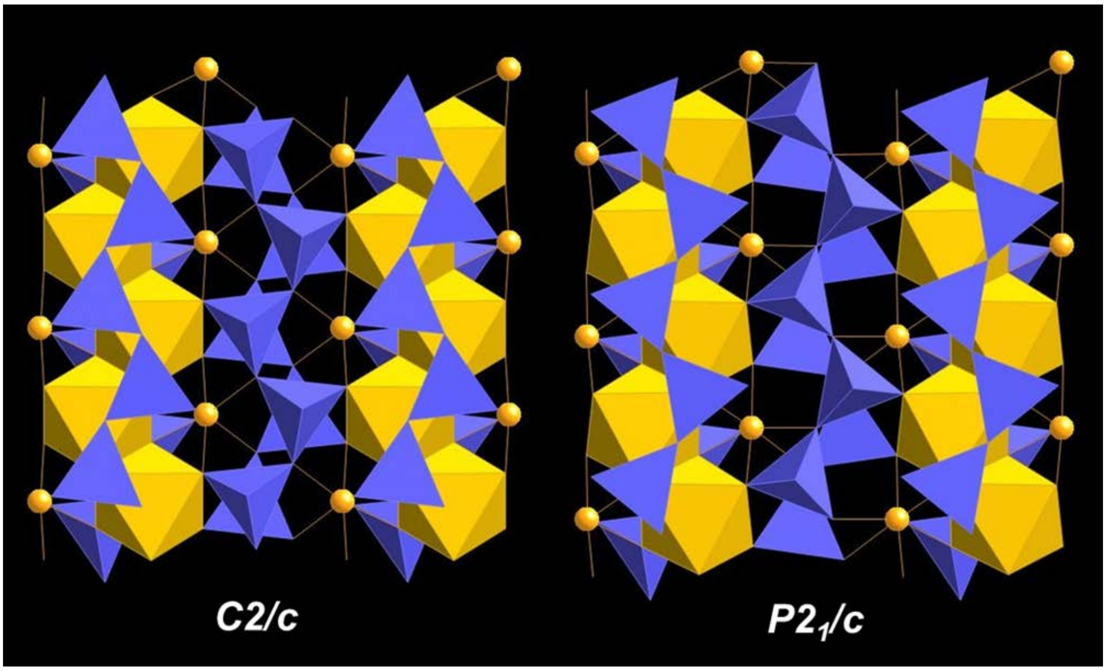

Figure 2.8: comparison between clinopyroxene with space group C2/c (left) and P2$_1$/c (right) along a axis.

Orthopyroxene structure

In pyroxenes containing no calcium and small cations in M sites, a structural reorganization is preferred.

In *Pbca* orthopyroxenes, subsequent layers are stacked in opposite directions, with the formation of a mirror plane at the unit cell scale. This results in a doubling of the unit cell (Figure 2.9).

Figure 2.10 shows a projection of the structure along the *b* axis. The unit cell is orthorhombic with the *a* lattice parameter ~ $2asin\,\beta$ relative to clinopyroxenes (Figure 2.9 a). The *b* and *c* parameters remain the same. The silicate chains are non-equivalent.

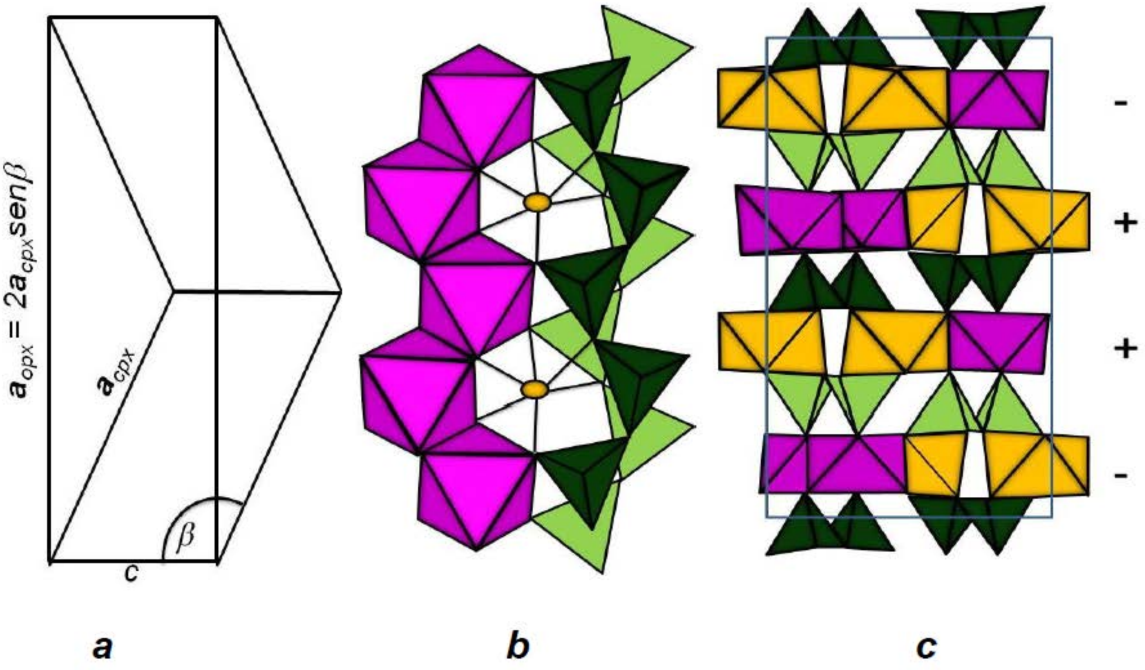

Figure 2.9: a) the relationship between the unit cells of clinopyroxene and orthopyroxene; b) view of the orthopyroxene structure and the way in which the tetrahedra links to polyhedra along a axis; c) projection along the c axis. The chain arrangement along the c axis results in non-equivalent chains, labelled A and B, and an alternation of octahedra in the + and – orientation (Putnis, 1992).

A comparison between clinopyroxene with space group *C*2/*c* and *Pbca* in (100) plane is shown in Figure 2.11.

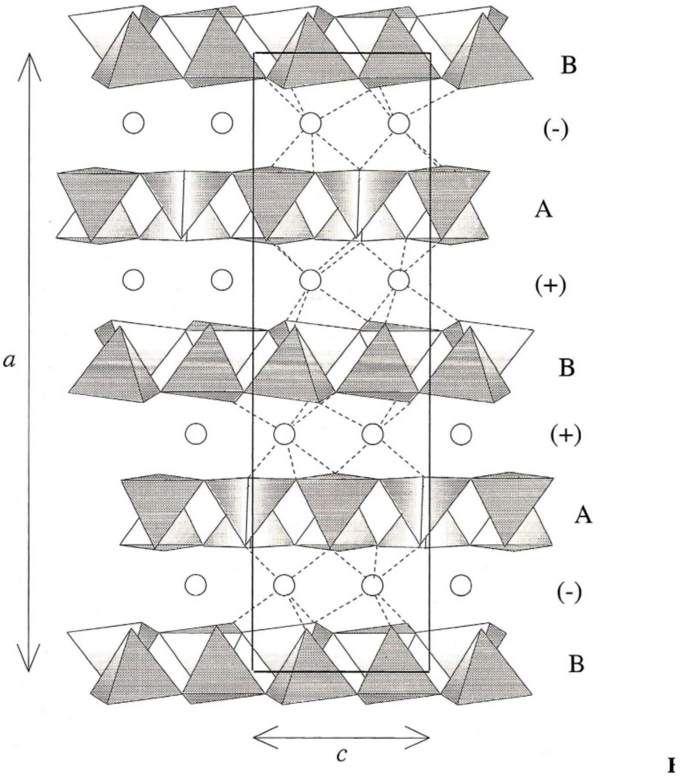

Figure 2.10: view of the orthorhombic structure Pbca along the b axis. The chains arrangement along the c axis results in non-equivalent chains, labelled A and B. One unit cell is outlined (Putnis, 1992).

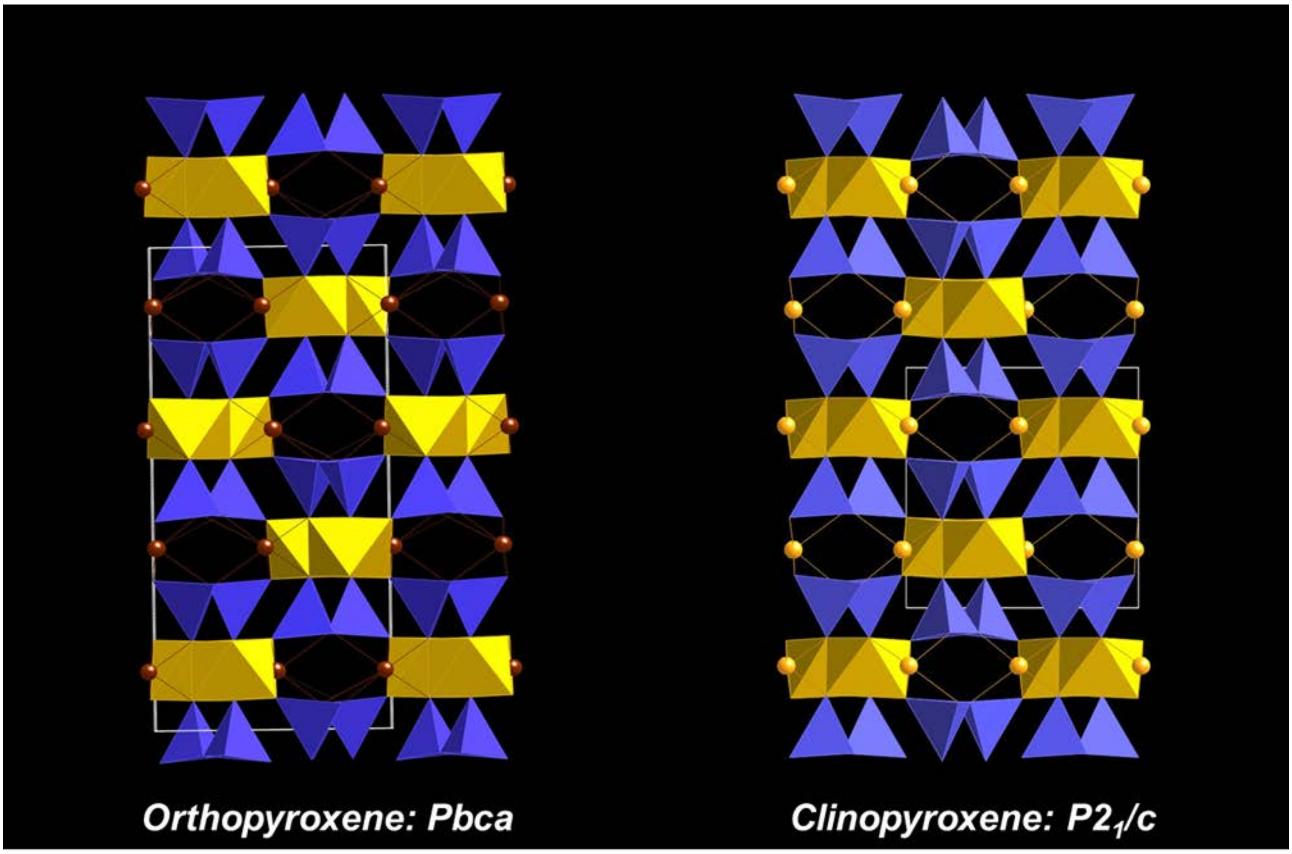

Figure 2.11: comparison between Pbca orthopyroxene and clinopyroxene with space group $P2_1/c$ along c axis.

To clarify the differences between the three most common space groups in pyroxene the *I-beam configuration* is used (Papike et al., 1973). The topological differences among the three principal structures types of pyroxenes are summarized with these diagrams, in which the structure is as tetrahedral-octahedral-tetrahedral *"I beam"* units, whose infinite dimension lies parallel to *c* axis (Prewitt, 1980) (Figure 2.12). In each I-beam, two tetrahedral units point inward and are cross-linked by octahedrally-coordinated cations. The symbols within the I-beam units provide information on the symmetry and orientation of individual coordination polyhedra. The A's and B's of the tetrahedral layers refer to two symmetrically-distinct chains: that is, chains that are kinked by different amounts and/or those whose tetrahedra are distorted differently. The absence of this notation indicates that the chains in adjacent layers within one I-beam unit are symmetrically equivalent and are related to 2-fold axes of rotation parallel to *b*. The O or S notation within the tetrahedral layers refers to the rotational aspect of the chains (Cameron and Papike, 1981). This configuration explains also better the M1 position. The + or – depend on the orientation of the octahedra between the chain apices. Viewed along the *c* axis, the octahedra can have a triangular face pointing downwards (+) or upwards (-) depending on the relative position of the chains along their length.

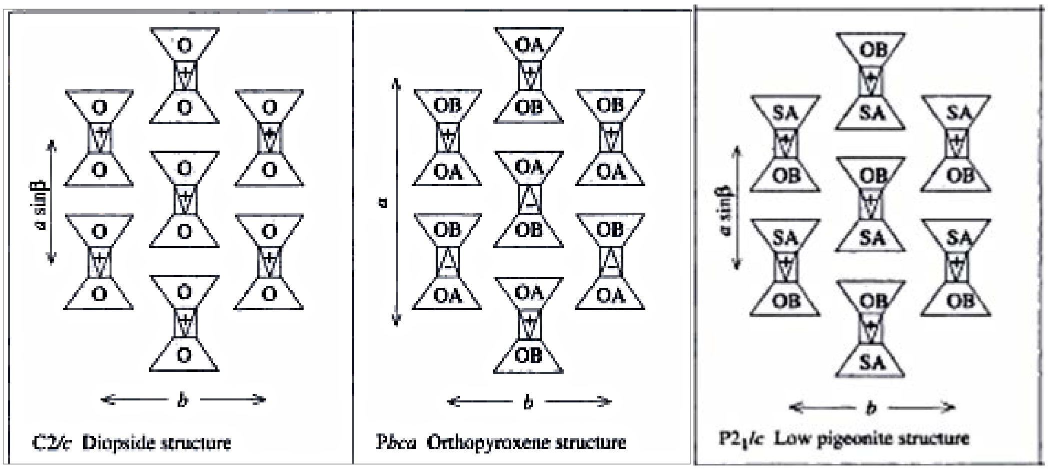

Figure 2.12: I-beam diagrams for the common pyroxene structures along c axis. O and S refer to the rotations of the tetrahedral chain. The orientations of the octahedra are labelled + and -, and A and B refer to non-equivalent chains (from Cameron and Papike, 1981).

Chapter III

THE $CaCoGe_2O_6$-$CoCoGe_2O_6$ SYSTEM

Cobalt-based ceramic pigments are widely used for coloured glazes in the ceramic industry, for wall or floor wares, and also for the bulk coloration of unglazed stoneware. The main characteristic of Co-based pigments is a high resistance with respect to light, environment, high temperature and chemical agents. Clinopyroxenes have a potential as ceramic colorants, since their crystal structure is highly stable to leaching and is able to accommodate transition metal ions at the M1 site, where they can play as chromophores. Therefore, cobalt based phases like Ca,Co-pyroxenes are interesting candidates, particularly because they can host a lower cobalt content with respect to the commonly used Co-olivine Co_2SiO_4 and spinel $CoAl_2O_4$ maintaining a bright pink color (Mantovani et al., 2015). In a previous study of the system $CaCoSi_2O_6$ - $CoCoSi_2O_6$, the stability along the join was achieved by high pressure, whereas at low pressure there wasn’t solid solution. For this reason, our intention was to try to synthesize the analogues system but with germanium in T site, because germanates behave as high-pressure models for corresponding silicates. It is expected that in Ge-pyroxene solid solution can be obtained at room conditions. In the corresponding Si-pyroxenes, solid solution was observed only very close to the $CaCoSi_2O_6$ end member. The knowledge about regularities of the structure of silicates can be substantially expanded by an investigation on germanium-containing analogues. Even if germanium is more expensive than silicon for ceramic industry, the easier synthesis and the better stability of Ge-pyroxenes can be helpful. Furthermore, the cobalt end member, with germanium in T site, could be tested as colorant.

3.1 Ge and Si pyroxenes: crystallographic similarities and differences

Synthetic pyroxenes with Ge in the T site have several points of interest. First, germanates have been studied for a long time as model systems for lower crust and upper mantle high-pressure silicate minerals. Both silicon and germanium form tetravalent ions that possess similar outer electronic structures and radii (Si^{4+} 0.42 Å, Ge^{4+} 0.49 Å), and as a consequence, there is a wide similarity in chemical and physical properties like polymorphism and chemical bonding of the corresponding phases with Ge and Si in the tetrahedral site. Accordingly, the crystal chemistry of silicates is very closely related to that of germanates, particularly for oxy-compounds, and corresponding silicates and germanates are usually isostructural. The advantage for germanates is that they can be synthesized at room or lower pressure than the corresponding high-pressure silicates, enabling studies that would be experimentally too demanding for the corresponding silicates. These relationships were first elucidated in a paper by Goldschmidt (1931).

In this paragraph the crystallographic differences between Ge and Si pyroxenes will be discussed.

In Table 3.1 the cell parameters for Ge and Si pyroxenes are reported.

Table 3.1: cell parameters for some Si and Ge pyroxenes. If the error is present, it is reported in brackets.

Sample	**a (Å)**	**b (Å)**	**c (Å)**	**β(°)**	**V (Å^3)**
[1]**$CaCoGe_2O_6$ *C2/c***	10.1531(3)	8.9772(3)	5.429(1)	104.888(2)	478.23(3)
[2]**$CoCoGe_2O_6$ *C2/c***	9.67315()	9.00294(6)	5.17437(4)	101.313(6)	441.895(5)
[3]**$CoCoGe_2O_6$ *Pbca***	18.8336(2)	9.0220(7)	5.3762(4)	90	910.5(1)
[4]**$CaMgGe_2O_6$ *C2/c***	10.1222(6)	8.9858(5)	5.4326(5)	105.2548(6)	476.72(5)
[5]**$MgMgGe_2O_6$ *C2/c***	9.6010(8)	8.9323(6)	5.1592(5)	101.034(9)	434.27
[6]**$MgMgGe_2O_6$ *Pbca***	18.8099(12)	8.9484(8)	5.3451(4)	90	899.68)
[7]**$CaFeGe_2O_6$ *C2/c***	10.1787(3)	9.0549(3)	5.4322(1)	104.265(1)	485.22
[8]**$FeFeGe_2O_6$ *C2/c***	9.7993(2)	9.1491(2)	5.1991(1)	101.891(2)	456.12(8)
[9]**$CaMnGe_2O_6$ *C2/c***	10.2665	9.1659	5.4653	104.2150	498.55(5)
[10]**$MnMnGe_2O_6$ *Pbca***	19.2864(2)	9.2548(1)	5.4782(1)	90	977.81(2)
[11]**$MnMnGe_2O_6$ *C2/c***	9.9138(10)	9.2733(10)	5.2738(6)	101.66(1)	474.84(8)
[12]**$CaNiGe_2O_6$ *C2/c***	10.1068	8.9539	5.4100	105.3239	472.17(8)

[13]$CaZnGe_2O_6$ *C2/c*	10.1659(8)	9.0096(7)	5.4369(4)	105.181(4)	480.59(6)
[14]$CaCoSi_2O_6$ *C2/c*	9.802(1)	8.962(1)	5.249(1))	105.40(1)	444.54(3)
[15]$CoCoSi_2O_6$ $P2_1/c$	9.650(3)	8.929(2)	5.220(1)	108.84(2)	424.3(1)
[16]$CoCoSi_2O_6$ *Pbca*	18.298(2)	8.921(2)	5.203(1)	90	849.4(1)
[17]$CaMgSi_2O_6$ *C2/c*	9.746(4)	8.899(5)	5.251(6)	105.63(6)	438.6(3)
[18]$CaMgSi_2O_6$ HT-*C2/c*	8.822(4)	9.081(1)	5.285(3)	105.98(3)	453.2(5)
[19]$MgMgSi_2O_6$ $P2_1/c$	9.6205	8.8255	5.1885	108.333	418.09
[20]$MgMgSi_2O_6$ HP-*C2/c*	9.201(3	8.621(1)	4.908(	101.5 0(3	381.5(2)
[21]$MgMgSi_2O_6$ *Pbca*	18.216(2)	8.813(1)	5.179(1)	90	831.42
[22]$CaFeSi_2O_6$ *C2/c*	9.8450(9)	9.0293(8)	5.2450(5)	104.775(7)	450.83
[23]$FeFeSi_2O_6$ $P2_1/c$	9.7075(5)	9.0807(4)	5.2347(5)	108.46(1)	437.70(6)
[24]$FeFeSi_2O_6$ *Pbca*	18.418(2)	9.078(1)	5.196(1)	90	837.47
[25]$FeFeSi_2O_6$ HP- *C2/c*	9.540(1)	8.996(3)	5.008(1)	103.01	418.8(2)
[26]$CaMnSi_2O_6$ *C2/c*	9.978(9)	9.156(9)	5.293(5)	105.48(3)	446
[27]$CaNiSi_2O_6$ *C2/c*	9.734(2)	8.891(2)	5.228(1)	105.87(2)	435.21(1)
[28]$CaZnSi_2O_6$ *C2/c*	9.7955(8)	8.9781(8)	5.251(6)	106.033(7)	443.8(5)

[1] *Present data*
[2,3] *Redhammer et al., (2010)*
[4] *Personal communication from Redhammer*
[5,6] *Ozima M., (1983)*
[7] *Redhammer et al., (2013)*
[9,12,27] *Redhammer et al., (2008)*
[8] *Redhammer et al., (2012)*
[10,11] *Redhammer et al., (2011)*
[13,28] *Redhammer and Roth, (2005)*
[14,15,16] *Mantovani, (2014)*
[17] *Clark et al., (1969)*
[18] *Cameron et al, (1973)*
[19] *Morimoto et al., (1960)*
[20,25] *Hugh-Jones et al., (1994)*
[21] *Hawthorne and Ito, (1977)*
[22] *Redhammer et al., (2006)*
[23] *Burham, (1965)*
[24] *Sueno et al., (1976)*
[26] *Freed and Peacor, (1967)*

A characteristic behaviour of the germanium system is that, along the clinopyroxene join, the evolution of β angle has an opposite trend with respect to corresponding silicate clinopyroxenes. When the amount of calcium decreases in the M2 site, in Si-pyroxenes the beta angle increases for the chemical substitution, towards a HT-*C*2/*c* structure. The HT-*C*2/*c* structure is not reached at the end member at room pressure, with the exception of ZnSiO$_3$ pyroxene, because a transition from *C*2/*c* to *P*2$_1$/*c* is observed at lower Ca content. In Ge clinopyroxenes the β angle decreases and the symmetry remains *C*2/*c,* changing towards the HP-*C*2/*c* structure (Figure 3.1).

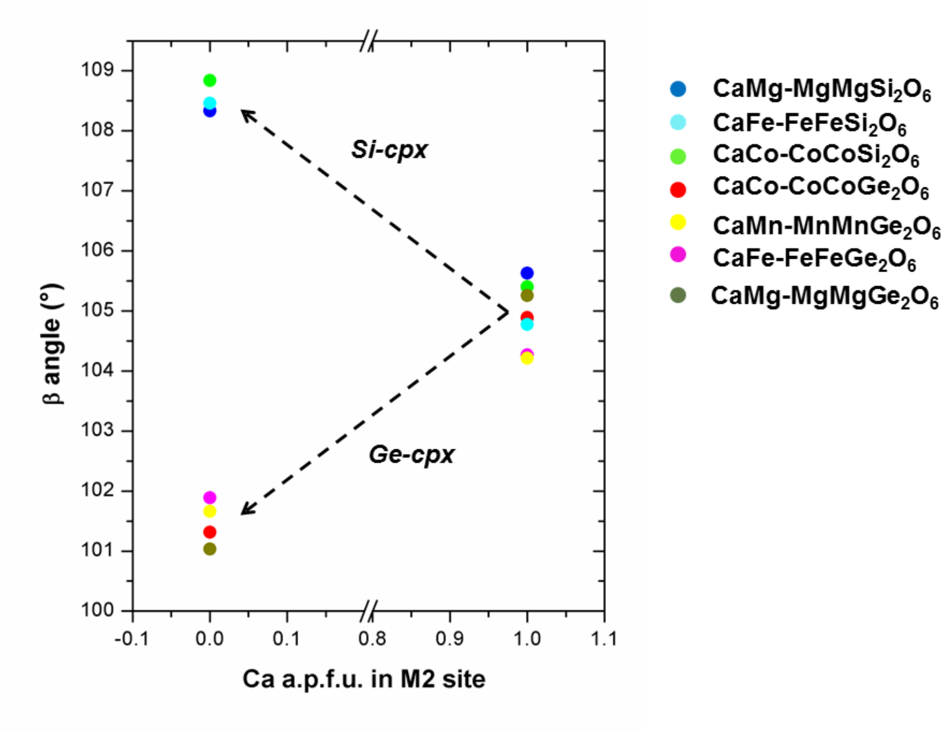

Figure 3.1: trend of β angle (°) vs Ca a.p.f.u. in M2 site of some clinopyroxenes.

When calcium is in the M2 site, Ge clinopyroxenes have smaller β angle and higher volume (Figures 3.2-3.3).

In Ca poor clinopyroxenes, the differences are more significant: the Si-clinopyroxenes have *P*2$_1$/*c* structure and the beta angle has a value around ~ 108°. The Ge clinopyroxenes have space group *C*2/*c* and β ~ 101°, as the HP- *C*2/*c* structure of Si-clinopyroxenes.

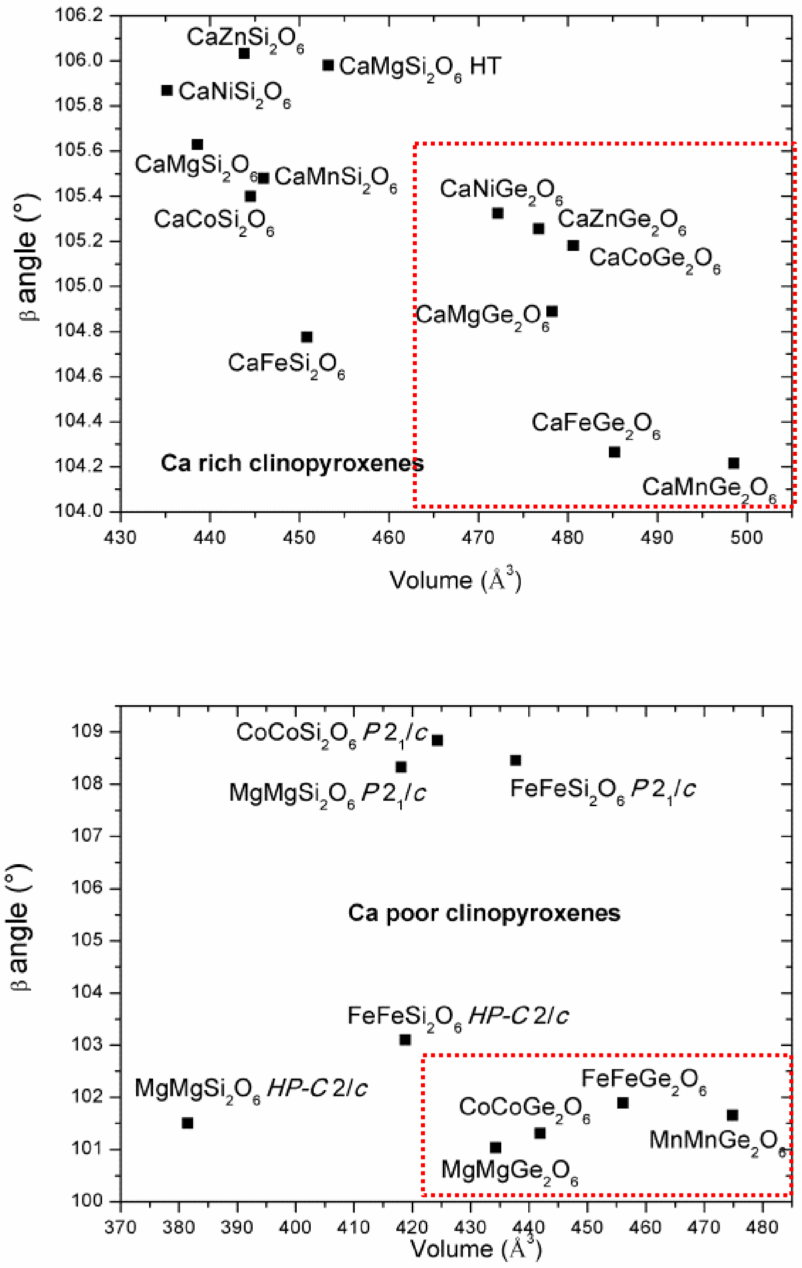

Figure 3.2: trend of beta angle versus volume in Ca rich (up) and Ca poor clinopyroxenes (down).

In Figure 3.3 the crystallographic changes within Si and Ge pyroxenes are summarized, highlighted by the changes in cell volume vs β angle .

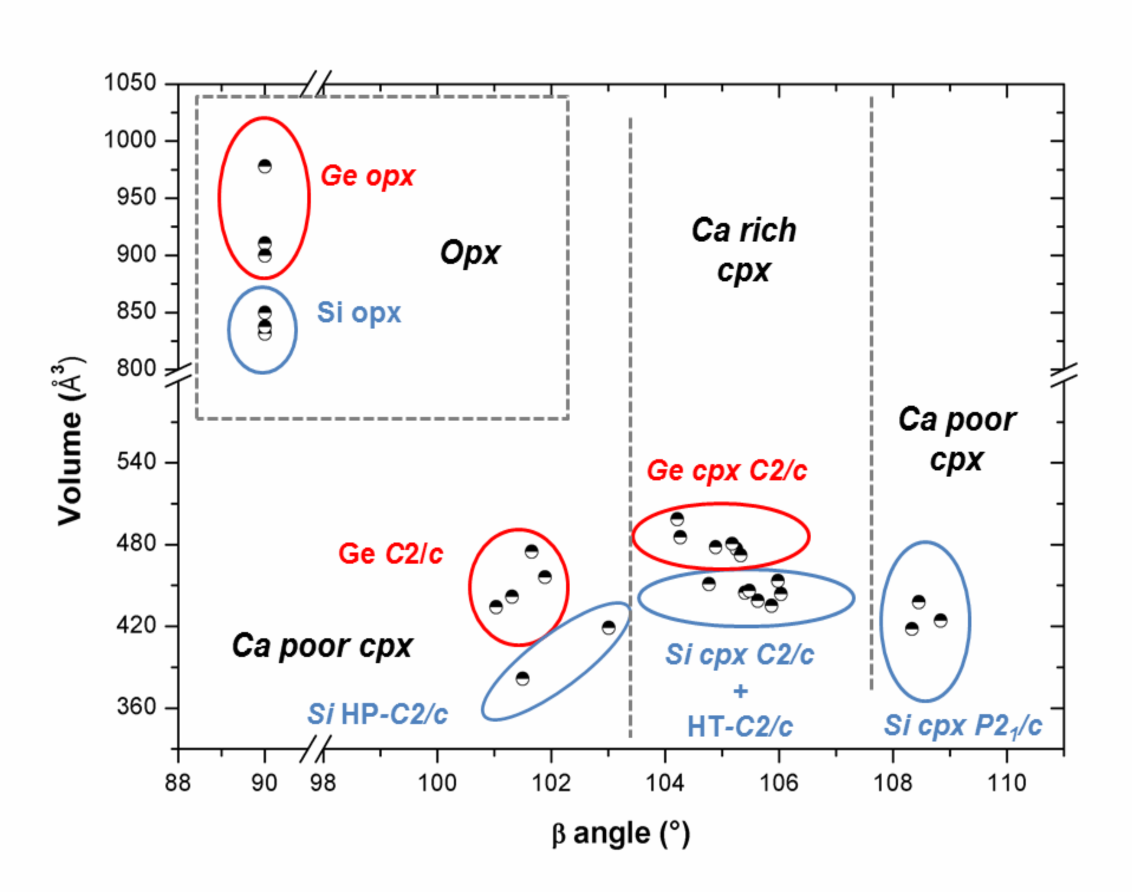

Figure 3.3: plot of volume (Å^3) vs β angle (°) for some pyroxenes.

Ca rich pyroxenes with Ge^{4+} in the T site show a crystallographic behaviour similar to the Si analogues, and the β angle has values similar to those found in the structure of HT-*C*2/*c.* In Ge system the *P*2$_1$/*c* structure is not observed, and Ca poor clinopyroxenes have β values similar to HP-*C*2/*c.*

Concerning the difference in volume between the two end-member, $CaCoSi_2O_6$ and $CoCoSi_2O_6$, the changes in the *C*2/*c* Ca–richer pyroxenes can be modeled assuming that they are only due to the decreasing average size of the cation in the M2 site. The unit cell volume V_x for a given Ca content can then be predicted as:

$$V_x = V_{EM} - 4/3\ \pi\ Z\ (R^3_{Ca} - R^3_{Fe,\ Co,\ Mg})(1 - X_{Ca})$$

where V_{EM} is the volume of the Ca–rich end member, i.e. diopside, hedenbergite or $CaCoSi_2O_6$, Z the number of M2 sites in the unit cell (4 in *C*2/*c* and *P*2$_1$/*c*), and R_{Ca} and $R_{Fe,\ Co,\ Mg}$ the ionic radii of divalent Ca and Fe, Co and Mg (Mantovani et al., 2014), respectively. This trend predicts quite closely the changes in volume with composition, which can be modeled as linear in the *C*2/*c* field (Figure 3.4), up to the compositions close to the transition, where the observed volumes are lower than those predicted by the model.

While the above linear model is followed quite closely by Ca-richer *C*2/*c* clinopyroxenes, in the *P*2_1/*c* field the cell volume is lower than predicted. We interpret the missing volume (~ 10 Å^3) mostly as an effect of the *C*2/*c* – *P*2_1/*c* transition (Figure 3.4).

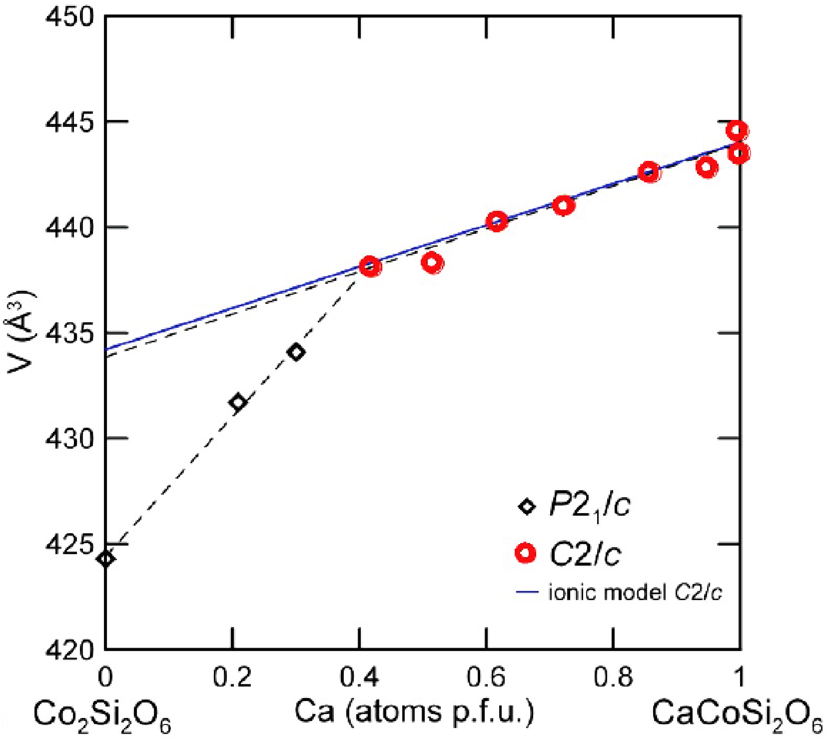

Figure 3.4: cell volume vs composition in $CoCoSi_2O_6$ - $CaCoSi_2O_6$ pyroxenes: the blue line represents the change in volume modeled by a "ionic model" (see text), red circles the experimental data for C2/c and black diamond for $P2_1/c$ pyroxenes. Best fits for C2/c and $P2_1/c$ are dashed. Figure taken from Mantovani et al. (2014).

Our germanium system has volume change of ~35 Å^3. As the cation substituted in M2 is the same, cobalt, we can use the same ionic model to predict the volume. The larger difference is now due to the different structure of the two end-members, HP and HT *C*2/*c*, and no phase transition is observed as in Si-join, in spite of the same space group.

The crystallographic changes noticed are only caused by substitution in tetrahedral sites.

In order to accommodate the large GeO_4 tetrahedra, the tetrahedral chain is distinctly more kinked in germanates (i.e. smaller O3–O3–O3 kinking angle). Additionally, the lateral size of the tetrahedral chain is decreased along *b*. Thus the additional space requirement by the Ge atoms is compensated along *b* and the *b*-lattice parameters are very similar for silicates and germanates, irrespective of the different volumes (Redhammer et al., 2008).

In Figure 3.5 are shown the three structures of pyroxenes. HT-*C*2/*c* is characterized by elongated chains while HP- *C*2/*c* has strongly kinked chains and in Ca rich pyroxenes the kinking is intermediate.

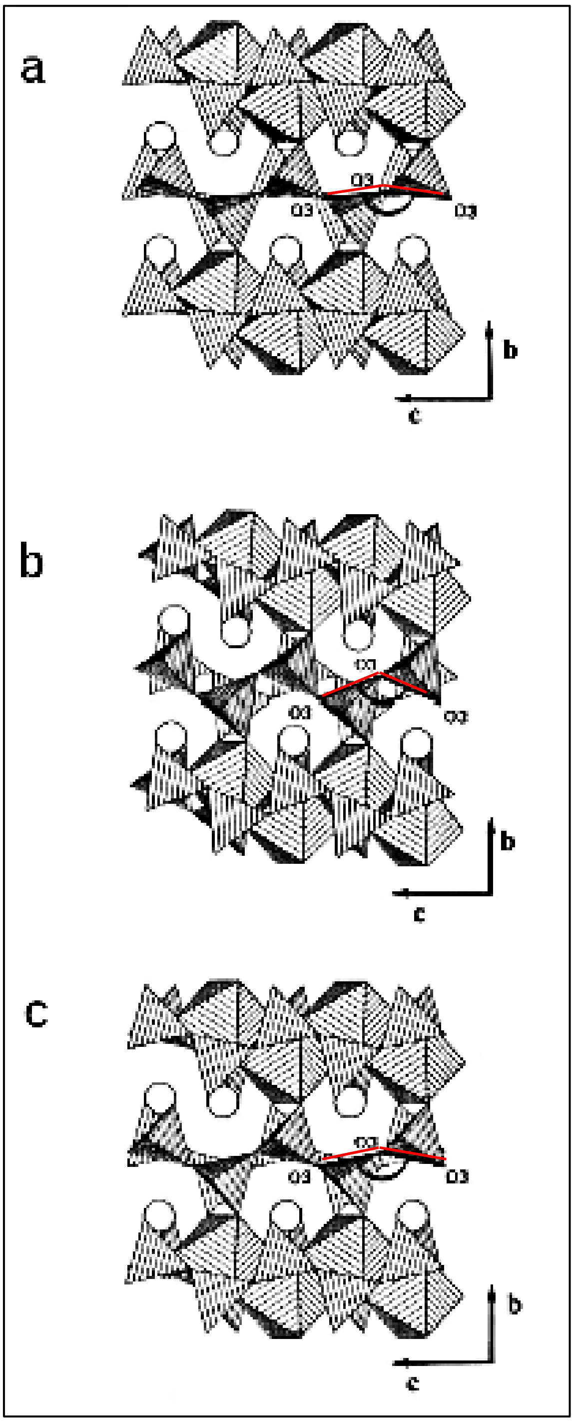

Figure 3.5: the structures of (a) the high-temperature, (b) the high-pressure, and (c) the high-Ca (or hedenbergite-like) C2lc phases of FeSiO$_3$, projected onto (100). The tetrahedral and M1 sites are shown as shaded tetrahedra and octahedra, respectively, and the M2 sites are drawn as circles. Note the variation of the (O3-O3-O3) chain kinking angle, in red, between the three structures (taken from Hugh-Jones et al., 1994).

3.2 Phase diagram of $CaCoGe_2O_6$-$CoCoGe_2O_6$ system vs Si pyroxenes by XRDP refinements

3.2.1 Sample preparation

The series of samples along the join $CaCoGe_2O_6$ – $Co_2Ge_2O_6$ was synthesized at University of Salzburg.

The process used is a traditional ceramic route, known as “solid state synthesis”, where stoichiometric ratios of oxides (GeO_2 and Co_3O_4) and $CaCO_3$ carbonate are mixed and heated in a crucible. The starting materials are powder of Co_3O_4 (black), $CaCO_3$ (white) and amorphous GeO_2 (black), prepared according to the stoichiometry $Ca_{1-x}Co_{1+x}Ge_2O_6$, where x = 0- 1with steps 0.1.

The initial compounds were weighted, mixed and crushed in an agate mortar with acetone. The powder is then reduced in pellets and heated within an alumina crucible in an electric furnace in air, under ambient pressure and ambient oxygen fugacity.

The heating system increased the temperature with a rate of 200 °C/h up to the desired temperatures of 1050 °C, 1200 °C and 1250 °C and then the samples were annealed for the selected time. At these temperatures, reduction of Co^{3+} to Co^{2+} and decarbonation occur quickly. After a sintering time of 2 days, the sample materials were reground, pressed and reheated. This procedure was repeated 3 times for samples at 1050 °C, 2 times for 1200 °C and one for the final temperature.

The reaction that occurs in the furnace is:

$$1/3\ Co^{2+}Co^{3+}{}_2O_4 + CaCO_3 + 2\ GeO_2 \leftrightarrow CaCoGe_2O_6 + CO_2 + 1/6\ O_2$$

The reaction is a typical oxidation/reduction, and in particular Co^{3+} at temperature > 1000 °C becomes Co^{2+}, avoiding the use of a reducing atmosphere (Mantovani et al., 2015).
The final quenching is done by turning off the power and cooling the samples in air. Then the samples were crushed in order to obtain a powder.

The samples made at each temperature are listed in Table 3.2.
The samples are labelled according to a.p.f.u. *10 of cobalt in M2 site and their heating temperature: for instance, Co6 1050 means that the starting material has a bulk composition of $Ca_{0.4}Co_{1.6}Ge_2O_6$ with 0.6 of Co a.p.f.u. in the M2 site of a hypothetical stoichiometric pyroxene and its heating temperature is 1050 °C.

Table 3.2: list of the solid state syntheses at three temperatures.

Sample Name	**Co0**	**/**	**Co2**	**/**	**Co4**	**Co5**	**Co6**	**/**	**Co8**	**/**	**Co10**
Temperature (°C)	**1050**		**1050**		**1050**	**1050**	**1050**		**1050**		**1050**
Time of annealing (h)	280		280		280	280	280		280		280
Nominal Ca content	1		0.8		0.6	0.5	0.4		0.2		0
Sample	**Co0**	**Co1**	**Co2**	**Co3**	**Co4**	**Co5**	**Co6**	**/**	**Co8**	**Co9**	**Co10**
Temperature (°C)	**1200**	**1200**	**1200**	**1200**	**1200**	**1200**	**1200**		**1200**	**1200**	**1200**
Time of annealing (h)	78	78	78	78	78	78	78		78	78	78
Nominal Ca content	1	0.9	0.8	0.7	0.6	0.5	0.4		0.2	0.1	0
Sample	**/**	**/**	**/**	**Co3**	**Co4**	**Co5**	**Co6**	**Co7**	/	/	/
Temperature (°C)				**1250**	**1250**	**1250**	**1250**	**1250**			
Time of annealing (h)				60	60	60	60	60			
Nominal Ca content				0.7	0.6	0.5	0.4	0.3			

As the phase diagram of germanium pyroxenes is not yet known, the three temperatures were chosen following available literature on the corresponding Si-analogues (Mantovani, 2013).

In particular, the first temperature was chosen as in the $CaSi_2O_6$ – $Co_2Si_2O_6$ system, at low pressure, the clinopyroxene is stable in the temperature range 1000 °C - 1150 °C (Mantovani, 2013), whereas at 1200 °C $CaCoSi_2O_6$ shows incongruent melting (Navrotsky and Coons, 1976). So, in analogy with this system, we choose 1050 and 1200 °C to remain in subsolidus. After the examination of the samples prepared in these two runs, we noticed that, apart from the samples Co0 1050 and Co0 1200, grains of different colours (pink and violet) coexisted, indicating different phases. So we increased the temperature for the samples from $Ca_{0.7}Co_{1.3}Ge_2O_6$ to $Ca_{0.3}Co_{1.7}Ge_2O_6$ up to 1250 °C trying to get rid of the phases other than pyroxene. This was unsuccessful, as spinel is still present at 1250 °C. The samples heated at 1250 °C were differently coloured and darker than the samples obtained in the first two runs.

3.2.2 X-Ray Powder Diffraction (XRDP) and Rietveld refinement

For qualitative and quantitative phase analysis, step-scan powder X-ray diffraction data were collected at room temperature in coupled Theta-Theta mode on a Bruker D8 Advance with Da Vinci-Design diffractometer, having a goniometer radius of 280 mm, equipped with a fast solid state *Lynxeye* detector and an automatic sample changer. Data acquisition was performed using Cu $K\alpha_{1,2}$ radiation between 5° and 80° 2Theta, with a step size of 0.02°, integration time of 1 sec, the divergence slit and the receiving slits opened at 0.3° and 2.5°, respectively; a primary and secondary side 2.5° Soller slit was used to minimize axial divergence, and the detector window opening angle was chosen as 2.95°. Data handling and qualitative phase analysis was performed with DIFFRAC.EVA^{TM} V2.1 software (Bruker, 2012).

The phases identified in the three syntheses at different temperatures are:

- $CaCoGe_2O_6$ pyroxene *C*2/*c*;
- $Co_2Ge_2O_6$ pyroxene, both monoclinic (*C*2/*c)* and orthorhombic (*Pbca*) phase;
- Co_2GeO_4 spinel (*Fd*3*m*).

The pyroxene phases are deep pink whereas the spinel is violet-dark pink, even if the cobalt has the same oxidation state (2+) in the same coordination (6). The different colour may be caused by a small distortion within the M1 octahedra in pyroxene.

The determination of the unit cell parameters and the quantitative analysis were performed by the Rietveld method with the GSAS-EXPGUI software package by multiphase refinement (Larson and Von Dreele, 2000). Independent variables for the Rietveld refinement are: zero point, twelve coefficients of the shifted Chebyschev function to fit the background, unit cell dimensions, separate scale factors for the different phases. A pseudo-Voigt profile function is used, refining two Gaussian coefficients (Gv and Gw) and one Lorentzian (Lv). In some cases, the March-Dollase preferential orientation was corrected.

Input data for crystal structures were taken from Redhammer et al. (2008) for $CaCoGe_2O_6$, from Redhammer et al. (2010) for $Co_2Ge_2O_6$ (monoclinic and orthorhombic forms) and from *Inorganic Crystal Structure database (ICSD*) entries 21115 (Furuhashi et al., 1973) for Co_2GeO_4. A good fit of the observed *vs* calculated patterns is always obtained, with χ^2 values varying between 6 and 1.5. To fully take care of residuals, we tried to test in Rietveld refinements GeO_2 in all the symmetries, $CaCoGeO_4$, akermanite, phases normally present in Si analogous system (Mantovani, 2013), but obtaining worse fitting.

In Figure 3.6 an example of Rietveld refinement (GSAS-EXPGUI software) of the samples Co0 1200 ($CaCoGe_2O_6$) is shown; the refinement confirms that the most abundant phase is $CaCoGe_2O_6$.

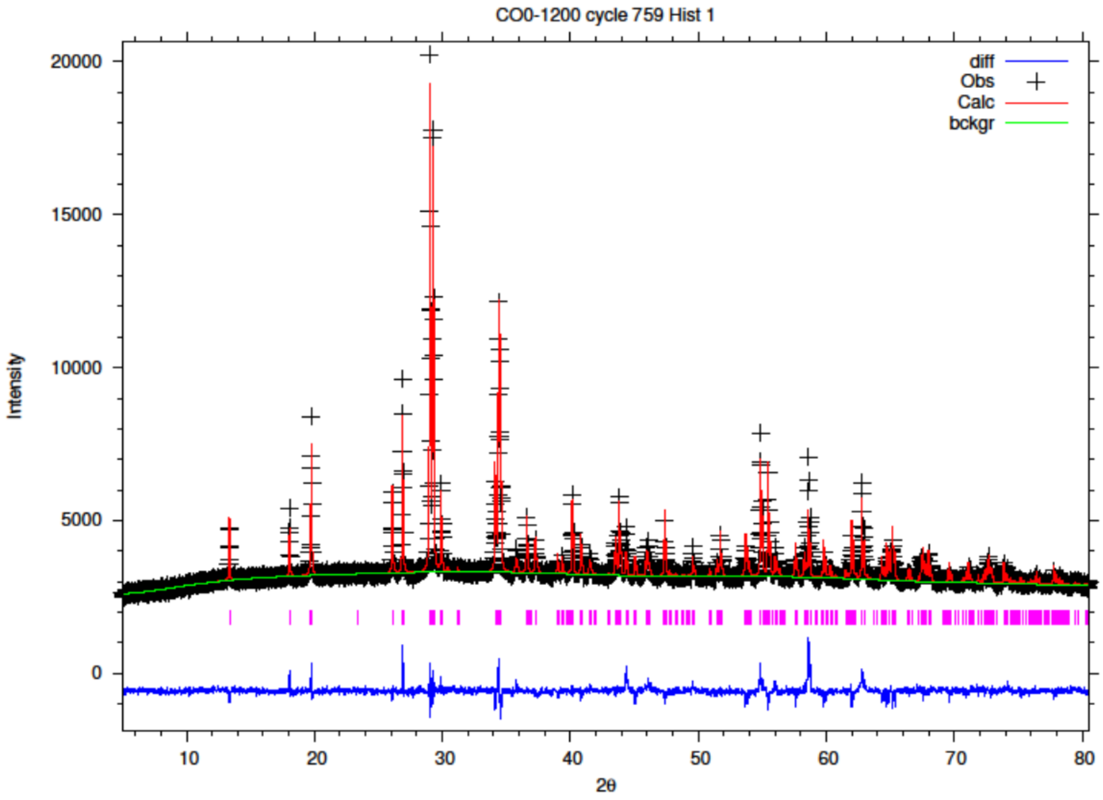

Figure 3.6: Rietveld refinement of the sample Co0 1200 °C (GSAS-EXPGUI software). The experimental data (obs) are indicated by black crosses, the calculated pattern by continuous red line, and the lower blue curve is the weighted difference between the calculated and observed patterns. Fitted background is reported in green. Vertical tick marks report the position of allowed reflections for the $CaCoGe_2O_6$ (in pink) phase present in the sample.

In the Figures below (from Figure 3.7 to 3.12) the diffraction patterns for all the series of samples are visible. The evolution of the phases is more evident in the enlarged 2 theta region in the range 10-45°.

$CaCoGe_2O_6$ has strong diffraction peaks at $2\theta \sim 13.4°$, 18.1°, 19.8°, 26.1° and 26.7°. Orthorhombic $Co_2Ge_2O_6$ is characterized by peaks at 20.8° and 22.3°, while the monoclinic phase has strong peaks at $2\theta \sim 26.5°$, 31.8° and a doublet at $2\theta \sim 35.3$ °.

At 1050 °C the phases formed are the monoclinic pyroxenes (Ca, Co) and a little amount of spinel.

The presence of monoclinic $Co_2Ge_2O_6$ is evident by two peaks at 2θ ~ 26.1 ° and at 31.8°, 35.1 and 35.4° (Figure 3.8).

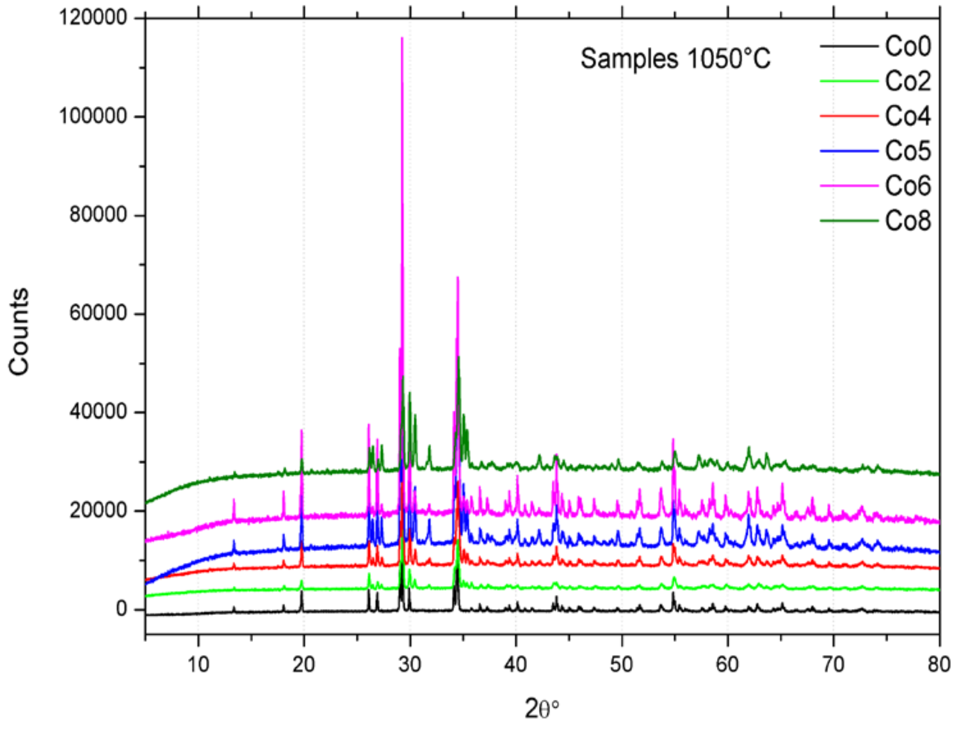

Figure 3.7: X-ray diffraction patterns (5-80°) for samples heated at 1050 °C.

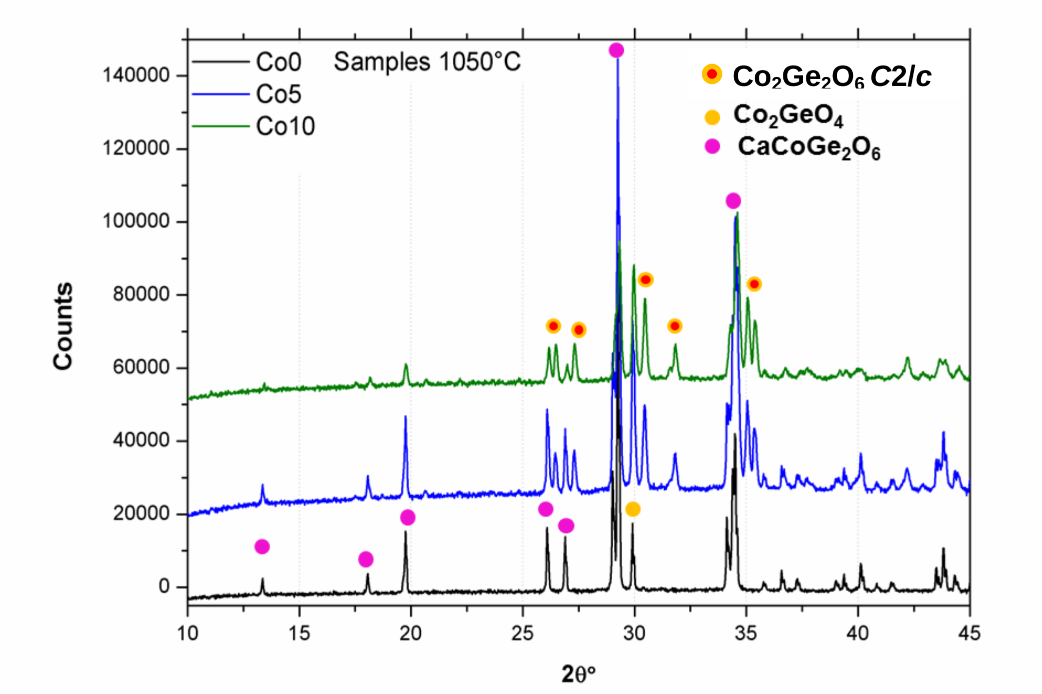

Figure 3.8: X-ray diffraction patterns (10-45°) for samples heated at 1050 °C. The phase identification by the major peaks is reported.

The annealing at 1200 °C allowed the formation of the orthorhombic end-member of Co pyroxene, unlike the Si-system in which the $Co_2Si_2O_6$ *Pbca* phase needs higher pressure (Mantovani, 2013). Increasing the amount of cobalt in M2 site, the peaks at lower 2θ (~ 13.4°, 18.1°, 19.8°), that identify $CaCoGe_2O_6$, show lower intensity, while peaks at ≈ 27° and ≈ 35°, attributed to $Co_2Ge_2O_6$ *Pbca,* arise (Figure 3.9-10).

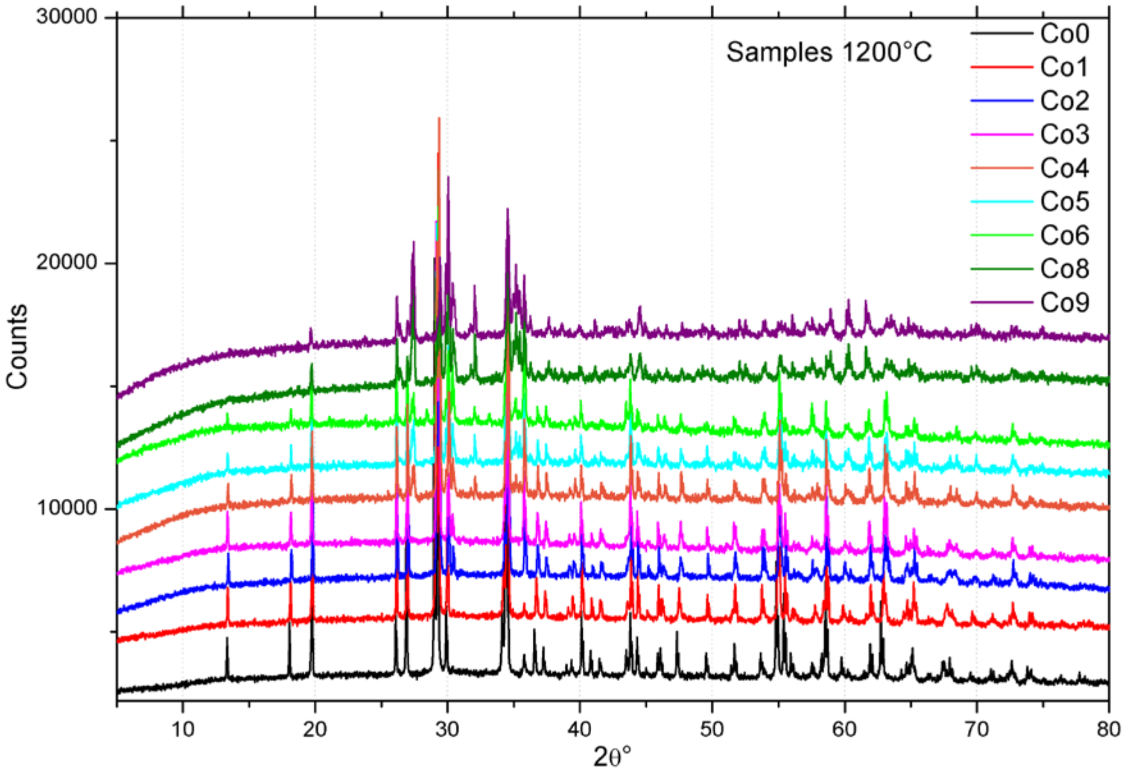

Figure 3.9: X-ray diffraction patterns (5-80°) for samples heated at 1200 °C.

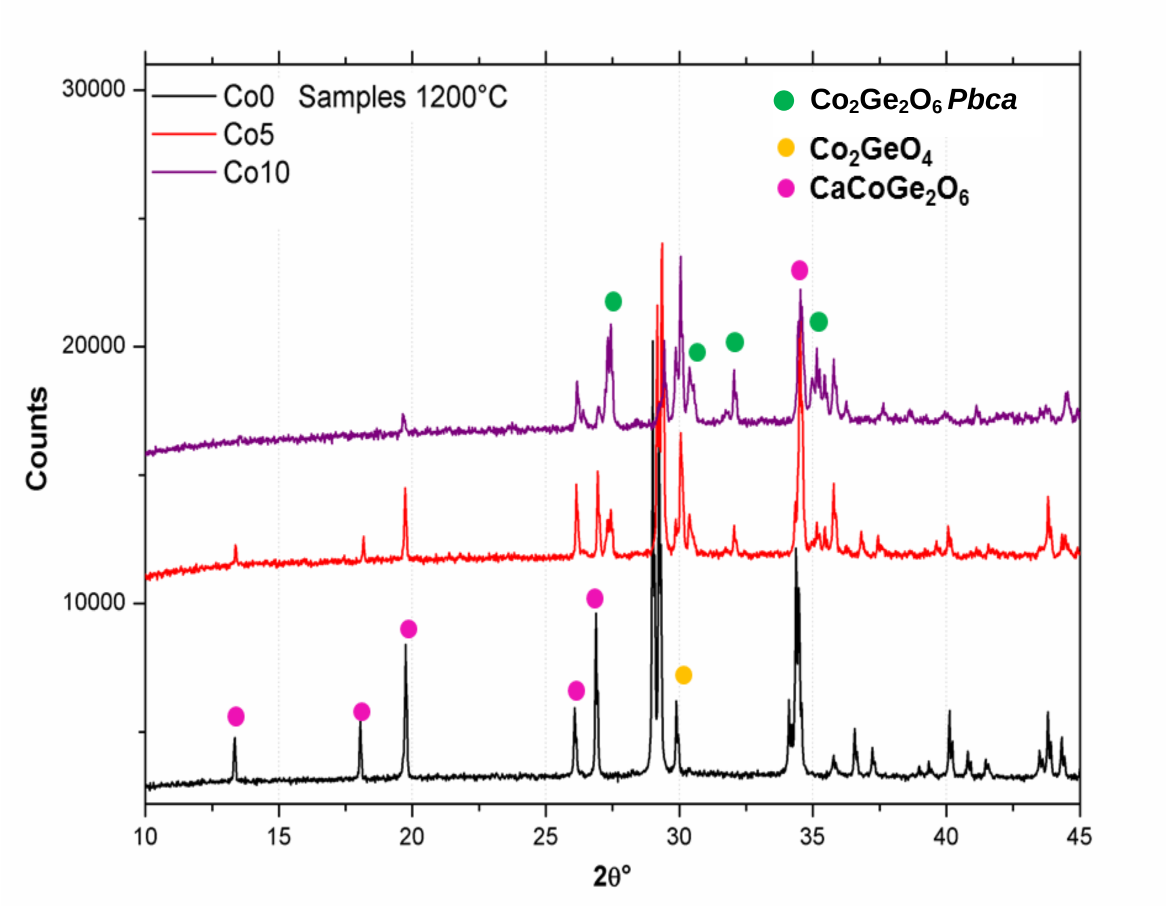

Figure 3.10: X-ray diffraction patterns (10-45°) for samples heated at 1200 °C. The phase identification for the major peaks is reported.

The diffraction patterns at the last temperature 1250 °C (Figures 3.11-3.12) are very similar to those at 1050 °C. The phases formed are $CaCoGe_2O_6$ pyroxene, the spinel and a little amount of $Co_2Ge_2O_6$ *Pbca.* This latter point is quite surprising, as, by stoichiometric requirement, the Co rich pyroxene phase should be present in higher amount.

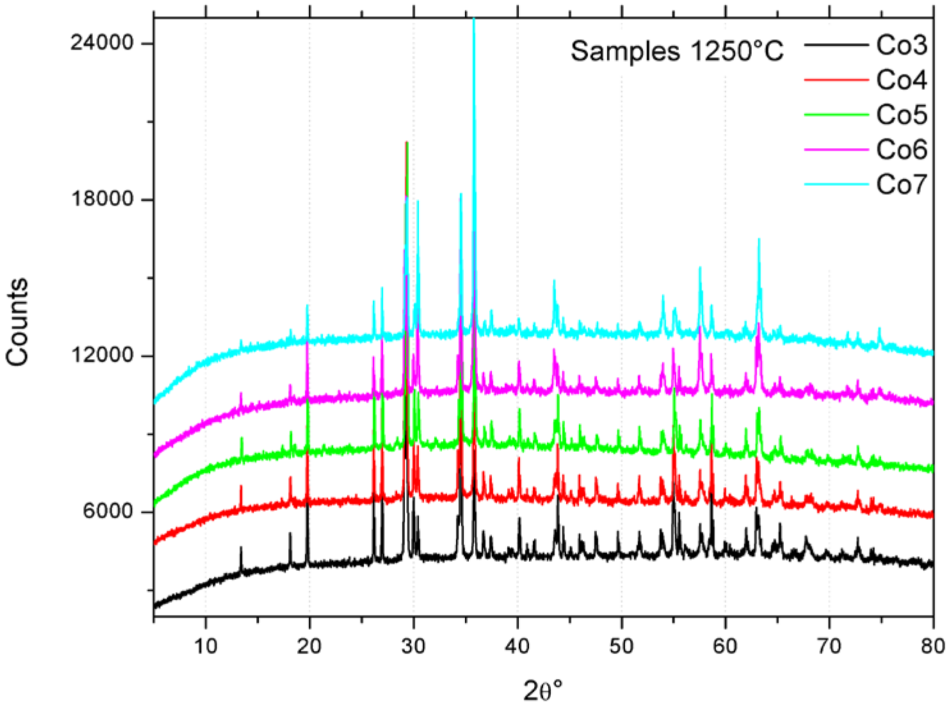

Figure 3.11: X-ray diffraction patterns (5-80°) for samples heated at 1250 °C.

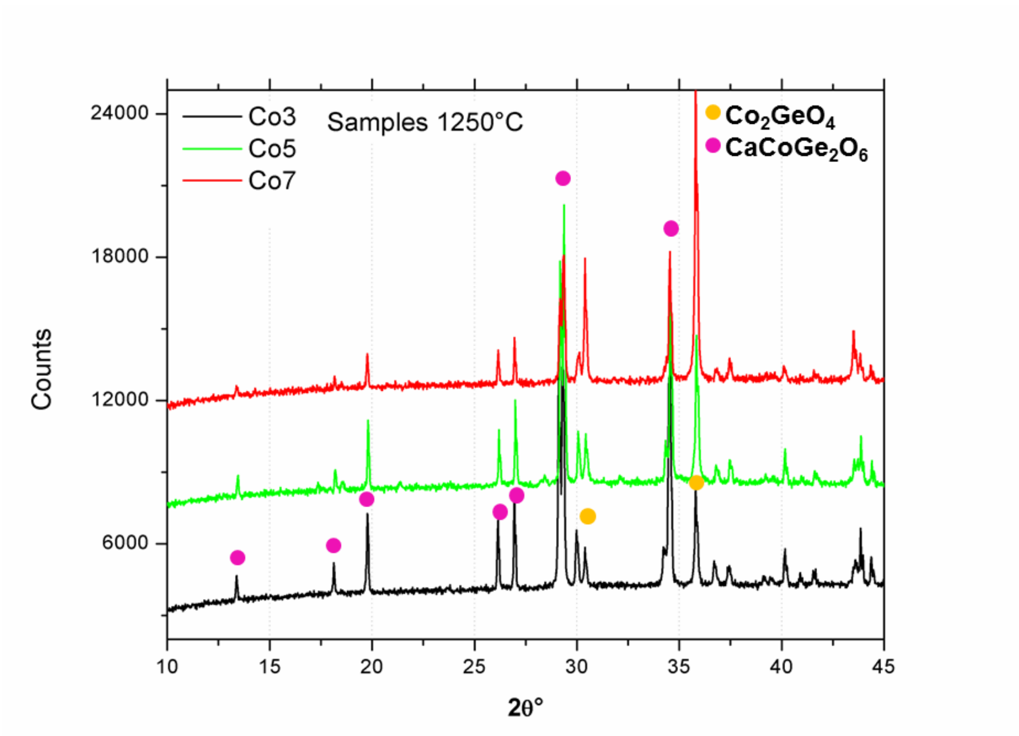

Figure 3.12: X-ray diffraction patterns (10-45°) for samples heated at 1250 °C. The phase identification for the major peaks is reported.

Tables below show that, in all the runs, the Ca pyroxene is found at higher amount in Ca richer samples. Co$_2$Ge$_2$O$_6$ *C2/c* is formed at 1050 °C while at 1200 °C its symmetry changes to an orthorhombic form. On the other hand, spinel has been found in a low amount between Co2 and Co10 at 1050 and 1200 °C, and at 1250 °C its quantity increases, especially in Co-richer samples.

The cell parameters and weight fraction for all the samples are listed in the Tables below.

Table 3.3: cell parameters and wt.% fraction for the sample synthesized at 1050 °C. The error is reported in brackets. If the wt.% fraction is less than 5% the Rietveld refinement is not accurate in determining the phase content.

Sample	**Co0**	**Co2**	**Co4**	**Co5**	**Co6**	**Co8**	**Co10 ***
Co fraction (a.p.f.u.)	1	1.2	1.4	1.5	1.6	1.8	2
CaCoGe$_2$O$_6$ (wt.%)	**98.4**	**80**	**59.9**	**51.4**	**46.8**	**20.5**	
a (Å)	10.1531(3)	10.1391(3)	10.1368(6)	10.1306(6)	10.1295(7)	10.1253(1)	
b (Å)	8.9772(3)	8.9824(3)	8.9854(5)	8.983(5)	9.0059(4)	8.978 (1)	
c (Å)	5.429(1)	5.4217(4)	5.4199(2)	5.4171(2)	5.4158(3)	5.4157(6)	
β (°)	104.888(2)	104.987(2)	105.009(3)	105.015(3)	105.021(4)	105.065(8)	
V (Å ^{3})	478.23(3)	476.98(2)	476.83(5)	476.14(5)	475.93(6)	475.39(7)	
Co$_2$Ge$_2$O$_6$ *C2/c* (wt.%)		**18.2**	**39.7**	**48.6**	**49.7**	**79**	
a (Å)	9.685(7)	9.6809(9)	9.6837(5)	9.6816(5)	9.6800(5)	9.6779(3)	9.67315()
b (Å)	9.0266(6)	9.0064(8)	9.0093(5)	9.007(4)	9.0059(4)	9.0038(3)	9.00294(6)
c (Å)	5.1823(3)	5.1762(5)	5.1772(3)	5.1764(2)	5.1759(2)	5.1754(2)	5.17437(4)
β (°)	101.7(6)	101.445(9)	101.465(4)	101.465(3)	101.451(3)	101.424(2)	101.313(6)
V (Å ^{3})	443.6(4)	442.35(5)	442.67(5)	442.39(2)	442.23(5)	442.04(3)	441.895(5)
Co$_2$GeO$_4$ (wt.%)	**0.7**	**1.7**	**nd**	**nd**	**3.5**	**0.6**	
a (Å)	8.316(1)	8.3138(6)			8.312(5)	8.312(1)	
V (Å ^{3})	575.105(262)	574.6(1)			574.2(1)	574.4(3)	

* Sample and data taken from Redhammer et al. (2010).

Table 3.4: cell parameters and wt.% fraction for the sample synthesized at 1200 °C. The error is reported in brackets. If the wt.% fraction is less than 5% the Rietveld refinement is not accurate in determining the phase content.

Sample	**Co0**	**Co1**	**Co2**	**Co3**	**Co4**	**Co5**	**Co6**	**Co8**	**Co9**	**Co10 ***

V (Å ^{3})	*c* (Å)	*b* (Å)	*a* (Å)	**$Co_2Ge_2O_6$ *P bca* (wt.%)**	V (Å ^{3})	β (°)	*c* (Å)	*b* (Å)	*a* (Å)	**$CaCoGe_2O_6$ (wt.%)**	**Co fraction (a.p.f.u.)**
					478.06(2)	104.858(1)	5.4291(1)	8.9746(1)	10.1511(2)	**98.6**	1
916(1)	5.376(2)	8.99(2)	18.958(6)	**1.48**	475.507	104.943(1)	5.4172(2)	8.9714(2)	10.1265(2)	**97.9**	1.1
916(2)	5.41(1)	8.9797(7)	18.87(4)	**2.4**	474.78(1)	104.911(2)	5.4095(2)	8.9813(2)	10.1129(2)	**92.9**	1.2
				nd	473.07(3)	104.843(2)	5.3976(2)	8.9833 (3)	10.0930(3)	**95.1**	1.3
916.5(1)	5.3831(6)	9.0185(1)	18.878(2)	**19.9**	472.83(3)	104.816(2)	5.3951(2)	8.9863(3)	10.0881(3)	**74.8**	1.4
916.10(9)	5.3826(4)	9.0187(6)	18.871(1)	**31.8**	472.58(3)	104.808(2)	5.3936(2)	8.9860(2)	10.0854(3)	**62.8**	1.5
917.2(2)	5.385(1)	9.019(2)	18.885(3)	**27.1**	473.10(4)	104.824(2)	5.3961(3)	8.9885(4)	10.0899(4)	**61.6**	1.6
916.9(2)	5.3856(4)	9.01988(7)	18.876(1)	**79.1**	472.93(9)	104.85(9)	5.3958(6)	8.989(1)	10.088(1)4	**13.3**	1.8
915.2(2)	5.3819(6)	9.014(1)	18.867(2)	**89.1**	476.9(4)	105.51(4)	5.479(4)	8.963(6)	10.080(6)	**6.5**	1.9
910.5(1)	5.3762(4)	9.0220(7)	18.8336(2)								2

Co_2GeO_4 (wt.%)	*a* (Å)	V (Å ^{3})
1.4	8.313(2)	574.5(4)
0.6	8.311(1)	574.2(3)
1.7	8.3131(3)	574.51(5)
4.9	8.3101(3)	573.86(7)
5.3	8.3113(4)	574.13(8)
5.4	8.3104(3)	573.94(7)
11.31	8.3131(3)	574.2(1)
7.6	8.3127(7)	574.4(1)
4.4	8.307(6)	573.1(1)

*Sample and data taken from Redhammer et al., (2010).

Table 3.5: cell parameters and wt.% fraction for the sample synthesized at 1250 °C. The error is reported in brackets. If the wt.% fraction is less than 5% the Rietveld refinement is not accurate in determining the phase content.

Sample	**Co3**	**Co4**	**Co5**	**Co6**	**Co7**
Co fraction (a.p.f.u.)	1.3	1.4	1.5	1.6	1.7
$CaCoGe_2O_6$ (wt.%)	**89.5**	**81.7**	**82.3**	**69.3**	**56.3**
a (Å)	10.1300(4)	10.1150(3)	10.1157(4)	10.1258(6)	10.1008(7)
b (Å)	8.9761(4)	8.9766(2)	8.9841(4)	8.9769(6)	8.9825(5)
c (Å)	5.4180(3)	5.4113(2)	5.4111(3)	5.4160(5)	5.3989(4)
β (°)	104.946(2)	104.925(2)	104.928	104.97(4)	104.861(5)
V (Å ^{3})	475.98(5)	474.77(4)	475.17(5)	475.60(7)	473.45(6)
$Co_2Ge_2O_6$ *Pbca* (wt.%)	**1.5**	**3.6**	**1.0**	**0.4**	**14. 3**
a (Å)	18.89(3)	18.916(3)	18.92(2)	18.80(1)	18.32(2)
b (Å)	8.99(1)	8.985(2)	8.98(1)	8.985(8)	8.16(1)
c (Å)	5.381(9)	5.391(1)	5.354(6)	5.3834(5)	5.042(6)
V (Å ^{3})	913(1)	916.2(2)	910(1)	909(1)	910.5(1)
Co_2GeO_4 (wt.%)	**9.1**	**13.0**	**16.6**	**26.2**	**29.4**
a (Å)	8.3141(4)	8.311(3)	8.3168(4)	8.315(3)	8.3117(3)
V (Å ^{3})	574.72(9)	574.09(7)	574.71(6)	574.79(7)	574.21(6)

3.2.3 Phase diagram of the $CaCoGe_2O_6$-$CoCoGe_2O_6$ system vs Si pyroxenes

In spite of the large changes in bulk composition, cell parameters of the synthesized phases change very little at 1050 °C. This indicates that the composition of the single phases doesn't change, whereas the abundance is varying. In more detail, in the Ca,Co-pyroxene phase the *a, b, c* parameters do not change significantly, but small changes in the β angle (104.8° - 105.8°) and in volume (478.2 $Å^3$ - 475.4 $Å^3$) are observed, which can be hardly related to changes in the bulk composition. The topology of this pyroxene is HT-*C*2/*c* (high temperature), in which the tetrahedral chains are relatively straight (Arlt and Angel 2000, Mantovani, 2013).

From the plot in Figure 3.13 it appears that β and volume changes in the Ca,Co-pyroxene correspond to a variation of Co content of about 0.1 - 0.2 a.p.f.u in M2, by similarity with the corresponding solution of Co for Ca in the Si analogue $CaCoSi_2O_6$. These small quantities of Co in M2 indicate that only limited solid solution is possible at room pressure.

The crystallographic parameters of $Co_2Ge_2O_6$ monoclinic do not change significantly (Figure 3.14).

The systematic phase relations in $Co_2Ge_2O_6$ were first studied by Tauber and Kohn (1965), who found, in equilibrium synthesis experiments, that $Co_2Ge_2O_6$ is dimorphous in nature and possesses a monoclinic (clinopyroxene) and an orthorhombic (orthopyroxene) form. They stated that up to 1300 °C the orthorhombic $Co_2Ge_2O_6$ is stable as a single phase, while only monoclinic $Co_2Ge_2O_6$ is found at higher temperatures. The structure of monoclinic $Co_2Ge_2O_6$ was determined at room temperature by Peacor (1968). The compound shows the typical pyroxene *C*2/*c* symmetry and is characterized by strongly kinked GeO_4 tetrahedral chains. The structure can be interpreted on the basis of a distorted cubic close-packing of oxygens (Tribaudino et al., 2005). Such a distinct kinking of the chains is generally evident only in clinopyroxenes that underwent a high-pressure phase transition from $P2_1/c$ to HP-*C*2/*c* (Nestola et al., 2009). The phase transition between HT and HP polymorph of *C*2/*c* symmetry (Arlt and Angel, 2000) is first order. The high difference in chain kinking (50°) makes the two *C*2/*c* HP and HT structures very different, and little compatible. One may define monoclinic $Co_2Ge_2O_6$ as a germanate analogue to the HP-*C*2/*c* silicate clinopyroxene (Redhammer et al., 2010). The pyroxene with cobalt in M2 exhibits smaller volume and β angle than those with Ca in M2, due to the smaller ion size (Arlt and Angel, 2000) and by the more closely packed nature of the HP-*C*2/*c* phase, with strongly kinked chains. The solid solution between the two end members, showing HT and HP structures, is then limited.

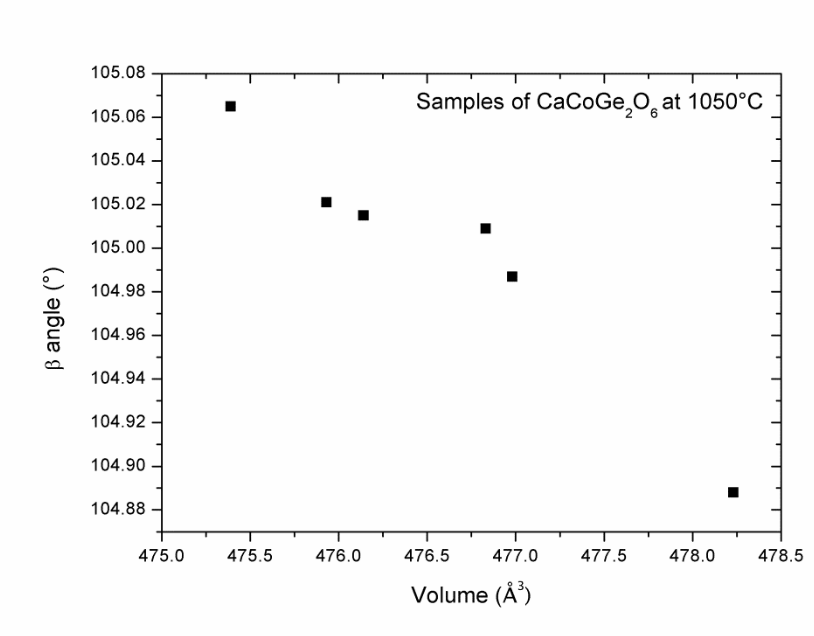

Figure 3.13: β angle (°) vs cell volume (Å^3) for the samples of $CaCoGe_2O_6$ synthesized at 1050 °C and room pressure.

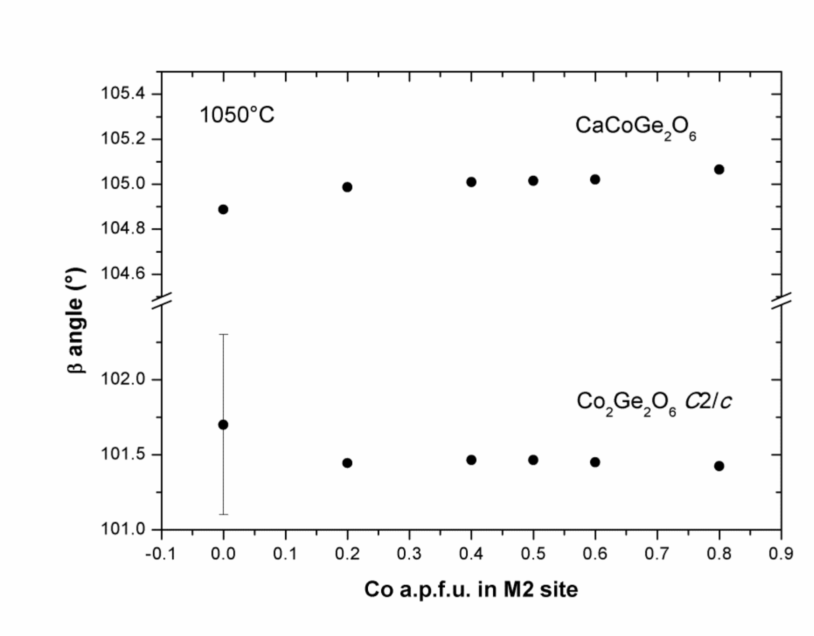

Figure 3.14: β angle (°) vs volume value (Å^3) for the samples of $CaCoGe_2O_6$ and $CaCoGe_2O_6$ synthesized at 1050 °C and room pressure. The errors are reported.

At 1200 °C, the the *a, b, c* parameters of Ca,Co-pyroxene phases change very little but a significant change in the β angle and in volume indicates some solid solution (Figure 3.15).

At 1200 °C the cobalt pyroxene formed is orthorhombic. In the samples in which there is a little amount of orthorhombic phase (from Co0 to Co3), a greater solubility is observed.

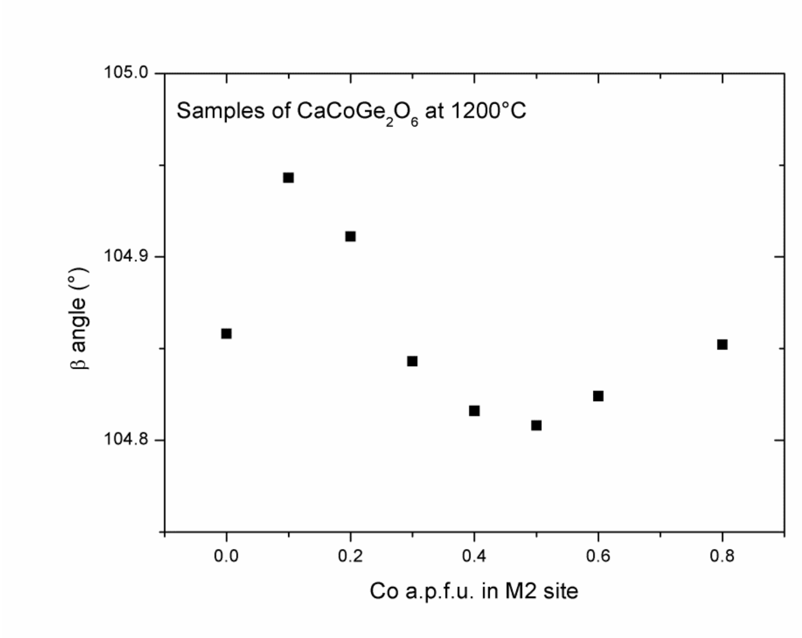

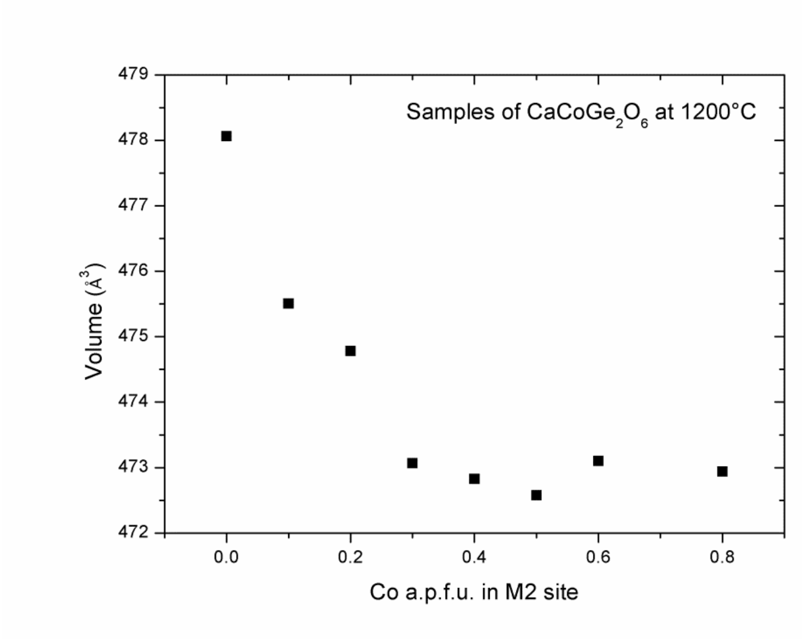

Figure 3.15: β angle (°) on the top and volume (Å^3) above vs Co a.p.f.u. for the samples of $CaCoGe_2O_6$ synthesized at 1200 °C and room pressure. The data for Co9 were not taken into account because they are affected by a large error.

At 1250 °C, the Co_2GeO_4 spinel and Ca pyroxene are stable, while the orthorhombic phase is not present.

Previous synthesis experiments on $Co_2Ge_2O_6$ confirmed that the orthopyroxene has a very limited stability range; below 1100 °C and above 1300 °C the monoclinic form is stable (Tauber and Kohn, 1965). In situ high temperature X-ray diffraction experiments suggested that the monoclinic to orthorhombic phase transition starts around 1050 °C showing that there is no sudden transition, but a wide temperature range, where both phases coexist. The study of the phase transition is complicated by the decomposition of $Co_2Ge_2O_6$ due to CoO loss above 1080 °C. On the other hand, the synthesis of $Co_2Ge_2O_6$ is aggravated for temperatures T>1220 °C, where there is substantial loss of GeO_2 and, consequently, the formation of a Co_2GeO_4 spinel phase initiates (Redhammer et al., 2010).

Figures 3.16-17-18 show the trend of the weight percentages of each phase, as a function of Co content in the M2 site at the different temperatures. At 1050 °C the two monoclinic pyroxenes change their amount with composition, indicating that varying the bulk composition simply changes the phase fractions but not their composition. At 1200 °C Ca,Co-pyroxene is always present, along the entire series, but its abundance decreases drastically from Co5 onwards, when the weight of Co-pyroxene increases. This may be related to solid solution behaviour, but there are not significant changes of cell parameters along the join confirming this trend. Spinel is present in small amount at 1050 and 1200 °C, while at 1250 °C it reaches 30% weight, as cobalt forms this phase and not pyroxene.

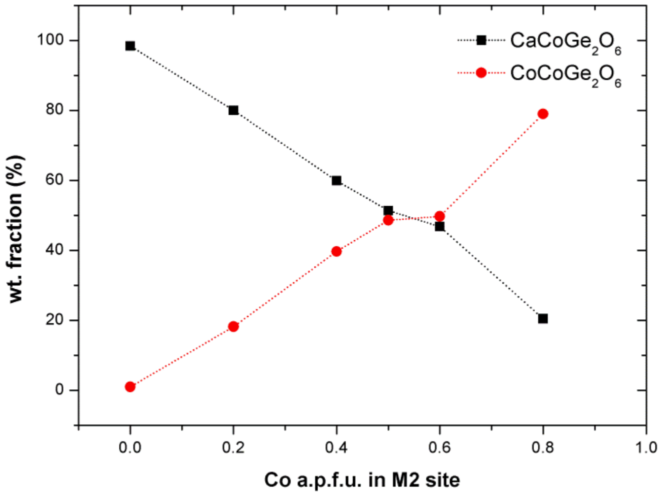

Figure 3.16: wt. fraction (%) of the phases vs Co content (a.p.f.u.) in M2 site at 1050 °C.

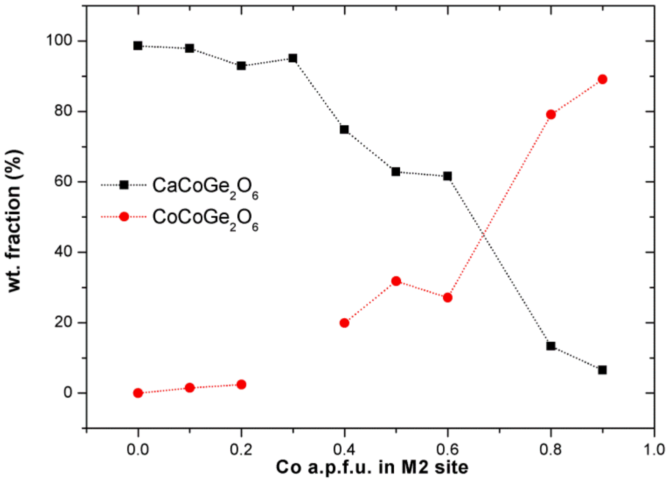

Figure 3.17: wt. fraction (%) of the phases vs Co content (a.p.f.u.) in M2 site at 1200 °C.

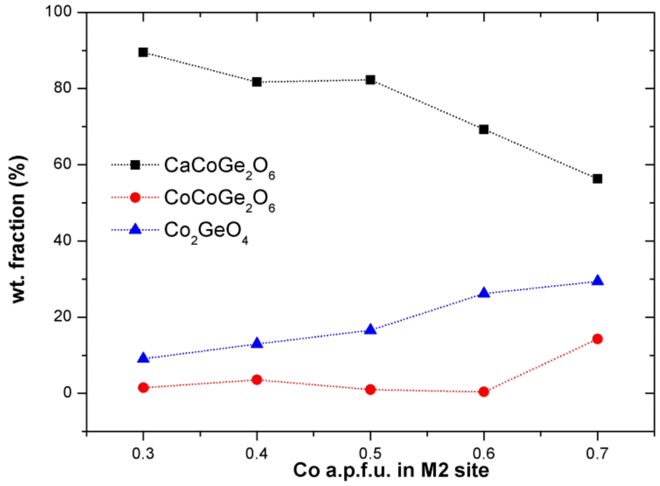

Figure 3.18: wt. fraction (%) of the phases vs Co content (a.p.f.u.) in M2 site at 1250 °C.

In comparison with the CaCo-$CoCoSi_2O_6$ system studied by Mantovani (2013), the Ca-Co substitution with germanium in T site produces many differences in the phase diagram and in the crystallographic parameters.

First of all, the end member $CoCoGe_2O_6$ pyroxene is stable at room pressure, whereas in the silicate system this occurs only above 3 GPa (Mantovani et al., 2014); moreover, at room pressure it displays two symmetries: monoclinic *C2/c* and orthorhombic *Pbca*. The analogous silicate forms at 3 GPa and 1200 °C in *Pbca* symmetry while the monoclinic one was synthesized only at 7 GPa and 900 °C.

In this system CaCo-$CoCoGe_2O_6$, the structure of spinel instead of akermanite is found. This structure is formed by a phase transition of an olivine structure; the same olivine to spinel transition occurs for silicates in the transition zone in the Earth's mantle, at 400 Km depth (Pearson et al., 2014). This phase highlights that germanium analogues of silicates are model systems for high-pressure silicate minerals and offers the possibility of obtaining useful information about phase transformations which may occur in silicates at pressures beyond the range of currently available experimental techniques (Ringwood and Seabrook, 1963). When a silicate or germanate is subjected to high pressure, the large oxygen ions tend to contract relatively more than the small Si^{4+} and Ge^{4+} ions; hence the R_{Si} / R_o and $R_{Ge}./R_o$ ratios increase. The transformation into a new high-pressure phase occurs when these ratios attain some critical value. Since the zero-pressure radius of Ge^{4+} (0.48 Å) is already slightly larger than that of Si^{4+} (0.42 Å), germanates require smaller pressures to achieve the critical ratios required for given transitions than the corresponding silicates do: because of the initially higher radius ratios, germanates may crystallize at zero pressure in a structure which is only attained by the silicates at high pressure.

Another difference is that there is no symmetry change in monoclinic pyroxenes, contrary to what occurs in the Si system, where at high pressure, for 0.7 a.p.f.u. of cobalt in M2 site, the symmetry changes from *C*2/*c* to $P2_1/c$ (Mantovani et al., 2014 a,b). The calcium end member, like the Si-system, is a monoclinic *C*2/*c* stable form.

In Figure 3.19 the phase diagrams of the two systems: $CaCoSi_2O6$-$Co_2Si_2O_6$ (Mantovani, 2013) and $CaCoGe_2O_6$ - $Co_2Ge_2O_6$ are sketched.
The phase diagram of the Si pyroxenes is shown at 3 GPa, where only pyroxene phases are present, while for Ge the diagram is displayed at room pressure. In the Ge-diagram, at ~1000 °C we find the coexistence of CaCo clinopyroxene and CoCo clinopyroxene, while in the Si-diagram one has CaCo-clinopyroxene and CoCo-orthorhombic pyroxene. At 1200 °C, in both systems, Ca rich clinopyroxene exists with Ca poor orthorhombic pyroxene. At 1250 °C the Ca rich pyroxene is stable in both systems, but in the germanates also Ge-spinel Co_2GeO_4 is stable.

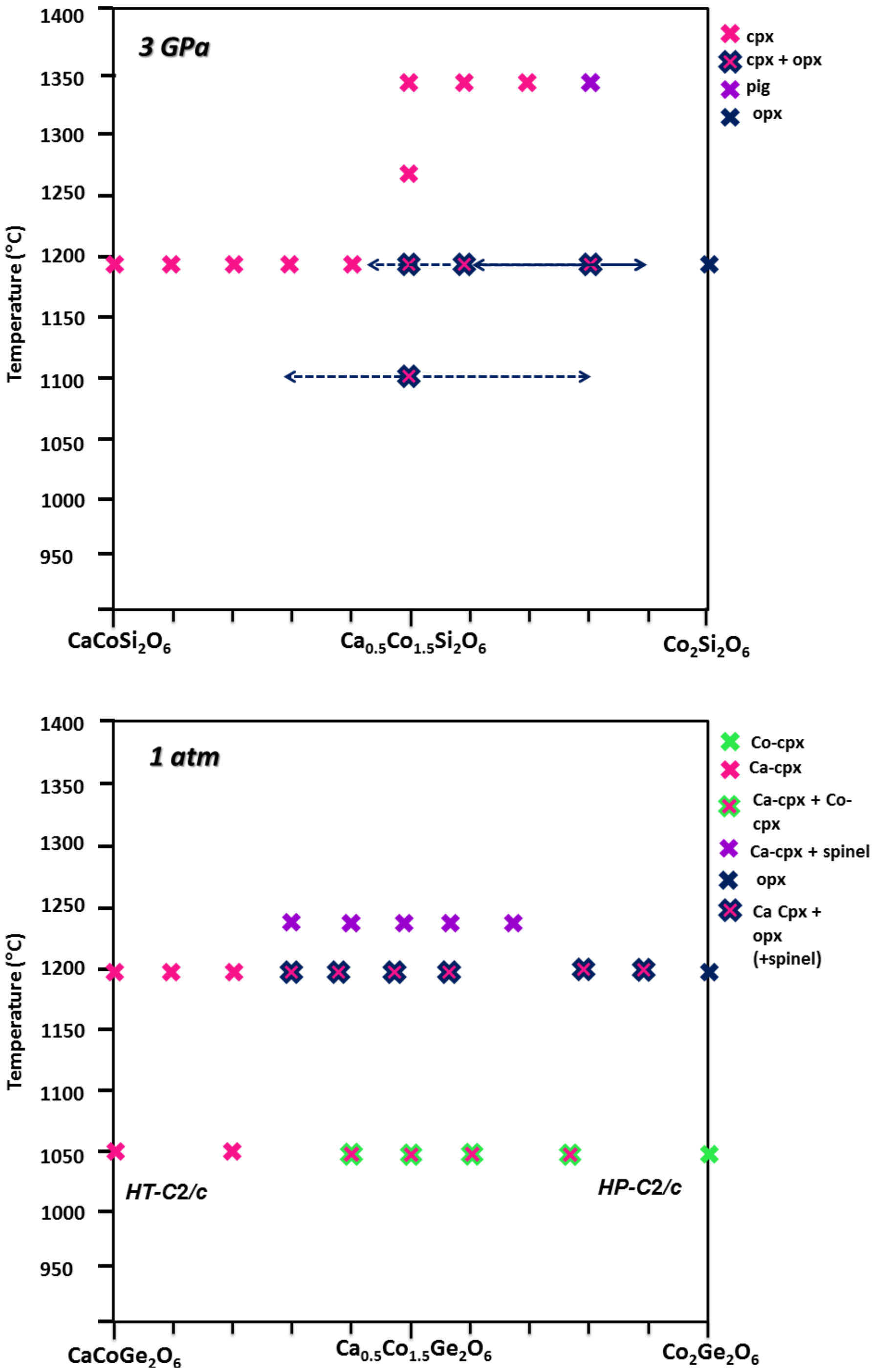

Figure 3.19: a sketch of phase diagram of the subsolidus: on the top the $CaCoSi_2O_6$-$Co_2Si_2O_6$ system at 3 GPa (Mantovani, 2013) and on the bottom $CaCoGe_2O_6$ - $Co_2Ge_2O_6$ at room pressure.

High pressure syntheses are needed in order to extend the solid solution range in germanates. Furthermore, technological tests on the $CaCoGe_2O_6$ and $CoCoGe_2O_6$ end-member will be useful to determine their stability in glazes and glassy coatings.

Part 1:

Vibrational Properties

Chapter IV

RAMAN SPECTROSCOPY

The most reliable method of phase identification in mineralogy is the X-ray diffraction, which provides detailed information about the crystalline structure. However, the process can require hours or days to perform a complete structural analysis. In the last years, Raman spectroscopy of minerals was used in order to obtain structural information and to monitor phase transitions in response to applied *T*, *P* or change in composition. The aim of this chapter is to follow the differences in the vibrational features due the various substitutions both in tetrahedral and in octahedral sites in pyroxene structure.

4.1 Raman spectroscopy of $CaCoGe_2O_6$ and $CaMgGe_2O_6$ at ambient conditions compared with the corresponding silicates

Extended Raman studies were performed on clinopyroxenes, with the aim of using them as a probe for further geological investigation, but also to clarify the relations between vibrational modes and structure (Mantovani et al., 2014; Tribaudino et al., 2012; Prencipe et al., 2012; Wang et al., 2001; Huang et al. 2000; Yang et al., 1999). Raman studies were almost completely devoted to clinopyroxenes with Si in the tetrahedral site. However, synthetic pyroxenes with Ge in the T site have several points of interest. Even if germanates have been studied for many years, and Ge-pyroxenes in particular to describe the phase transitions mechanisms at the atomic scale (Pearson et al., 2014), only a very few papers about Raman spectroscopy on germanates are available in the literature: here we show the Raman spectra of $CaCoGe_2O_6$ and $CaMgGe_2O_6$.

The results of this work were published in: Journal of Raman Spectroscopy, *46: 586-590,* E. Lambruschi, I. Aliatis, L. Mantovani, M. Tribaudino, D. Bersani, G. J. Redhammer, P. P.

Lottici (2015). Raman spectroscopy of $CaM^{2+}Ge_2O_6$ (M^{2+} = Mg, Mn, Fe, Co, Ni, Zn) clinopyroxenes (http://onlinelibrary.wiley.com/doi/10.1002/jrs.4681/full).

4.1.1 Crystal structure of the analysed samples

The samples under investigation are monoclinic pyroxenes with symmetry *C2/c.* $CaCoGe_2O_6$, $CaMgGe_2O_6$ and $CaCoSi_2O_6$ are synthetic, while $CaMgSi_2O_6$ is natural from a rodingitic rock sampled at Bellecombe, Aosta Valley, Italy.

The crystal structure and synthesis condition for $CaCoGe_2O_6$ are published in Redhammer et al. (2008), while for $CaCoSi_2O_6$ in Mantovani (2013). $CaMgGe_2O_6$ was kindly provided by G. Redhammer, who performed also the crystal structure of the sample. Natural diopside, $CaMgSi_2O_6$ was previously studied by Prencipe et al., (2000).

4.1.2 Experimental

Raman measurements were carried out in backscattering geometry using a Horiba Jobin-Yvon LabRam instrument equipped with a holographic grating (1800 lines/mm) and a CCD detector (1024 × 256 pixels). The Rayleigh radiation was blocked by reflective volume Bragg grating notch filters BragGrateTM (OptiGrate), which enable Raman shift measurements down to ~10 cm^{-1} from the laser line. The 632.8 nm line of a He-Ne laser was used for excitation. Laser power on the sample was kept less than 1 mW. The wavenumber calibration was performed by the strong Raman peak of a silicon sample at 520.6 cm^{-1}. A 100x objective with numerical aperture 0.9 was used with a spatial resolution of about 1-2 μm. The spectral resolution was about 1.5 cm^{-1} with a 150 μm confocal hole. Collection time of the spectra ranged from 3 to 12 minutes (typical exposures were 60-240 sec, repeated 3 times), depending upon the crystal size, the Raman scattering efficiency, and the intensity (if any) of the background fluorescence.

Raman analyses were made on loose grains without any sample preparation. At least eight spectra were collected for each sample at different spots and here we report the average spectrum: due to the small grain size, no attempt was made to take Raman spectra from oriented single crystals and then to evidence orientation effects. The peak positions were obtained from baseline-corrected spectra by a curve-fitting least-squares routine using Labspec® software package. A pseudo-Voigt profile was used in the peak profile analysis.

4.1.3 Results and discussion

Factor-group analysis at Γ point (**k**=0) shows that *C*2/*c* pyroxenes, with 20 atoms per primitive unit cell (Z=2), are expected to have 30 ($14A_g+16B_g$) Raman active modes (Rustein and White, 1971). To our best knowledge, no assignment of the Raman bands of germanate pyroxenes has been yet done, if we exclude the recent work of Oreshonkov et al. (2015) on $MnGeO_3$, although many studies exist about silicate pyroxenes *(*Mantovani et al., 2014; Tribaudino et al., 2012; Prencipe et al., 2012; Wang et al., 2001; Huang et al. 2000; Yang et al., 1999). Recently, *ab initio* quantum mechanical calculations of Raman and IR wavenumbers (Prencipe et al., 2012) and intensities (Prencipe et al., 2014) were published.

The Raman spectra of two silicate pyroxenes, $CaMgSi_2O_6$ and $CaCoSi_2O_6$, are compared with those of the corresponding germanates $CaMgGe_2O_6$ and $CaCoGe_2O_6$ in Figure 4.1 and 4.2.

According to Wang et al., (2001), the spectra of silicate pyroxenes can be divided in five spectral regions:

1) R1 (1100-800 cm^{-1}), showing a strong asymmetric peak near 1000 cm^{-1}, and some broad and weak humps on both low and high wavenumber side, ascribed to Si-O_{nbr} stretching modes, where O_{nbr} is a non-bridging oxygen;

2) R2 (800-600 cm^{-1}), with a strong doublet or an asymmetric single peak near 670 cm$^{–1}$ due to the stretching/bending modes of Si-O_{br}-Si bonds, O_{br} being the bridging oxygen between tetrahedra in the pyroxene tetrahedral chain (O3);

3) R3 (450-300 cm^{-1}), with a group of strong overlapping peaks (motions of the cations in M2 and M1 sites correlated with tetrahedral chain motion and tilting tetrahedra);

4) R4 (600-450 cm^{-1}) characterized by a group of overlapping peaks of moderate intensities, ascribed to O-Si-O vibrations;

5) R5 (below 300 cm^{-1}) with a few peaks of moderate intensity.

R3 and R5 regions have been attributed to “lattice” modes (Wang et al., 2001).

The Raman spectra of germanate pyroxenes display patterns similar to silicate pyroxenes, but shifted to lower wavenumbers (Guyot et al., 1986), due to the substitution of Si^{4+} with heavier Ge^{4+}. The Si–O bond length for 4-coordinated Si is typically between 1.60 and 1.65 Å, whereas the Ge–O distance ranges from 1.70 to 1.80 Å (Wang et al., 2003). Lower vibrational wavenumbers in germanates with respect to silicates are therefore expected not only because of the increased atomic mass of the tetrahedral cation but also for the weaker Ge-O bond strength. Guyot et al. (1986) described the magnitude of the red-shift in the Raman spectra of Mg_2GeO_4 compared to Mg_2SiO_4 (olivine structure) by a very simple harmonic oscillator model. They assumed (Coulombic) Ge- or Si-O force constants proportional to the inverse of the third power of the interatomic distances d. The ratio of the wavenumbers of corresponding bands in magnesium silicate and germanate therefore gives:

$$\frac{\nu_{Si}}{\nu_{Ge}} = \sqrt{\frac{\mu_{Ge}}{\mu_{Si}}}\left(\frac{d_{Ge-O}}{d_{Si-O}}\right)^{3/2} = 0.813, \text{ with: } \mu^{-1}_{Ge,\,Si} = m^{-1}_{Ge,\,Si} + m^{-1}_{O}.$$

In the olivine structure, isolated $[SiO_4]^{4-}$ tetrahedra are connected only by interstitial cations. Pyroxenes are inosilicates with interlocking chains of silicate tetrahedra; their structure is more complex than olivine but the intra-tetrahedral distances do not change. We may therefore expect that the scaling ratio between the vibrational wavenumbers of the main intra-tetrahedral modes in silicates and germanates is similar also for pyroxenes.

We consequently assign the main peak at ~850 cm^{-1} in germanate pyroxenes to the symmetric stretching mode of Ge-O_{nbr} in the $[GeO_4]^{4-}$ subunits and the strong peak at ~550 cm^{-1} to chain bending of Ge-O_{br}-Ge bonds. A comparison between $CaMgGe_2O_6$ and $CaCoGe_2O_6$ with $CaMgSi_2O_6$ and $CaCoSi_2O_6$ gives for the corresponding main peak wavenumbers a ratio of 0.846 (Mg) and 0.833 (Co), whereas for chain bending mode the ratio is 0.831 (Mg) and 0.825 (Co), all close to the value predicted by the oversimplified oscillator model. Recent quantum calculations suggest that the vibrational modes at low wavenumbers are affected in a non-negligible way by the contribution of the tetrahedra (Prencipe et al., 2012). Modes at wavenumbers in the 290 - 340 cm^{-1} range can be associated to tetrahedral tilting, while in the range 390-460 cm^{-1} they are largely due to O-Ge-O bending motion. In the lowest range, the modes are attributed to chain tilting and octahedral motions.

We can therefore tentatively subdivide the characteristic germanate Raman spectrum in five spectral regions as for silicates, with an analogous correspondence of vibrational modes (Figures 4.1-4.2):

1) R1 (880-640 cm^{-1}): Ge-O_{nbr} stretching modes, that are internal vibration modes of GeO_4;

2) R2 (640-480 cm^{-1}): stretching/bending modes of Ge-O_{br}-Ge bonds;

3) R3 (360-240 cm^{-1}): motions of the cations in M2 and M1 sites correlated with tetrahedral chain motion and tilting tetrahedra;

4) R4 (480-360 cm^{-1}): O-Ge-O vibrations;

5) R5 (below 240 cm^{-1}): lattice modes.

Our calculation has been recently confirmed by lattice dynamics simulation by Oreshonkov et al. (2015).

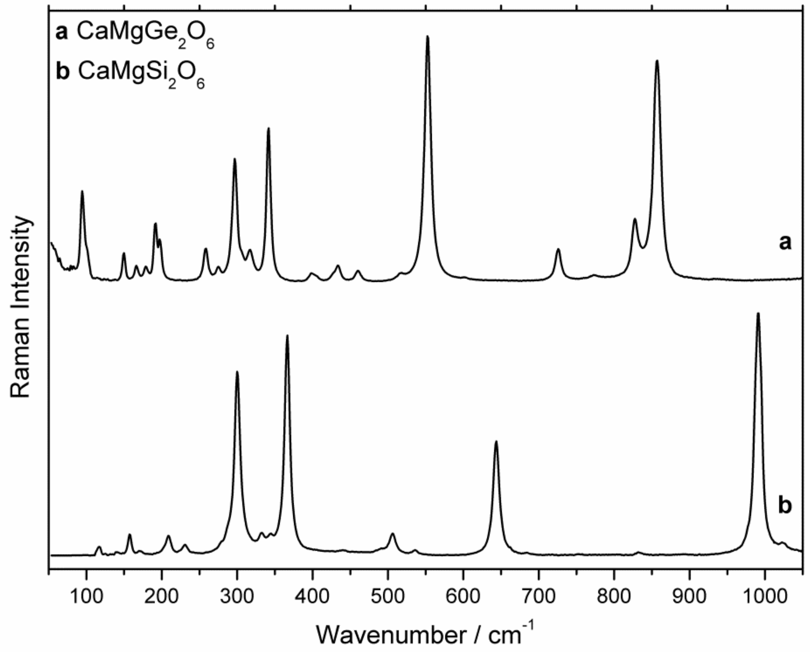

Figure 4.1: Raman spectra of CaMgGe$_2$O$_6$ (a) and CaMgSi$_2$O$_6$ (b).

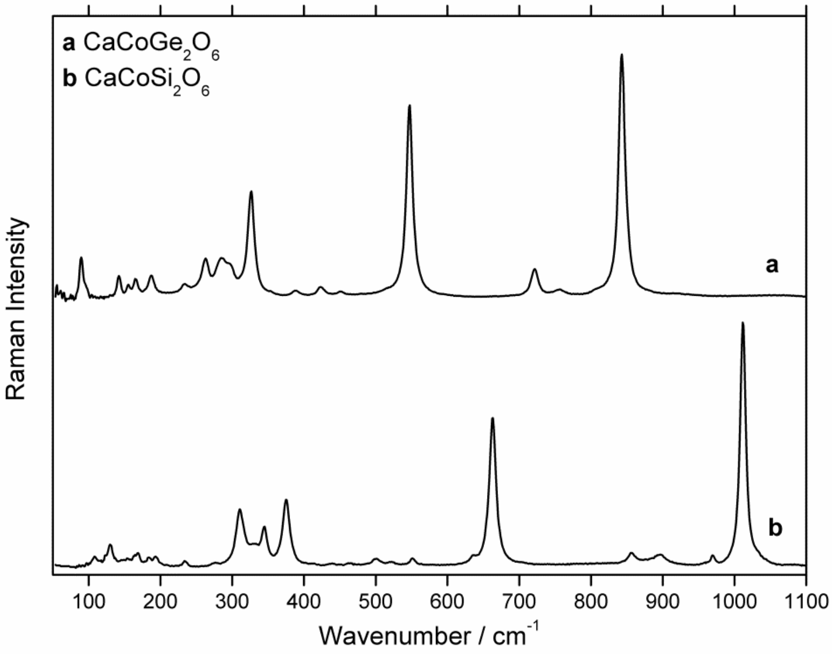

Figure 4.2: Raman spectra of CaCoGe$_2$O$_6$ (a) and CaCoSi$_2$O$_6$ (b).

4.2 High pressure behaviour in Raman experiments on $CaCoGe_2O_6$ and $CaMgGe_2O_6$ pyroxene, compared to the corresponding silicates

Clinopyroxenes are known to show a variety of phase transitions as a function of temperature and pressure, and the research on silicates synthesized at high pressures and temperatures plays a major role to understand the Earth's interior. The first experiments on common rock-forming silicates at pressures up to 10 GPa revealed striking changes in mineral structure and properties. Investigation of SiO_2, for example, demonstrated the transition from a relatively open framework (of corner-sharing Si-tetrahedra) in quartz to the dense rutile-type structure of stishovite, with edge-sharing chains of silicate octahedra (Stishov 1995; Hazen 1993; Stishov and Popova, 1961). The corresponding increase in density, higher than 66%, *i.e.* from 2.65 to 4.41 g/cm^3 between 0 and 8 GPa, has strong geophysical implications for the interpretation of seismic velocity data. In this section, we describe the vibrational changes in Raman spectra of Ge and Si- diopside and $CaCoGe_2O_6$ and $CaCoSi_2O_6$ in response to the applied pressure.

4.2.1 Crystal structure of the analysed samples

The samples analyzed are: synthetic $CaCoSi_2O_6$ single crystal, natural $CaMgSi_2O_6$ single crystal from a rodingitic rock sampled at Bellecombe (Aosta Valley), synthetic $CaMgGe_2O_6$ powder and synthetic $CaCoGe_2O_6$ single crystal.

Structural and chemical analyses have been reported for $CaCoSi_2O_6$ in Mantovani (2013), for $CaMgSi_2O_6$ in Prencipe et al. (2000), for $CaCoGe_2O_6$ in Redhammer et al. (2008), whereas further details on the synthesis and characterization of $CaMgGe_2O_6$ will be given in a forthcoming paper about crystallographic structure of calcium germanate. The data about this structure were personal communications of G. Redhammer.

All the samples are monoclinic with symmetry $C2/c$.

4.2.2 Experimental

An ETH-type diamond anvil cell (DAC; Miletich et al., 2000) (Figure 4.3), was used for the high-pressure Raman experiment. Stainless-steel T301 foil, 250 μm thick, pre-indented to a thickness of about 100 μm, with a 300 μm hole obtained by electro-spark erosion, was used as a gasket. Type-II diamonds were used as anvils (culet ∅ 600 μm). One crystal of each sample (approx. 100 x 60 x 50 μm^3) was placed in the gasket hole along with some ruby chips for pressure measurements by the ruby-fluorescence method (precision of ± 0.05 GPa) (Mao et al., 1986). Two experiments were performed: the first for the two silicates and the second for the two (Figure 4.4). Methanol:ethanol = 4:1 mixture was used as hydrostatic pressure-transmitting fluid (Angel et al., 2007; Gatta, 2008; Gatta, 2010). Room and high-pressure Raman spectra were collected in the pressure range 0.0001- 7.6 GPa for silicates and 0.0001- 8.27 GPa for germanates (in compression mode) using an Olympus BX40 microscope attached to a Jobin- Yvon Horiba LabRam confocal Raman spectrometer. A Nd:YAG diode laser at 473.1 nm using intracavity frequency doubling of 946 nm (maximum power 100 mW) was used for excitation (see technical details in the previous chapter). The spectral resolution was 3.5 cm^{-1}.

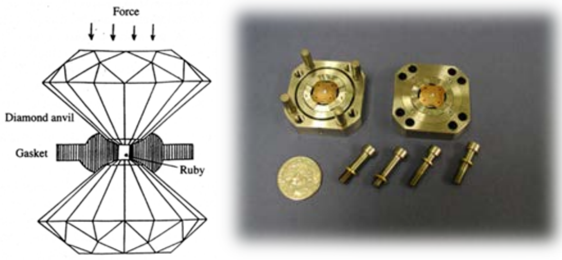

Figure 4.3: scheme (left) and the assemblage parts (right) of an ETH-type diamond anvil cell (DAC).

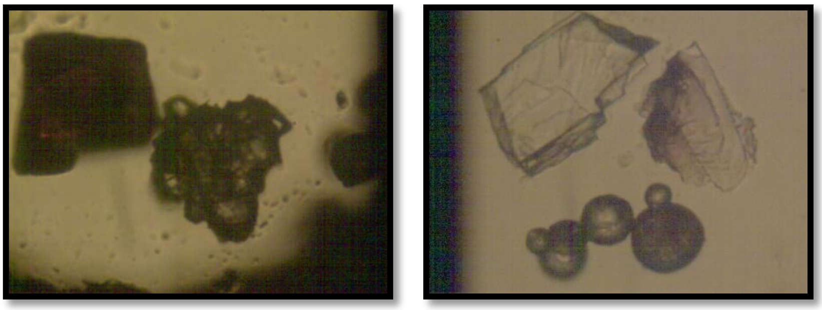

Figure 4.4: the Ge-samples (left) and Si-samples (right) together with some ruby chips in the gasket hole of the DAC. Photo at 50X.

On the basis of the single crystal nature of the sample and its monoclinic symmetry, a dependence of the orientation of the crystal on the intensity of the Raman bands is expected. No special care was taken to enhance or to minimize possible polarization effects. Each Raman spectrum was collected keeping fixed the sample orientation so that the changes in relative intensities may be taken as representative of the pressure induced changes. This was not possible for $CaMgGe_2O_6$ powder and, for example, in this case the data at 2.34 GPa were discarded. The Raman spectra of pyroxenes under investigation and the ruby fluorescence were calibrated at each measurement using the emission lines of a Zn spectroscopic lamp. The position of the fluorescence and Raman bands was measured using a Gauss-Lorentzian deconvolution procedure with the LabSpec v. 5 software.

4.2.3 Results and discussion

For all the four pyroxenes here investigated, the Raman spectra collected within the *P*-range investigated did not show evidence of phase transitions in response to the applied pressure.

Raman spectra of silicate pyroxenes under ambient pressure are widely investigated (Mantovani et al., 2014; Prencipe et al., 2012; Tribaudino et al., 2012; Wang et al., 2001; Huang et al., 2000).

The Raman spectra of Ge- pyroxenes are discussed in the previous paragraph.

The Raman setup did not enable the identification of all the features present at ambient condition: a general deterioration of the Raman signals when pressure increased was observed and some Raman features could not be detected. On the other hand, additional Raman bands at 880 and 1000 cm^{-1} were observed and assigned to the methanol-ethanol pressure-fluid. In the raw data, the strong peak centred at 1332 cm^{-1} due to the diamond anvils is obviously clearly visible.

The Raman spectra of the samples during compression are reported in Figures from 4.5 to 4.8.

$CaMgSi_2O_6$

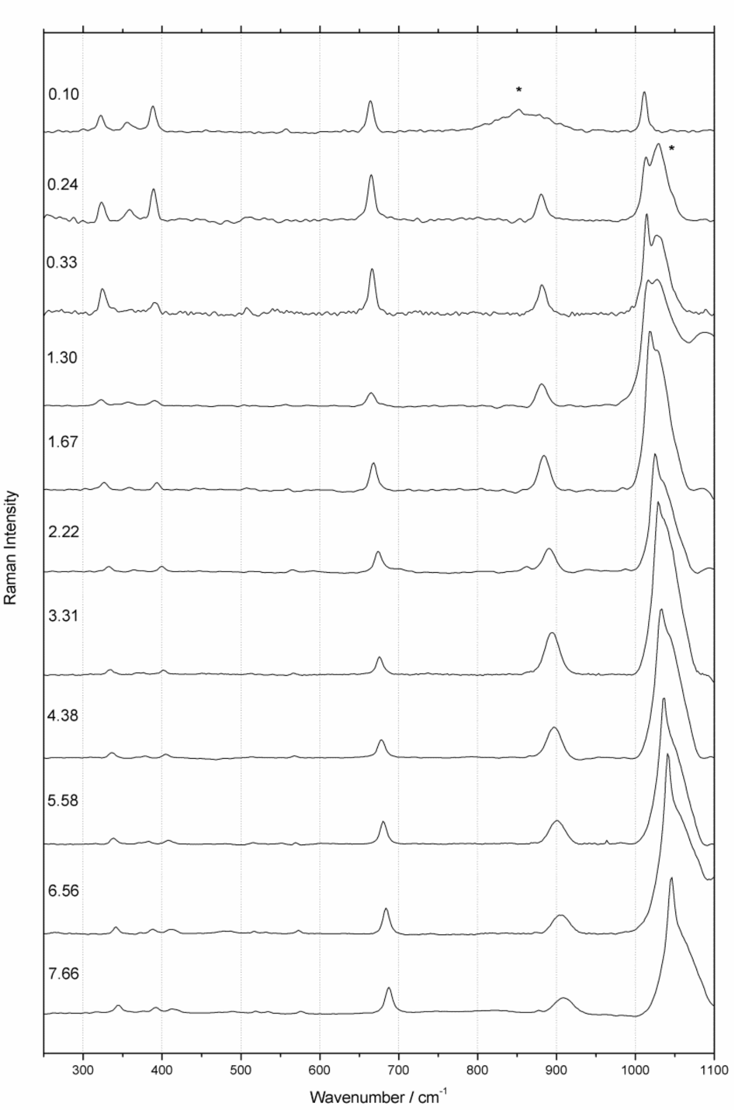

Figure 4.5: Raman spectra of $CaMgSi_2O_6$ upon compression. The pressure values are in GPa.The asterisks label spurious Raman features due to the medium.

The evolution of the Raman spectra of $CaMgSi_2O_6$ with pressure (Figure 4.5) shows the following distinct changes: the intensities of the dominant modes at low wavenumbers and that at about 665 cm^{-1} decrease with *P*, whereas the intensity of the peak at 1012 cm^{-1} is almost preserved. No significant change in the peaks width is observed. The Raman shift with pressure for bending mode is ~ 22 cm^{-1}, whereas for the stretching band is 33 cm^{-1} between 0 and 7.66 GPa. The Raman spectra are affected by spurious features due to the pressure medium at about 900 and 1000 cm^{-1}.

$CaMgGe_2O_6$

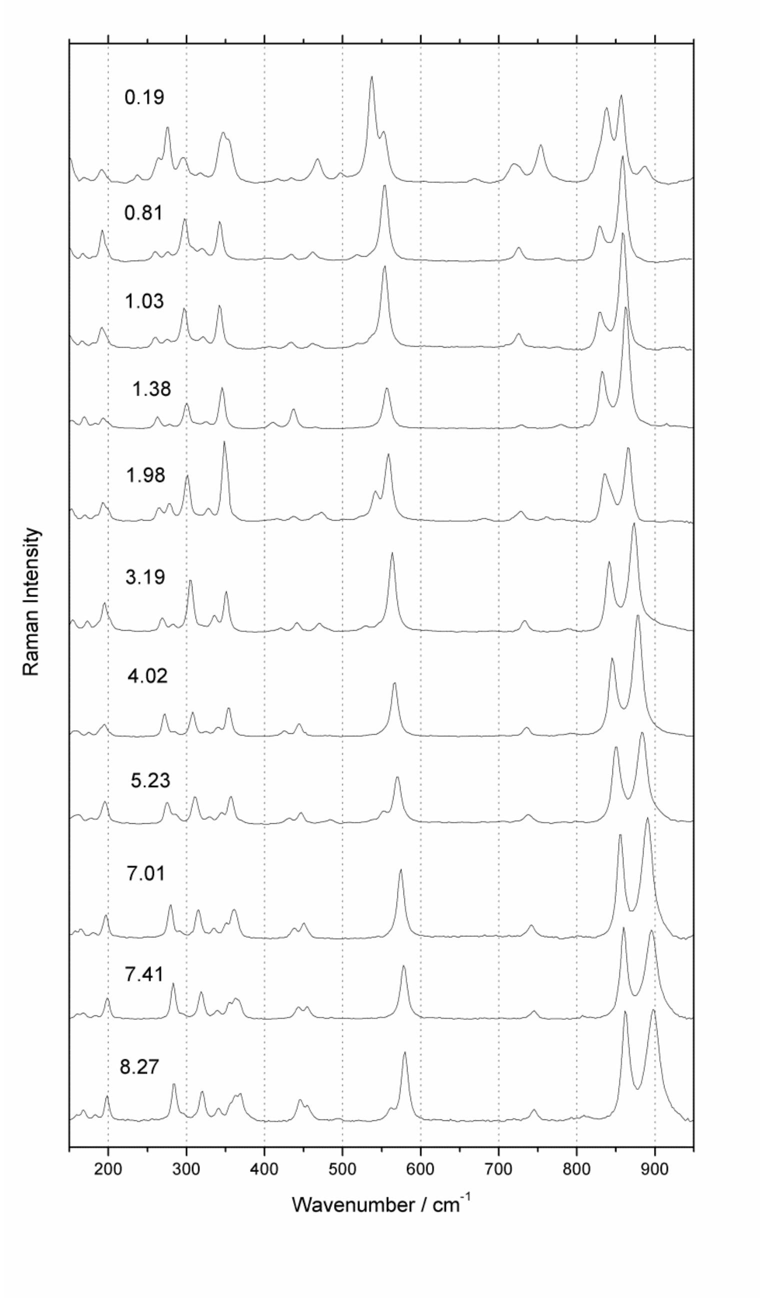

Figure 4.6: Raman spectra of $CaMgGe_2O_6$ upon compression. The pressure values are in GPa.

The Raman spectra of $CaMgGe_2O_6$ upon compression (Figure 4.6) show more Raman peaks than those observed for Si-diopside.

In the wavenumber region, between 250 and 400 cm^{-1}, the intensities of many peaks change; this could be caused by the polycrystalline form of the sample (not single crystal) and by its inhomogeneity. The bending mode of Ge-O_{br}-Ge blue-shifts of ~ 27 cm^{-1}; even more (40 cm^{-1}) for the stretching symmetric mode Ge-O_{nbr} at 857 cm^{-1}.

$CaCoSi_2O_6$

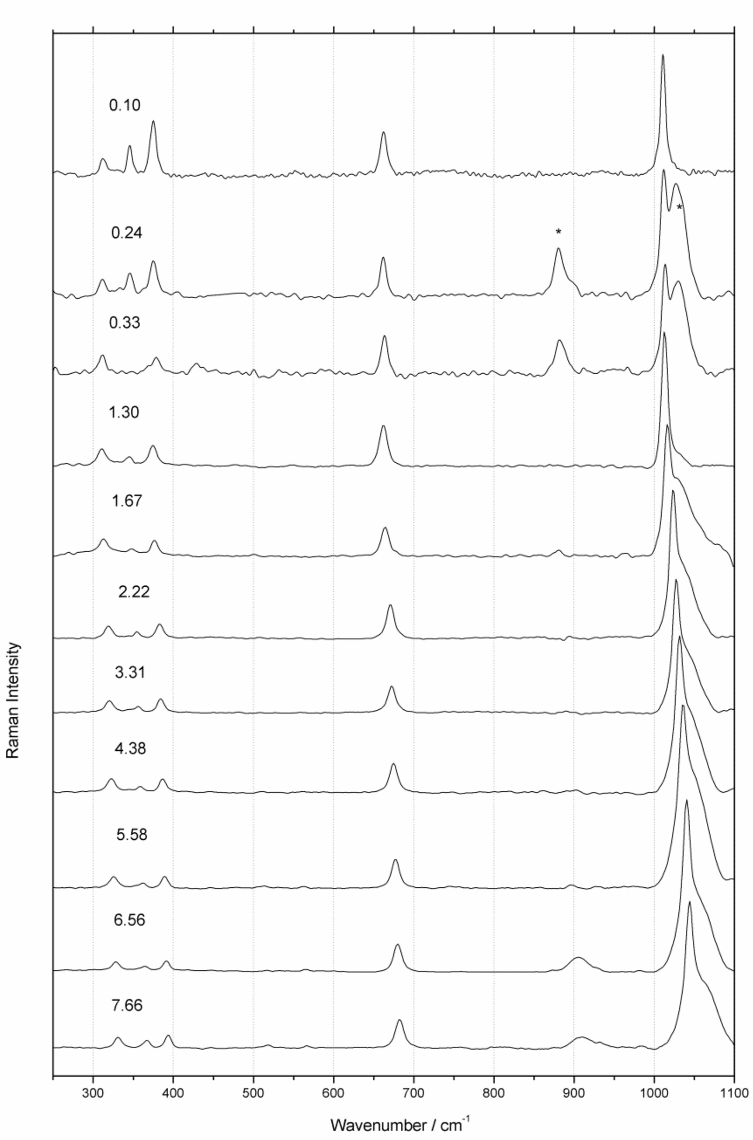

Figure 4.7: Raman spectra of $CaCoSi_2O_6$ upon compression. The pressure values are in GPa. The asterisks label spurious features due to the medium.

The spectra of $CaCoSi_2O_6$ at the different pressures are very similar each other. Below 800 cm^{-1}, the dependence of the wavenumber on the pressure is almost the same as Si-diopside. The bending peak upshifts of ~ 20 cm^{-1} while the stretching mode of 33 cm^{-1}. The Raman spectra are affected by spurious features due to the pressure medium at about 900 and 1000 cm^{-1}.

CaCoGe$_2$O$_6$

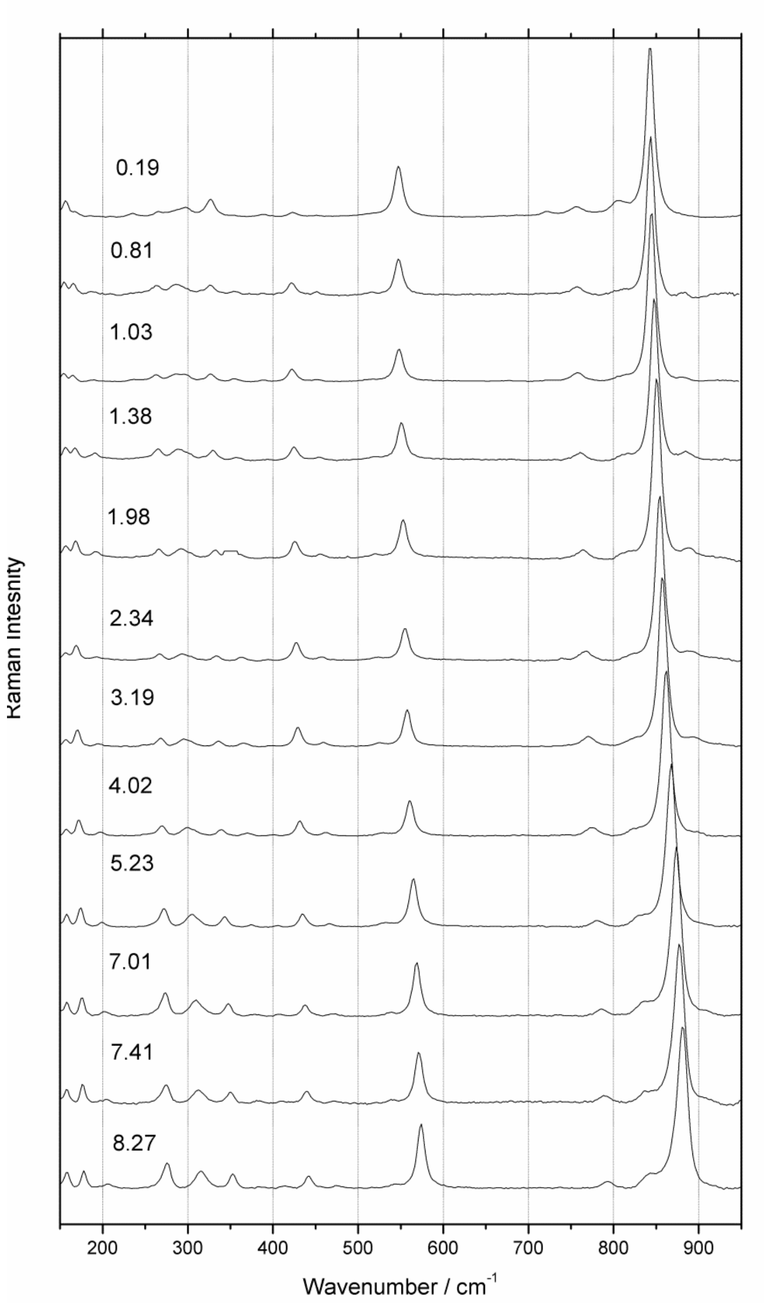

Figure 4.8: Raman spectra of CaCoGe$_2$O$_6$ upon compression. The pressure values are in GPa.

Raman spectra of CaCoGe$_2$O$_6$ upon compression are shown in Figure 4.8. The intensities of the dominant modes at low wavenumbers increase with pressure and, at high pressure, a doublet clearly emerges in the region 155-180 cm^{-1}. Again, the largest shift in wavenumber is displayed by the stretching mode at 840 cm^{-1} (Δ ~33 cm^{-1}). The bending mode blue-shifts of ~ 27 cm^{-1}.

While high-pressure XRD investigations on single crystal on Ca-silicate clinopyroxenes (Tribaudino et al, 2001; Serghiuo et al., 2000; Zhang et al, 1997; Levien and

Prewitt, 1981) are available, only a few HP Raman studies have been reported (Chopelas and Serghiou, 2000). As far as we know, there are no high pressure XRD and Raman data on Ca-germanate pyroxenes.

About HP Raman study on diopside, Chopelas and Serghiou, (2000) reported that no phase transition occurs below 10 GPa. The evolution of our spectra with increasing pressure does not reveal changes with respect to the number of bands or splitting of modes with pressure.

Also the other samples analyzed do not exhibit any phase transition: all the peak positions vary linearly as a function of pressure and no change of slope occurs during the compression.

All the peaks blueshift towards higher wavenumbers on increasing pressure: the major shifts are attributed to the chain bending (Ge-O_{br}-Ge) and stretching modes (Ge-O_{nbr}) for all the samples.

Concerning the crystallographic structure of $CaMgSi_2O_6$, no phase transition seems to be indicated by structural data below 10 GPa (Tribaudino et al, 2001; Serghiuo et al., 2000; Zhang et al, 1997; Levien and Prewitt, 1981). It has been reported (Levien and Prewitt*,* 1981) that the unit-cell parameters decrease monotonically with increasing pressure. The unit-cell compression was observed to be accommodated by the (different) compression of the three independent polyhedra. The polyhedral volumes of M(1) and M(2) both decrease approximately by 5%, whereas that of the Si-tetrahedron decreases only by 1%, and the silicate-chain kinking increases in response to the applied pressure.

Diopside shows a minor tetrahedral compression, higher octahedral compression, and a more pronounced silicate-chain kinking (Levien and Prewitt*,* 1981). The compression of the structure is controlled by the directions and compressibilities of the bonds in M(1) and M(2) polyhedra, and not by the chains of silicate tetrahedra. The least compressible M-O bonds can be correlated with the direction of minimum compression in the diopside structure; the most compressible bonds [M(2)-O(3C2,D2)] show the highest compression, (Levien and Prewitt*,* 1981) and the M2-polyhedron becomes smaller and more regular with increasing pressure (Tribaudino et al., 2000).

At pressures between 5 and 10 GPa, diopside shows a change in the main deformation axes on the (010) plane, at angles about 55° from *c* axis, but this change is continuous and related to changes in the microscopic compression mechanisms. The important mechanism of deformation in *C*2/*c* clinopyroxenes with pressure is the shift of tetrahedral chains facing on the M2 polyhedron, which accounts for the major part of the changes in β angle and hence the deformation on (010) (Tribaudino et al., 2000).

The Si-O bond lengths in tetrahedra decrease as a function of pressure (1.637(1) – 1.630(2) Å) as the volume of tetrahedra (Levien and Prewitt, 1981).

The bond lengths decrease influences the vibrational modes (Guyot et al., 1986). In particular, the force constant k depends on the interatomic distance d as: k α d^{-3}. The Raman frequency is roughly proportional to the square root of the ratio between the force constant and the reduced atomic mass: when the bond lengths decrease, the wavenumber increase, because of higher repulsion within the polyhedra.

In particular, the stretching mode T-O_{nbr} shows the highest shift; even if the M polyhedra are more compressible, the major wavenumber changes are related to the chain and tetrahedral modes. This can be explained looking at the pyroxene structure: chains of edge-shared MgO_6 octahedra and CaO_8 octahedra run parallel to the silicate chains. The calcium site is quite distorted with four long and four short bonds, with average bond length differing by 12%. The Ca octahedra becomes more regular upon compression (Levien and Prewitt, 1981) and the kinking angle decreases in order to accomodate this crystallographic change in M2 polyhedron. Furthermore, the inter-tetrahedral distances Si-Si decrease, in response to a decrease of the intra-tetrahedral angles (O-Si-O) and inter-tetrahedral angles (Si-O3-Si and O3-O3-O3).

Raman spectroscopic studies on *C*2/*c* Si-clinopyroxenes reveal that the Raman shift of the Si-O-Si stretching vibration (at 670 cm^{-1}) is linearly dependent on the Si-Si distance: it increases with a decrease in the Si-Si distance (Ohashi, personal communication).

All these mechanisms lead to an increase of the wavenumber of the bending mode (T-O_{br}-T) and even more of the stretching mode Si-O_{nbr}.

This mechanism can be assumed also for the other samples of pyroxene, because they possess the same symmetry and unique tetrahedral chain.

For this reason, we focused our attention in particular to the peaks related to tetrahedral motions (chain bending and stretching modes) and we calculate the slope $\Delta v/\Delta P$ of the observed band positions, because the wavenumber of the other peaks changes less with respect to the tetrahedral modes.

The stretching modes show the highest shift, and this could be related to the compression of T-O bonds within the tetrahedra. The wavenumber of the bending modes increases with decrease of T-T distances, and so with a decrease of kinking angle and of Si-O3-Si angles (Ohashi and Osawa, 1981).

Within all the samples, Ge-pyroxenes show the higher shift in peak position (Figure 4.9 and Table 4.1). This can be related to the fact that germanates usually show the high-pressure configurations of their analogous silicates. As a consequence, germanates are more compressible than the iso-structural silicates. This fact is confirmed by the study on high pressure of Si-quartz by Levien and Prewitt (1980). As pressure is increased, the geometry of SiO_2 quartz structure approaches that of the low pressure GeO_2. Another confirmation that germanates are more compressible can be found if we consider the linear thermal expansion coefficients. Redhammer et al. (2010b) studied $LiFeGe_2O_6$ and $LiFeSi_2O_6$: the Ge-sample shows the highest coefficients.

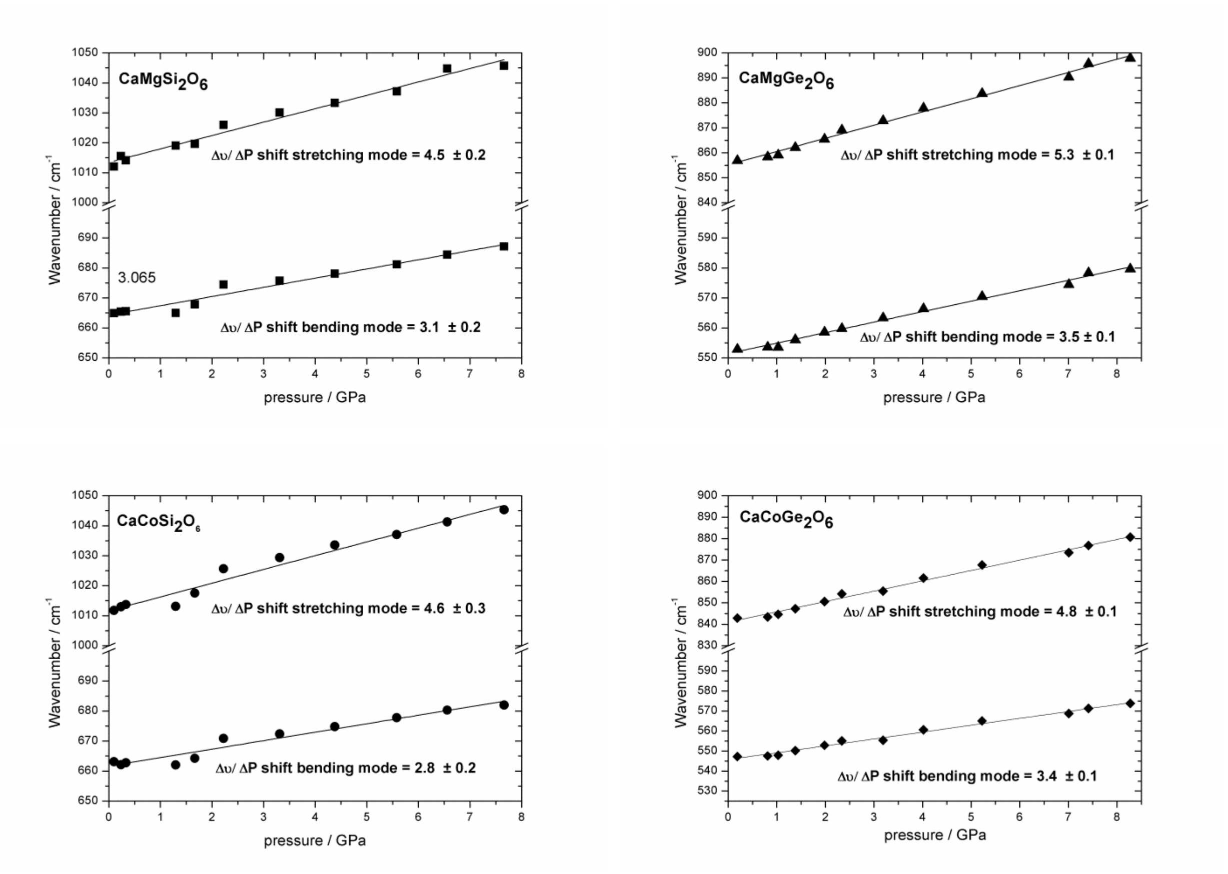

Figure 4.9: Raman shifts for selected bands (Ge-O$_{br}$-Ge bending and Ge-O$_{nbr}$ stretching) as a function of pressure in the four samples of pyroxenes. Lines correspond to the linear fits of the Raman shift of modes, and the values along with uncertainties (stated as $cm^{-1}GPa^{-1}$) correspond to the fitted slope of the linear fits.

Table 4.1: Δv/ΔP shift ($cm^{-1}GPa^{-1}$) with standard error and R squared of the main vibrational modes.

Δv/ΔP shift / Samples	$CaMgSi_2O_6$	$CaMgGe_2O_6$	$CaCoSi_2O_6$	$CaCoGe_2O_6$
Bending modes	3.1 ±0.2	3.5 ± 0.1	2.8 ± 0.2	3.4 ± 0.1
Stretching modes	4.5 ± 0.2	5.3 ± 0.1	4.6 ± 0.3	4.8 ± 0.1
R^2	$R^2 = 0.96$	$R^2 = 0.99$	$R^2 = 0.96$	$R^2 = 0.99$

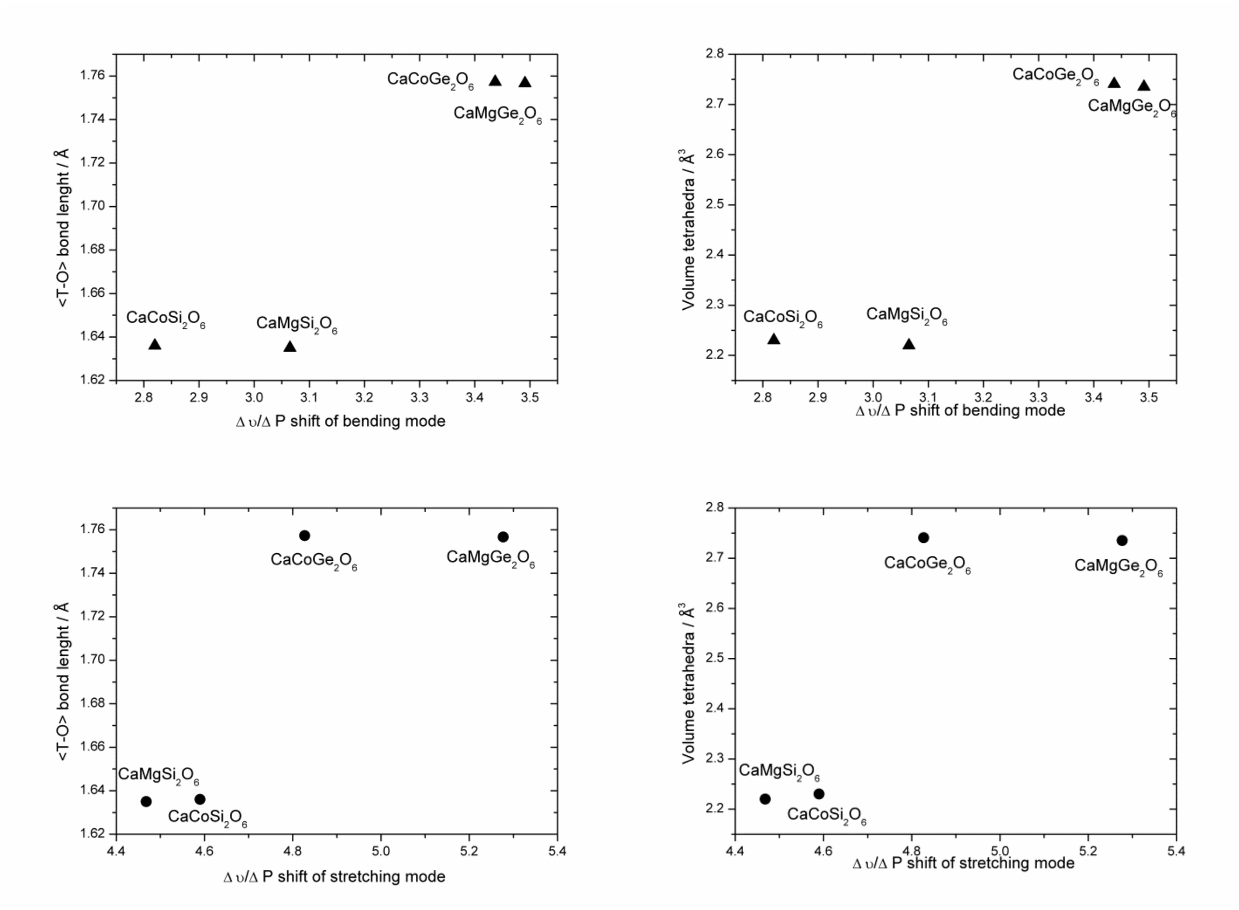

Figure 4.10: plot of <T-O> bond length and volume of tetrahedra vs Δv/ΔP of bending and stretching mode.

The results in Table 4.1 and Figure 4.10 show that germanates are more compressible than silicates. Furthermore, $CaCoGe_2O_6$ is less compressible than $CaMgGe_2O_6$, while $CaCoSi_2O_6$ is more compressible than $CaMgSi_2O_6$.

The overall aspect of the highest pressure spectrum is very similar to the room pressure one, in terms of number of peaks and relative intensity. This evidences that the symmetry has not changed during the compression.

A change in the Raman shift is related to crystallographic changes occurred during compression. The major shifts in wavenumber are attributed to the stretching mode and then to the bending mode. The other peaks change less their position and are difficult to follow at increasing pressure.

To clarify the crystallographic changes during the compression, HP X-ray diffraction will be needed.

4.3 Raman Spectroscopy in Ge monoclinic pyroxenes

The Ca end-members *C*2/*c* pyroxenes, with a bivalent cation in M1 site, have been extensively investigated for their physical properties, being Ca the most common ion in the M2 site of natural pyroxenes. Here, we report the Raman spectra of a series of synthetic *C*2/*c* Ge-pyroxenes, with M2 site always occupied by Ca and M1 by cations with increasing atomic mass Mg<Mn<Fe<Co<Ni<Zn and increasing radii (Zn<Ni<Mg<Co<Fe<Mn), in a six-fold coordinated (Shannon, 1976), high spin configuration polyhedron. This work is the first part of a project that will include ab initio quantum mechanical calculations of pyroxene mineral species and was published in: Journal of Raman Spectroscopy, *46: 586-590,* E. Lambruschi, I. Aliatis, L. Mantovani, M. Tribaudino, D. Bersani, G. J. Redhammer, P. P. Lottici (2015). Raman spectroscopy of $CaM^{2+}Ge_2O_6$ (M^{2+}=Mg, Mn, Fe, Co, Ni, Zn) clinopyroxenes (http://onlinelibrary.wiley.com/doi/10.1002/jrs.4681/full).

4.3.1 Crystal structure of the analysed samples

Raman spectra were taken on synthetic powders of clinopyroxenes $CaM^{2+}Ge_2O_6$ (M^{2+} =Mg, Mn, Fe, Co, Ni, Zn), space group *C*2/*c*, Z=2 in the primitive cell. The syntheses were carried out in a furnace at room pressure in a temperature range between 1200 and 1350 °C. The average size of the grains was tens of micrometer in length. They were first optically examined and then structurally characterized by single crystal X-ray and powder diffraction. The detailed crystal structure of $CaFeGe_2O_6$ was published by Redhammer et al. (2013), whereas further details on the syntheses and characterization of the samples with M^{2+} =Mg, Mn, Co, Ni, Zn are personal communications by G. Redhammer.

4.3.2 Experimental

Raman measurements were carried out using a Horiba Jobin-Yvon LabRam. The 632.8 nm line of a He-Ne laser was used for excitation. Laser power on the sample surface was less than 1 mW (see technical details of the instrument in chapter 4.1.2).
The spectra of *C*2/*c* clinopyroxenes $CaM^{2+}Ge_2O_6$ (M^{2+}= Mg, Mn, Fe, Co, Ni, Zn) are shown in Figure 4.11 and peak wavenumbers are given in Table 4.2. A total of 22 peaks were identified in the range 90-900 cm^{-1}.

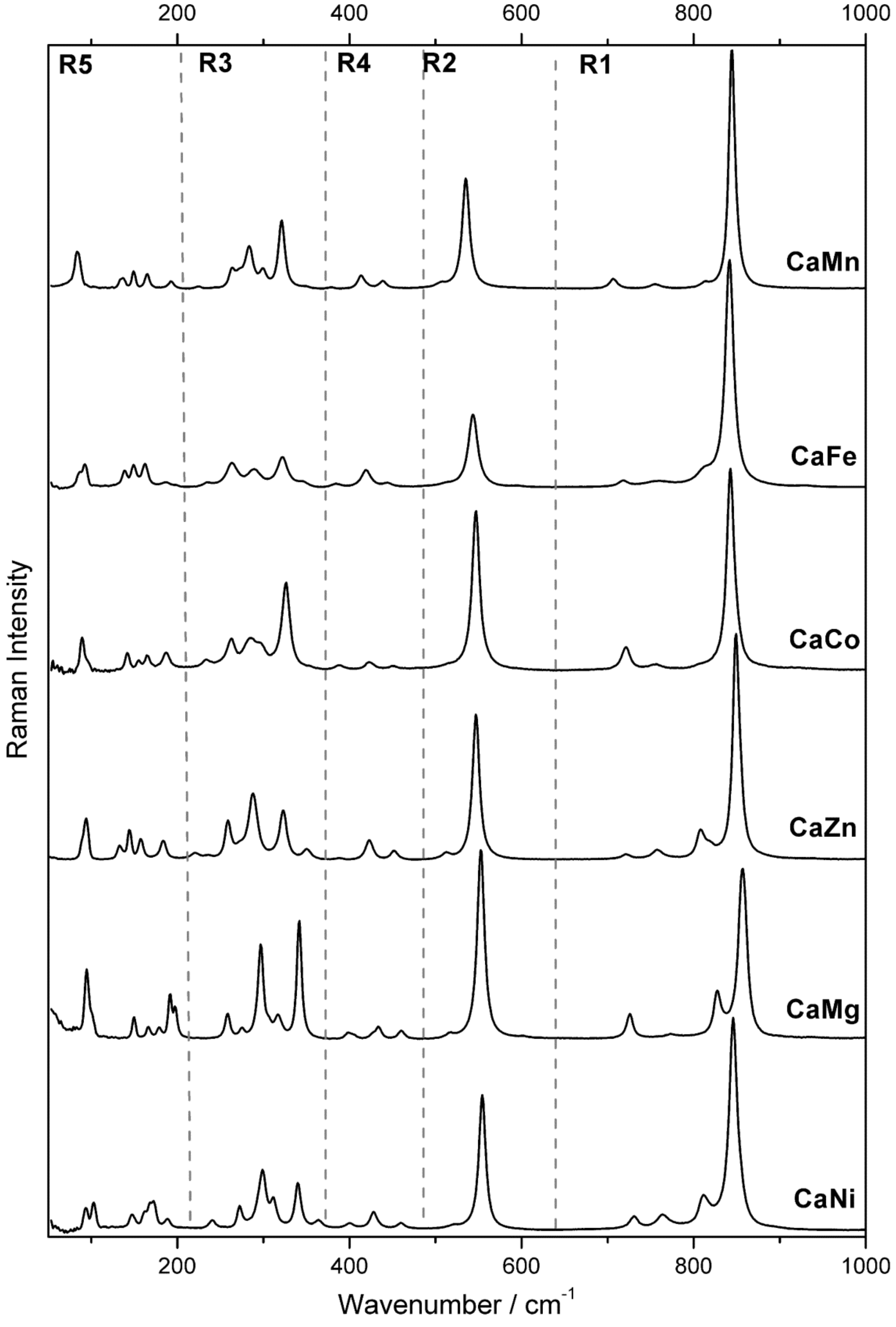

Figure 4.11: Raman spectra of CaM^{2+}Ge$_2$O$_6$ (M^{2+} =Mg, Mn, Fe, Co, Ni, Zn).

Table 4.2: peak positions (in cm^{-1}) in the Raman spectra of Ca germanates.

$CaMgGe_2O_6$	$CaMnGe_2O_6$	$CaFeGe_2O_6$	$CaCoGe_2O_6$	$CaNiGe_2O_6$	$CaZnGe_2O_6$
95	84	87	89	94	94
101		93	94	103	
150	137	139	142	148	133
166	149	149	155	161	144
179	165	162	165	168	158
191	193	187	187	173	184
198				189	
					221
	225	235	234	240	235
258	264	264	262	272	259
275	273		285		272
297	283	289	298	299	288
307	299		317	312	
317	321	322	326	340	323
342	350	345		364	351
400	379	385	388	400	388
433	414	419	423	428	423
460	438	443	453	460	452
517	507	513	514	522	512
553	535	544	547	554	547
726	707	719	721	731	721
772	755	759	755	764	757
828	812	812	809	812	808
					819
857	845	842	843	846	850

4.3.3 Results and discussion

The spectra for $CaM^{2+}Ge_2O_6$ (M^{2+}= Mg, Mn, Fe, Co, Ni, Zn) germanates (Figure 4.11) show significant differences in the wavenumbers of the modes referred to equivalent vibrational patterns in all the series, because of the substitution of the cation in the M1 site. The substitution affects the chain bending wavenumber and, to a lesser extent, also the tetrahedral stretching modes which, in a rough approximation, are often considered dependent only on the Ge-O bond. The pyroxene structure has an inherent flexibility, and compositional changes within one polyhedron affect the oxygen positions also in other polyhedra: Raman modes, obviously, cannot be simply described by the vibrations within a polyhedron (Prencipe et al., 2012).

To get a deeper insight on the effect of the substitutions, we have tested the relationship between the ionic radius of the cations in the M1 site or the average M1-O bond distance and the wavenumber of the most relevant peaks.

An approximate inverse correlation is found for the T-O_{br}-T bending (chain bending) modes at about 550 cm^{-1} (Figure 4.12): with increasing ionic radius (or average M1-O distance) a decreasing wavenumber is observed.

The tetrahedral chain is linked to the octahedral one via common O2 oxygen atoms (Figure 4.14). Any change in the size of the octahedra, in order to incorporate the cation with different ionic radius, causes different kinking of the tetrahedral chain (Redhammer et al., 2008). As shown in Figures 4.12-13, when the ionic radius for the cation in the M1 site and therefore the M1-O average bond distance increases, the kinking angle decreases consequently. The wavenumber of the chain bending mode decreases as the chain becomes more kinked, or the kinking angle decreases. The tetrahedral chain bending motion depends also on the Ge-Ge distance, in analogy with silicates (Ohashi and Sekita 1982): its wavenumber decreases with an increase in the Ge-Ge distance, but without any apparent linear behavior.

The lowest wavenumber of this mode is found in $CaMnGe_2O_6$, which has the smallest kinking angle and the largest atomic radius and the highest Ge-Ge distance.

This is an opposite trend respect to the behaviour under pressure. The reason could be that, when the chain structure is under pressure, the crystallographic changes involve all the structure, and the variations within the structure are more significant and continuous, because at high pressure the 4-coordinated tetrahedra will be trasformed into octahedra (Chopelas and Serghiou, 2002). In this case we substitute a cation in M2 and the changes are limited to an accomodation of this cation.

No simple relationship is found between the atomic mass of the cations and the chain bending mode wavenumber.

As outlined before, the strong peak at ~850 cm^{-1}, ascribed to a T-O$_{nbr}$ stretching mode, should be unaffected by the change in the M1 cation, being the tetrahedron a rather stiff unit (Cameron et al., 1973). However, the T-O$_{nbr}$ stretching modes of $CaFeGe_2O_6$ and $CaMgGe_2O_6$ pyroxenes differ by 15 cm^{-1} (Table 4.2). The small variations in the tetrahedral bond lengths cannot explain this behaviour, and an effect of the mass of the M1 cation could hardly be invoked. Actually, in the Co and Mg pyroxenes the T-O stretching mode occurs at the same wavenumber (1012 cm^{-1}) (Tribaudino et al., 2012; Mantovani et al., 2014), in spite of the significant M1 mass difference. Preliminary quantum mechanical simulations show indeed poorer agreement between experiment and calculations for this high wavenumber mode in germanates with respect to silicates.

At low wavenumbers no relationship has been found between peak wavenumber and atomic weight or ionic radii: here it is very difficult to discriminate the contribution of the M1 cation to each mode. Recent quantum-mechanical simulations in silicate diopside (Prencipe et al, 2012) show that the modes at low wavenumbers cannot be assigned solely to the M1-O or M2-O motion, but they involve other polyhedra and the tetrahedral chain.

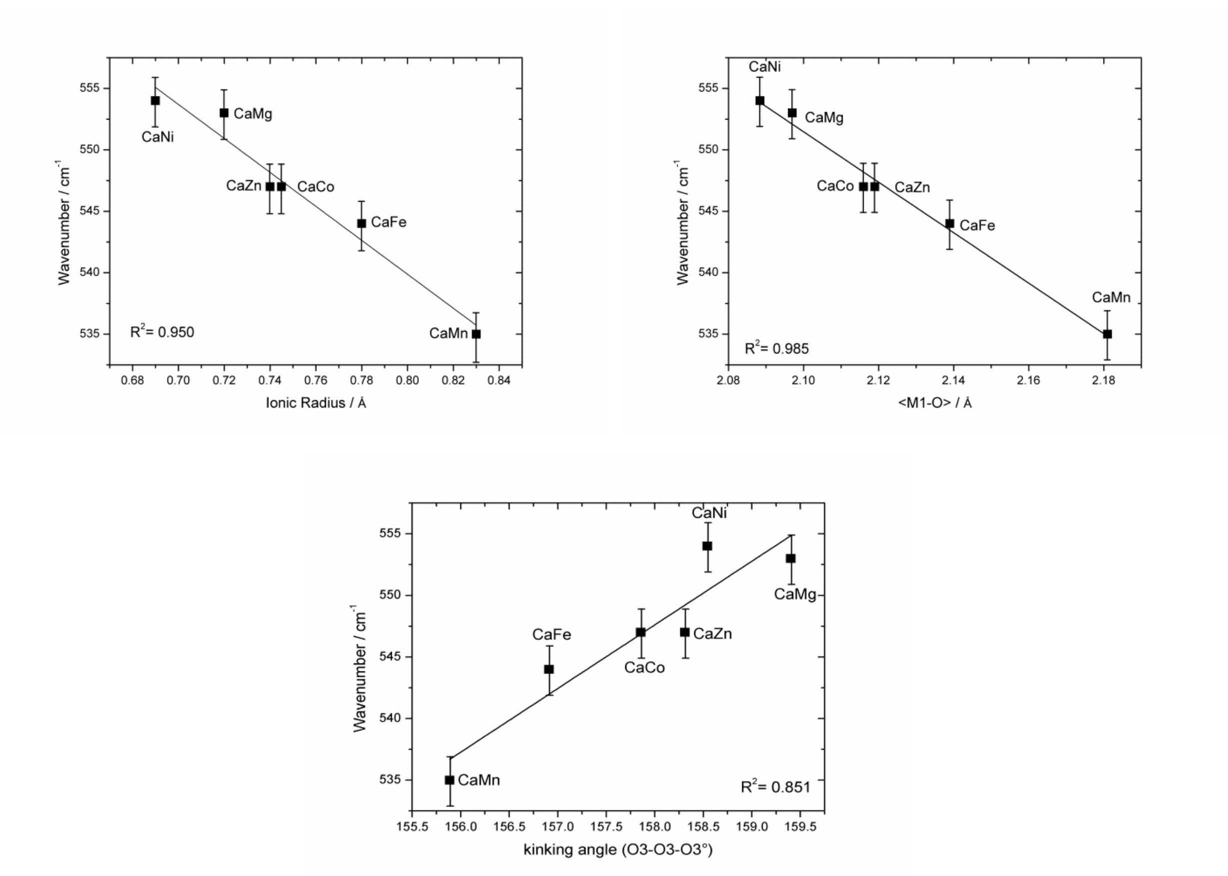

Figure 4.12: chain bending wavenumber in germanates vs. M1 ionic radius, average <M1-O> cation-oxygen bond distance and kinking angle.

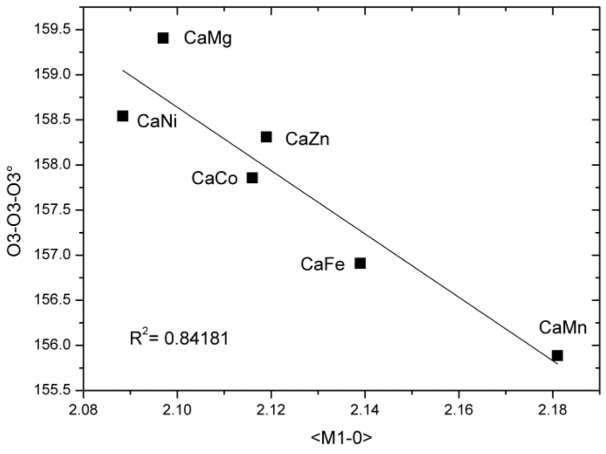

Figure 4.13: average bond length M1-O vs O3-O3-O3 chain kinking angle.

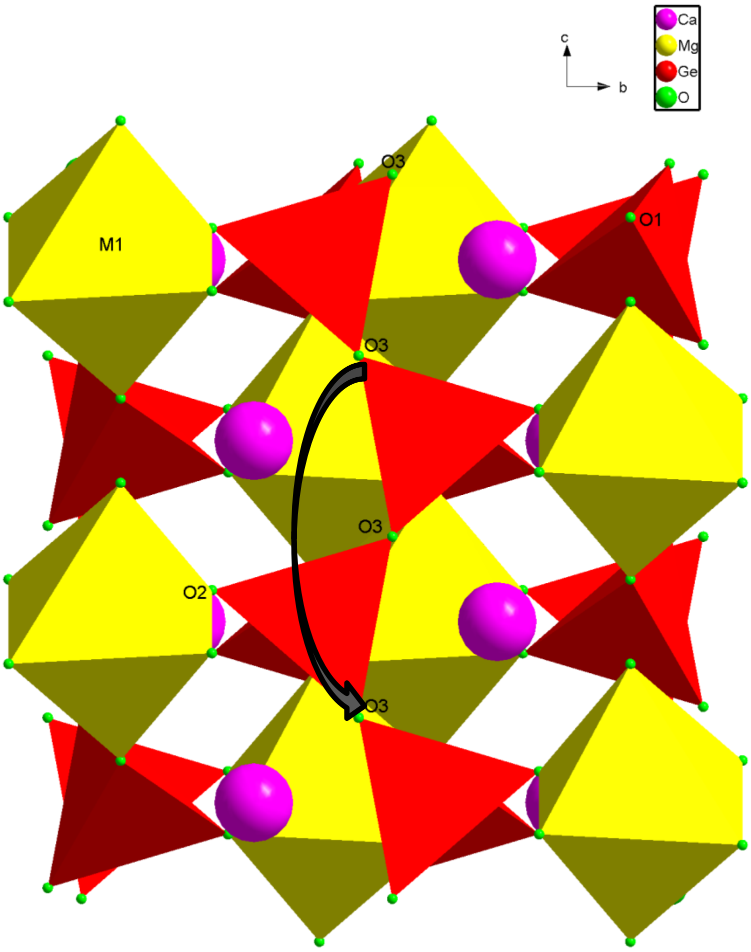

Figure 4.14: structure of Ge-clinopyroxene in cb plane view: the tetrahedral chain is parallel to c axis and characterized by the kinking angle O3-O3-O3 (the black arrow).

Part 2:

Magnetic Properties

Chapter V

MAGNETIC PROPERTIES OF $CaCoSi_2O_6$-$CoCoSi_2O_6$ PYROXENES

The investigations of pyroxenes systems have been essentially focused on mineralogical and crystallographic aspects. Only recently their magnetic properties attracted some attention. Most pyroxenes seem to be antiferromagnetic and complete magnetic structures are only known for few end-members of this class (Jodlauk et al., 2007).

The specific features and the variety of magnetic properties of pyroxenes are determined by their crystal structure, and in this paragraph the magnetic properties of the system $CaCoSi_2O_6$-$CoCoSi_2O_6$ will be discussed. In particular it will be investigated how the different amount of magnetic ion in the structure along the join, together with a structural phase transition, modifies the magnetic behaviour.

5.1 Characterization of the samples

The samples analysed were synthesized by L. Mantovani. The synthesis conditions and cell parameters are listed in Table 5.1.

This join was studied in order to obtain a model for the solid solutions between Ca and smaller divalent cations like Mg, Fe or Co (Mantovani, 2013). Ca,Co-pyroxenes have acquired a lot of interest because they are interesting candidates as ceramic pigments both for the strong resistance of the pyroxene structure and for the final pink colour given by the entrance of Co in the octahedral site.

Along this join a phase transition occurs at Co7 (*i.e.* $Ca_{0.3}Co_{1.7}Si_2O_6$): the pyroxenes symmetry changes from $C2/c$ to $P2_1/c$, due the substitution of a smaller cation in the M2 site. For the end-member fully occupied by cobalt, $Co_2Si_2O_6$, the symmetry is orthorhombic *Pbca.*

So, the aim of this study is to follow the changes in magnetic properties and discuss them with the relative crystallographic changes.

In literature there are only few studies that deal with the magnetic behaviour in pyroxenes within a solid solution (Wiedenman et al., 1986; Eeckhout et al., 2001) and the end member of this join were studied by Sawaoka et al. (1968) for $Co_2Si_2O_6$ and by Durand et al. (1996) for $CaCoSi_2O_6$.

Table 5.1: synthesis conditions and cell parameters (from PXRD) of the samples (from Mantovani, 2013).

Synthesis conditions					**Cell parameters**						
Sample	***Chemical composition***	***P (GPa)***	***T (°C)***	***t (h)***	***Simmetry***	***a (Å)***	***b (Å)***	***c (Å)***	***β (°)***	***V (Å³)***	***Measurement***
Co0	**Ca (M2 site)** Co **(M1 site)**	3	1200	6	*C2/c*	9.802(1)	8.962(1)	5.249(1)	105.40(1)	444.54(3)	M(T)
Co2	$\mathbf{Ca_{0.8}Co_{0.2}}Co_{1}$	3	1200	6	*C2/c*	9.791(1)	8.954(1)	5.246(1)	105.77(1)	442.58(8)	M(T), M(H)
Co4	$\mathbf{Ca_{0.6}Co_{0.4}}Co_{1}$	3	1200	4	*C2/c*	9.769(1)	8.964(1)	5.243(1)	106.46(1)	440.28(3)	M(T), M(H)
Co5	$\mathbf{Ca_{0.5}Co_{0.5}}Co_{1}$	3	1200	5	*C2/c*	9.753(1)	8.962(1)	5.239(1)	106.78(1)	438.41(9)	M(T), M(H)
Co7	$\mathbf{Ca_{0.3}Co_{0.7}}Co_{1}$	3	1350	7	*C2/c*	9.717(1)	8.952(1)	5.245(1)	107.92(6)	434.09(8)	M(T)
Co8	$\mathbf{Ca_{0.2}Co_{0.8}}Co_{1}$	3	1350	4	*P*2$_1$/*c*	9.707(1)	8.950(2)	5.238(1)	108.43(5)	431.7(1)	M(T), M(H)
Co10	$\mathbf{Co_{1}}Co_{1}$	3	1200	6	*Pbca*	18.298(2)	8.921(2)	5.203(1)		849.4(1)	M(T), M(H)

5.2 Squid Measurements M(H) and M(T)

Magnetometric measurements have been performed by means of a Quantum Design MPMSXL-5 SQuID magnetometer.

A SQuID (Superconducting Quantum Interference Device) is a very sensitive magnetometer used to measure extremely subtle magnetic fields, based on superconducting loops containing Josephson junctions. There are two principal magnetic measurements:

1. *M(T)* magnetization as a function of temperature and,
2. *M(H)* magnetization as a function of applied magnetic field.

Small amounts of each sample (7-20 mg) were put into polytrifluorethylene (KLF) containers and brought into measuring position using a straw.

M(T): magnetization as a function of temperature

An M(T) measurement is made by fixing the applied field H and measuring M at a series of T values.

Magnetic measurements were performed on bulk polycrystalline samples, operating only in standard dc mode,. Zero Field-Cooling (ZFC) and Field-Cooling (FC) magnetization measurements were carried out by the standard procedures: in the former the system is cooled from RT to 5 K with no applied magnetic field, then the selected field is switched on and magnetization measured in warming (ZFC); in the latter, starting directly at the end of the ZFC measurement, the data collection is performed upon cooling in the same field (FC). The ZFC/FC method is very useful for determining the temperature range over which the systems show irreversible transformations. Measurements were made in a sweep mode (2 K) for each experiment.

Specifically:

Zero field cooled (ZFC)

300-5 K, H= 0 Oe

5-300 K, H= 10 - 5000 Oe

Field Cooled (FC)

300-5 K, H= 10-5000 Oe

M(H): magnetization as a function of applied magnetic field

In-field magnetization was characterized by hysteresis loops measurements collected cyclically, spanning the field range -5 T to 5 T, starting from 5 T in sweep mode at 5 K.

5.3 Results

5.3.1 Thermal spontaneous magnetization at 10 Oe

The spontaneous magnetization measured for the two end-members $CaCoSi_2O_6$ and $Co_2Si_2O_6$, with a ZFC-FC protocol at 10 Oe, allows figuring out the magnetic behaviour of the pyroxene join.

Looking at Figures 5.1-5.2, the cobalt ion in the M2 site of the pyroxene structure is responsible for a clear modification of the system magnetism.

For the $CaCoSi_2O_6$ sample, a sharp magnetic transition has been detected at about 13 K with AFM behaviour, characterized by the typical cusp and by a lowering of the magnetization to non-zero values at lower temperatures (due to the polycrystallinity of the phase).

Differently, $Co_2Si_2O_6$ shows a double peaked ZFC curve typical of a system in which two different and independent contributions overlap (the first located again at 13 K, and the latter, more intense, at 45 K). The ZFC and the FC curve are significantly separated at low temperature (below the longe range ordering temperatures). This suggests that, despite the pure collinear AFM behaviour of the superexchange interaction involving Co ions in M1 site (intra-chain), the magnetic order developed by the cobalt ions in M2 site (intra-chain) is affected by weak ferromagnetism, due to the non-collinearity of the AFM interaction (Dzyaloshinskii-Moriya Effect - antisymmetric exchange interaction).

In magnetically ordered systems, this effect promotes a spin canting of antiparallel magnetic moments and thus, e.g., could be a source of weak ferromagnetic behaviour in an antiferromagnet.

The lack of a well-defined magnetic transition temperature implies that the inter-chain exchange integral is less intense than intra-chain exchange integral for both M2 - M1 sites.

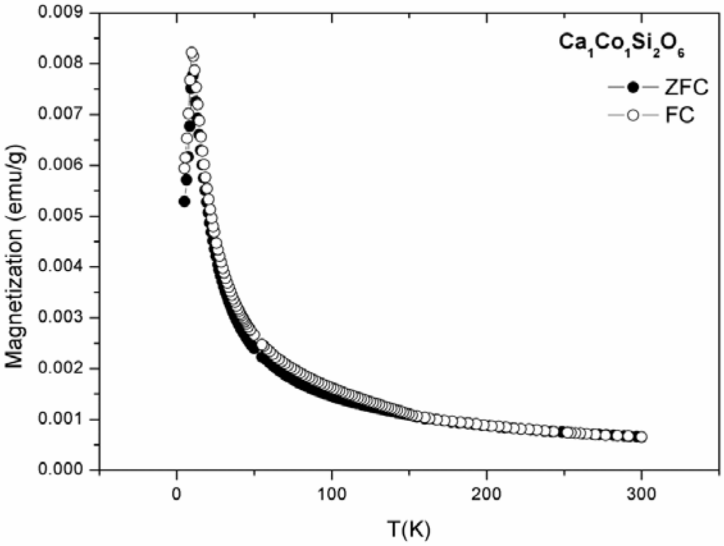

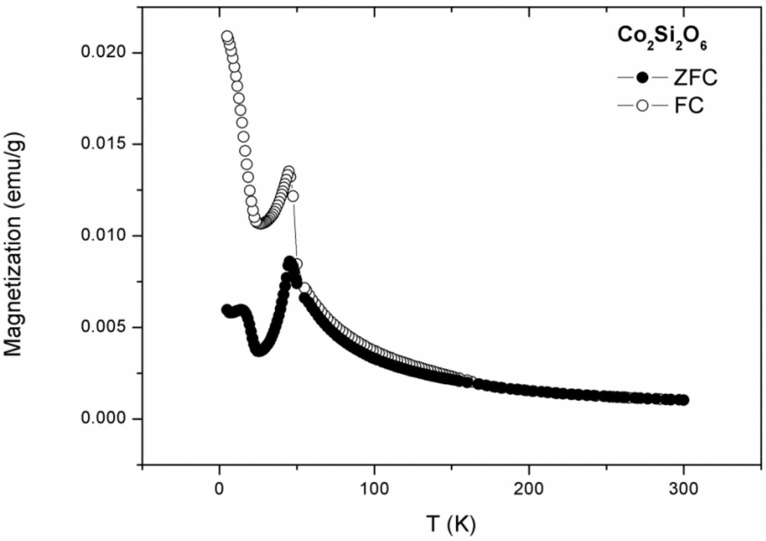

***Figure 5.1:** M(T) of $CaCoSi_2O_6$ (top) and $Co_2Si_2O_6$ (bottom).*

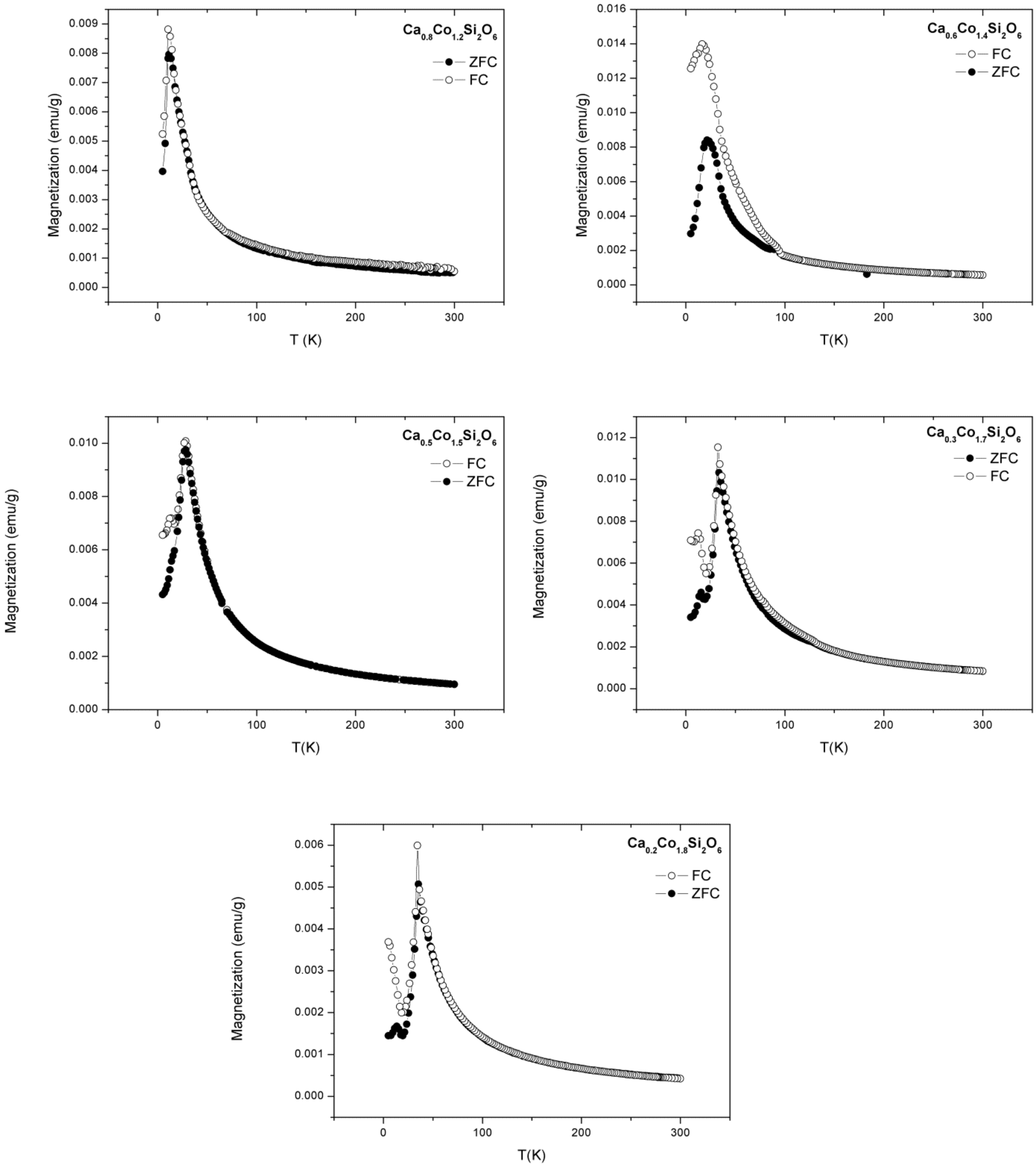

Figure 5.2: M(T) at 10 Oe of the solid solutions along the join: $Ca_{0.8}Co_{1.2}Si_2O_6$, $Ca_{0.6}Co_{1.4}Si_2O_6$, $Ca_{0.5}Co_{1.5}Si_2O_6$, $Ca_{0.3}Co_{1.7}Si_2O_6$, $Ca_{0.2}Co_{1.8}Si_2O_6$.

The substitution of Co for Ca causes a gradual broadening of the antiferromagnetic cusp at higher temperatures (Figure 5.3), which increases as far as the disorder on the M2 site increases. Furthermore, the position of this magnetic peak is shifted at higher temperatures with the increase of the cobalt concentration (moving from 16 K to 36 K approximately) because the magnetic interaction is stronger.

On the other hand, the low temperature transition does not change its position being related to the M1 intrachain interaction (Figure 5.3). Therefore, when the cobalt concentration on the M2 site is enough to stabilize a macroscopic magnetic signal, a new magnetization maximum arises (with 1.5 Co a.p.f.u.) and rapidly increases (see samples Co7, Co8 and Co10*)* (Figure 5.2), clearly suggesting the final formation of two superimposed and independent magnetic phases.

This result is confirmed by the structural transition from a *C*2/*c* to *P*2_1/*c* space group symmetry due to an increase of the cobalt concentration on the M2 site. This symmetry lowering is related to a strong tetrahedral tilting of the chains induced by the presence of a small cation Co and, at the same time, perfectly reproduced from the magnetic point of view by the formation of a novel magnetic phase and enhancement of the magnetic complexity.

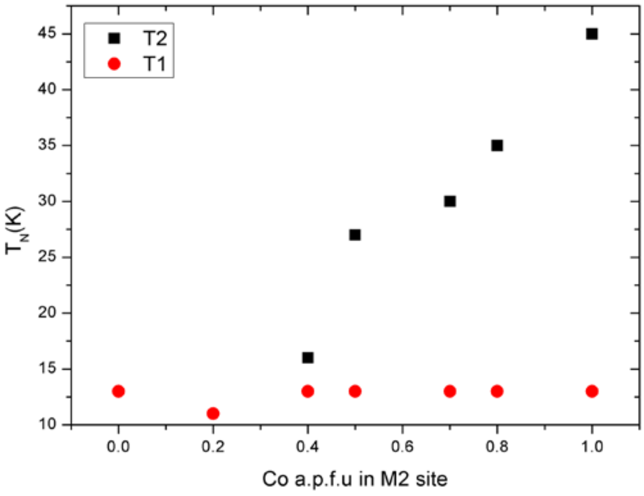

Figure 5.3: the evolution of the magnetic transition temperature along the studied join at 10 Oe.

5.3.2 Thermal Magnetization in High Field Conditions (5000 Oe)

A high external field applied during the ZFC/FC protocol makes negligible weak contributions to the magnetization as for instance diamagnetism, weak ferromagnetism, with respect to the primary magnetic responses (ferro, ferri and antiferro-magnetism).

In the present case (Figure 5.4) we observe a strong simplification of the thermal magnetization if compared to Figures 5.1 and 5.2.

All curves reported in Figure 5.4 show the typical AFM trend expected for a pellet sample, evidencing also the same critical temperatures detected in the low field case.

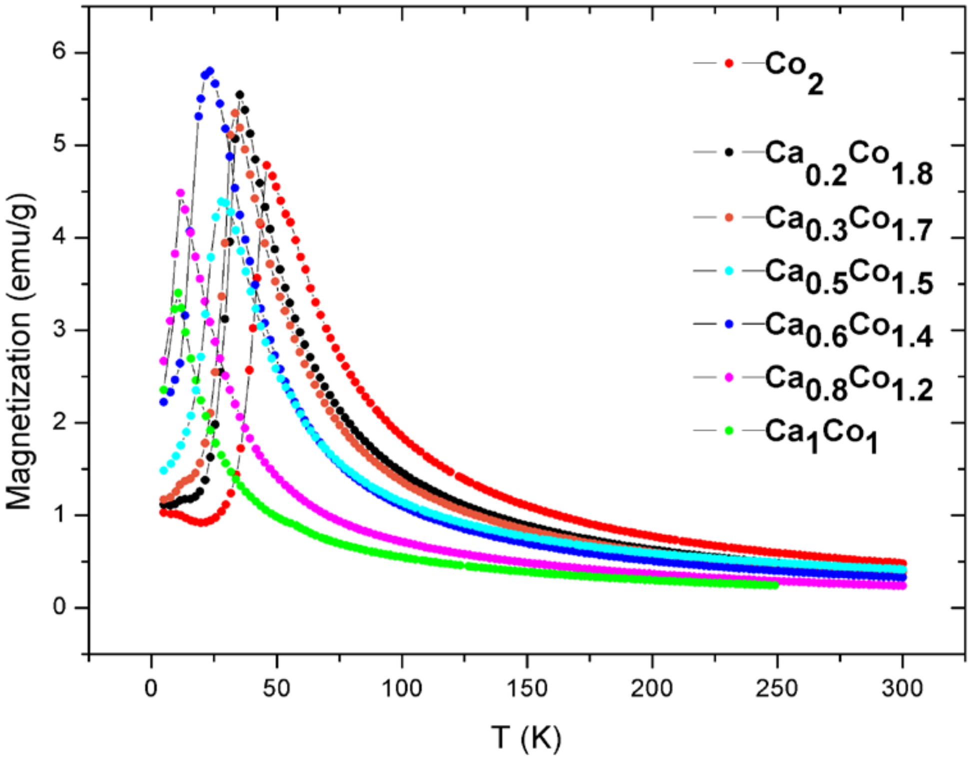

Figure 5.4: M(T) ZFC at 5000 Oe of all samples.

The main difference with respect to the spontaneous magnetization is a reduction of the low-T weak ferromagnetic contribution driven by the symmetrizing action of the magnetic field upon the non collinear intra-chain arrangement of the cobalt on the M2 site. Also for this reason, the two independent magnetic sublattices become indistinguishable (Figure 5.5).

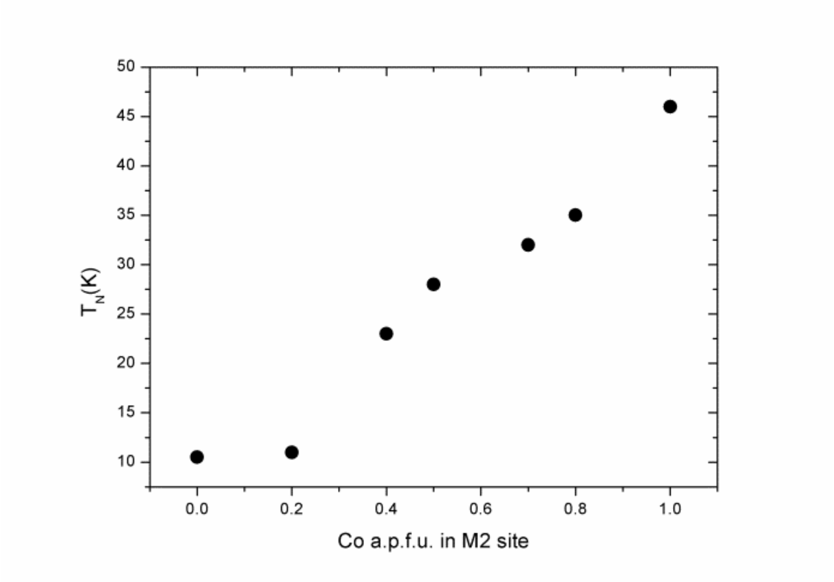

Figure 5.5: the evolution of the magnetic transition temperature along the studied join at 5000 Oe.

Study of the paramagnetic region by the Curie Weiss law

The inverse magnetic susceptibility $1/\chi_{mass}$ curves in ZFC mode at 5K Oe show Curie-Weiss behaviour. By fitting a regression line according to the Curie-Weiss law to the data, following:

$$\frac{1}{\chi_{mass}} = \frac{T}{C_m} - \frac{\theta_P}{C_m}$$

with χ_{mass} = the magnetic susceptibility, C_m = the Curie constant, and θ_P = the paramagnetic Curie temperature, C_m and θ_P can be extracted. The temperature, from which the linear fit starts, was chosen in generally above 100 K, but for each sample was determined looking carefully at the $1/\chi_{mass}$ curves. In Figure 5.6 the typical $1/\chi_{mass}$ curves of two different magnetic behaviours are displayed: $CaCoSi_2O_6$ shows the typical positive intercept of an antiferromagnet, while $Co_2Si_2O_6$ a negative intercept, evidencing the ferromagnetism of the sample.

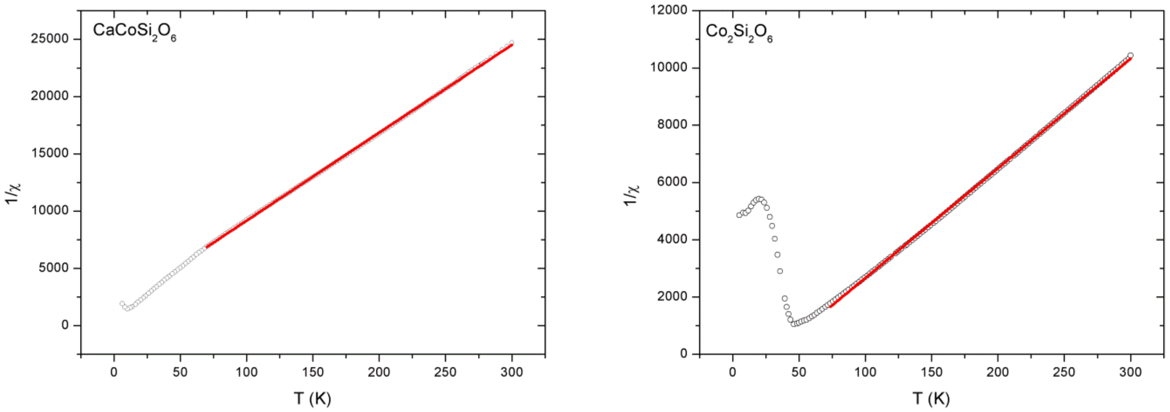

Figure 5.6: inverse of magnetic susceptibility of $CaCoSi_2O_6$ (on the left) and $Co_2Si_2O_6$ (on the right). The red line is the linear fit of the data, from which it is possible to calculate the C_m = the Curie constant and θ_P = the paramagnetic Curie temperature.

The number of Bohr magnetons (ρ_{eff}) can be calculated in the paramagnetic phase of a material by the value of the Curie-Weiss constant (C_m):

$$\rho_{eff} = \sqrt{\frac{PM * C_m * 3 * K_B}{N_A * z * \mu_B^2}} * \mu_B$$

where K_B is the Boltzmann constant ($1.38 * 10^{-16}$ J K^{-1}), N_A the Avogadro number ($6.023 * 10^{+23}$ mol^{-1}), μ_B the Bohr magneton ($9.27 * 10^{-21}$ J T^{-1}), PM the molecular weight, and z = number of magnetic ions per formula unit.

The expected value of Bohr magnetons for Co^{2+} ion in high spin configuration, considering the quenching of the orbital moment L (spin-only magnetic moment) is 3.87 μ_B, while in presence of spin orbit coupling the expected value is included between 4.7 and 5.2 μ_B.

The experimental Bohr magneton values obtained by this fitting procedure were elaborated for each sample starting from the corresponding ZFC measurement collected at 5000 Oe. The results are given in Table 5.2.

Table 5.2: results of susceptibility and magnetization measurements on powder samples. θ is the paramagnetic Curie Temperature and the effective moment expressed by number of Bohr magnetons per magnetic ion.

Sample	**Chemical composition**	**θ (K)**	**Number of Bohr magnetons per magnetic ion (μ_B)**
Co0	$CaCoSi_2O_6$	-16.1 ± 3	5.13
Co2	$Ca_{0.8}Co_{\mathbf{0.2}}Co_1Si_2O_6$	-12.59 ± 3	4.90
Co4	$Ca_{0.6}Co_{\mathbf{0.4}}Co_1Si_2O_6$	-10.55 ± 3	5.28
Co5	$Ca_{0.5}Co_{\mathbf{0.5}}Co_1Si_2O_6$	8.97 ± 3	5.3
Co7	$Ca_{0.3}Co_{\mathbf{0.7}}Co_1Si_2O_6$	16.56 ± 3	5.0534
Co8	$Ca_{0.2}Co_{\mathbf{0.8}}Co_1Si_2O_6$	28.4 ± 3	4.99
Co10	$Co_{\mathbf{1}}Co_1Si_2O_6$	31.83 ± 3	5.29

All the investigated samples are compatible with the presence of Co^{2+} in high spin configuration and with a strong spin-orbit coupling with a mean value of 5.2 μ_B.

Furthermore, the calculated θ temperatures plotted as a function of the Co content on the M2 site (Figure 5.7) suggest the presence of weak magnitude of the exchange integrals of the long range magnetism both along the M1 and M2 intra-chains, since very small magnitude of the θ detected for all samples.

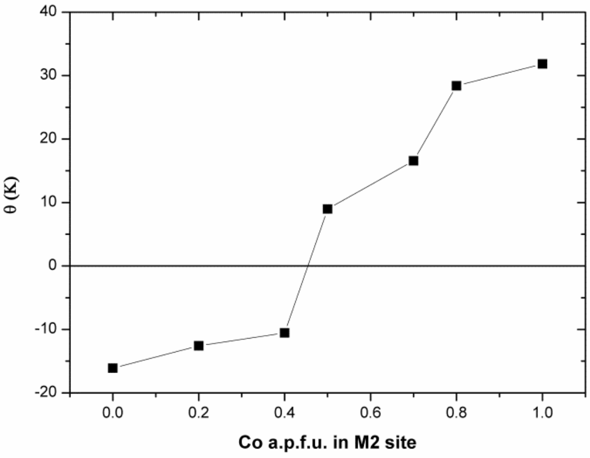

Figure 5.7: magnetic behaviour of the pyroxene join: the paramagnetic Curie temperature vs the amount of cobalt in M2 site.

However, the change of the θ sign above the 50% of the Co content on the M2 site is the marker of the new order incoming on the quasi-monodimensional M2 intrachain and so of the space symmetry change already discussed. The monodimensionality of the magnetism in these pyroxene compounds can be justified by looking at the low magnitude of the resultant magnetization (tending to zero for all the phases) (Coey and Ghose, 1988).

5.3.3 M(H) Characterization Hysteresis Loop

The hysteresis loop characterization of the join, performed at 5 KOe, clearly shows an AFM response.

The system confirms, in low field conditions, the features and the hypotheses pointed out by means of the magnetization study. The global intrinsic response of the material is AFM (Figure 5.8). This is clearly depicted in the shape and in the field dependence of the magnetization below one Tesla for the studied samples, where a predominant linear trend with negligible residual magnetization at H = 0 is measured.

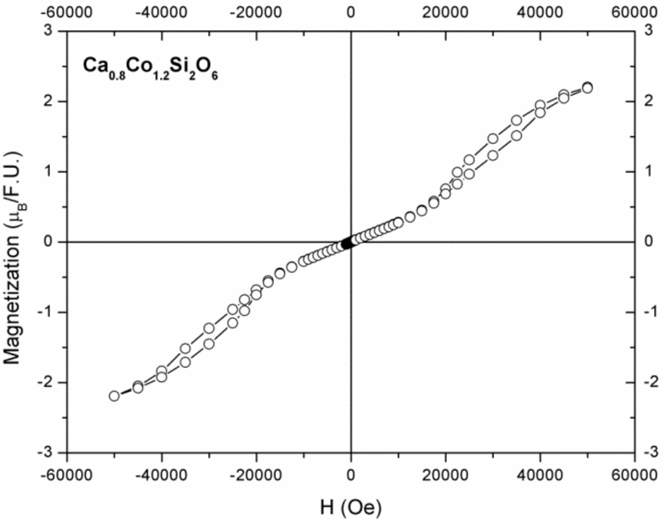

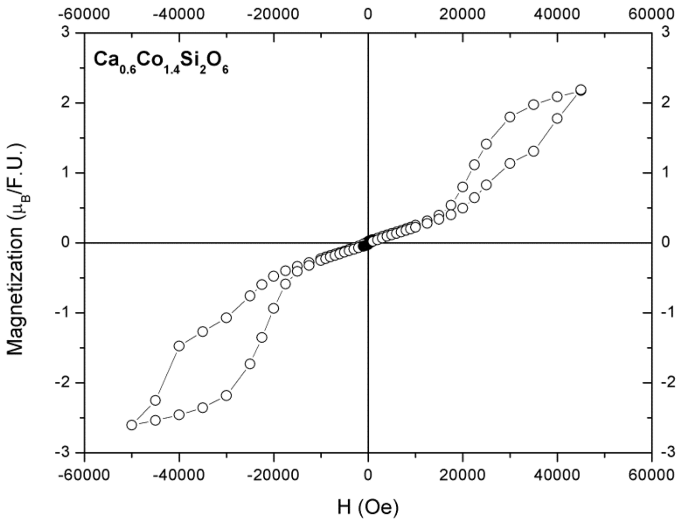

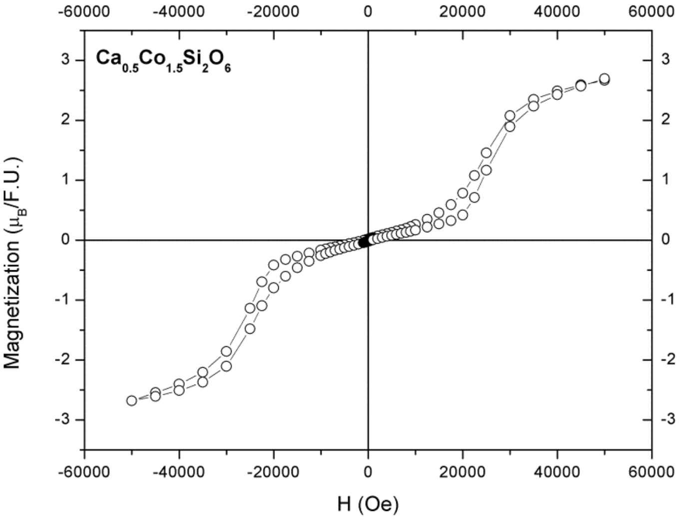

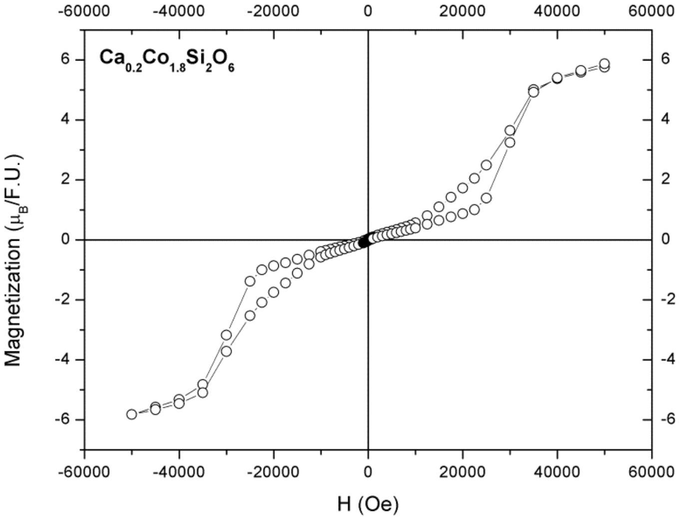

Figure 5.8: hysteresis loop of $Ca_{0.8}Co_{1.2}Si_2O_6$ (in the previous page), $Ca_{0.6}Co_{1.4}Si_2O_6$, $Ca_{0.5}Co_{1.5}Si_2O_6$ and $Ca_{0.2}Co_{1.8}Si_2O_6$.

The second peculiar characteristic is the spin-flop mechanism (AFM to FM continuous transition) with the expected opening of two ferromagnetic minor loops centered in symmetric position with respect to the graph origin (Figure 5.9).

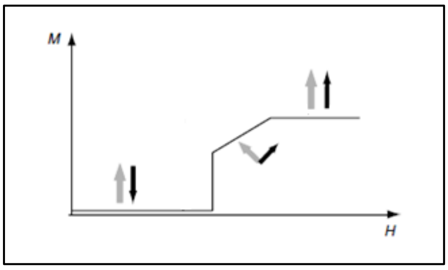

Figure 5.9: magnetization of an antiferromagnet as a function of applied magnetic field showing a spin flop transition (from Coey and Ghose, 1988).

This phenomenon is typical of systems in which the antiferromagnetic interactions are very weak. In addition, the singular field of the spin-flop process depends on the Co concentration on the M2 site: the higher the concentration, the higher the field necessary to break the antiparallel arrangement of the spins.

Another peculiar aspect of the hysteresis loop is related to the extrapolation of the saturation magnetization.

After the spin flop process, at fields higher than 4 T, all the curves seem to flatten getting closer to the saturation. When the long range magnetic order on the M2 site appears, for Co concentration higher than Co5, the observed value, expressed in Bohr magnetons, doubles. This means that the spin flop process involves also the AFM Co-O-Co chain on the M2 site as well as the AFM Co-O-Co on the M1 site.

The values at 5 T suggest also a quenching of the orbital momentum (spin only value) at 5 K contrary to what observed for the paramagnetic region. This is deduced by looking at the magnitude of the magnetization that tends to 3.87 for Co2, Co4 and Co5 while tends to 3.87*1.8 (number of magnetic ions per formula unit) for Co8.

Finally, looking at the zoomed region around H=0 (Figure 5.10), we are able to evidence also the weak ferromagnetism observed for the samples with higher Co content by means of the thermal magnetic characterization reported in the previous section.

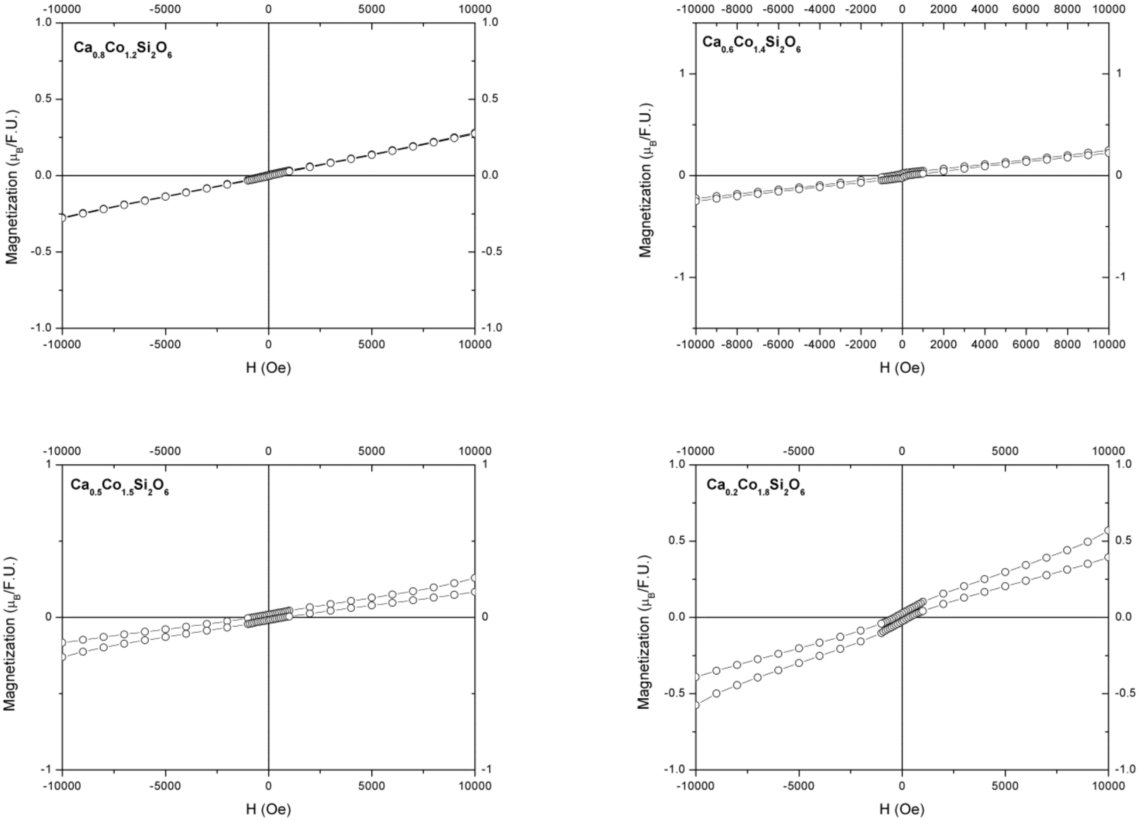

Figure 5.10: zoom of the hysteresis loop between -1T and 1 T of all samples along the join.

Looking at Figure 5.10, we notice that Co2 exhibits almost pure antiferromagnetic trend due to the unique contribution of Co^{2+} in M1 site (intra-chain interaction) which is collinear. On the other hand, Co8 is characterized by a weak ferromagnetic contribution with very low spontaneous magnetization (typical value of a weak ferromagnetism arising from a non-collinear arrangement of the AFM spins) superimposed to the antiferromagnetism. This causes the opening of the curve around zero and the linearity is lost. The presence of two independent AFM lattices is confirmed.

Consequently, our system could be described by two independent magnetic lattices due to the predominant intrachain interactions with respect to the interchain ones.

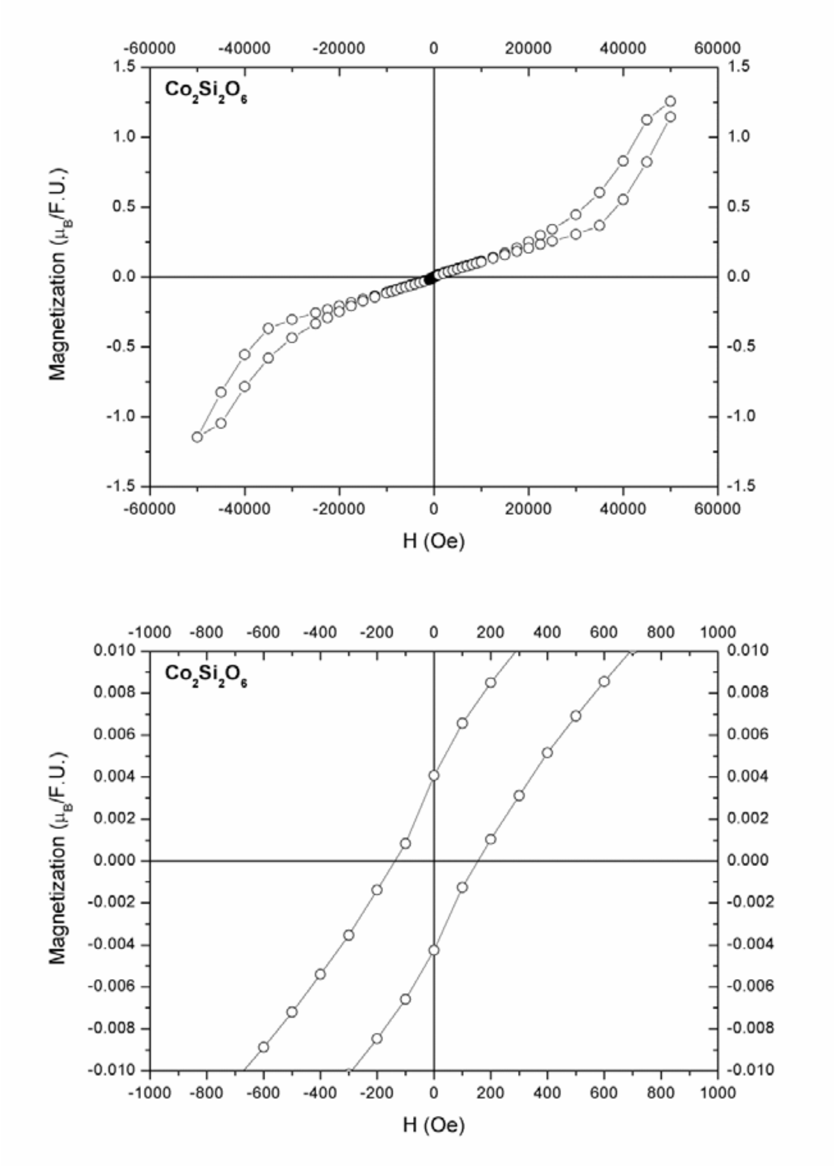

Figure 5.11: hysteresis loop of $Co_2Si_2O_6$ (top) and zoom of the hysteresis loop between -1T and 1 T (bottom).

The weak ferromagnetism is evident in $Co_2Si_2O_6$ sample (Figure 5.11), where the low field hysteretic behaviour appears more defined. As expected for Co10, the energy required for promoting the spin-flop process is the highest. Therefore, in this case, the flattening process is not visible (being just in the point of derivative maximum at 5 T). The predicted saturation magnetization for this system is consequently 3.87+3.87 μ_B, considering the complete rotation of the two AFM orders. The spin flop process was detected in other pyroxenes, like $Fe_{0.87}Mg_{0.13}SiO_3$ (Wiedenmann et al., 1986) where, applying a critical field $H_{c,}$ the antiferromagnetic ordering state changes directly to a parallel spin alignment.

In conclusion, the presence of this spin-flop process suggests that the AFM interactions are weak as expected for materials with monodimensional magnetism.

5.4 Discussion

Natural silicates, as pyroxene, often contain small amounts of 3d transition metal TM ions in octahedral sites (M2 and M1 sites), which possess a magnetic moment due to unpaired 3d electrons. When the concentration of 3d ions is sufficiently high to activate a magnetic coupling via exchange interactions, there may be a phase transition to a collective, magnetically ordered state at low temperatures (Coey and Ghose, 1988). Factors that impede high magnetic ordering temperatures are: the relatively low density of magnetic ions in silicates, as compared to oxides, the tendency for transition metal to occupy edge-sharing octahedra in silicate structures with near-90° TM-0-TM bond angles, which lead to weak superexchange interactions, and the low spatial dimensionality of the basic magnetic units, as the octahedral chains (Coey and Ghose, 1988).

The basic structural units of pyroxenes are infinite chains of edge-shared M1 octahedra, running parallel the crystallographic *c*-axis that may contain first row transition metals. Attached to these chains are the so-called M2 sites, which are 5- to 8-fold coordinated by oxygen, depending on the nature of the M2 cation and temperature/ pressure. These strips of M1/M2 polyhedra are interconnected via the corner-shared tetrahedral chains, also running parallel to the crystallographic *c*-axis (Figure 5.12) (Redhammer et al., 2010).

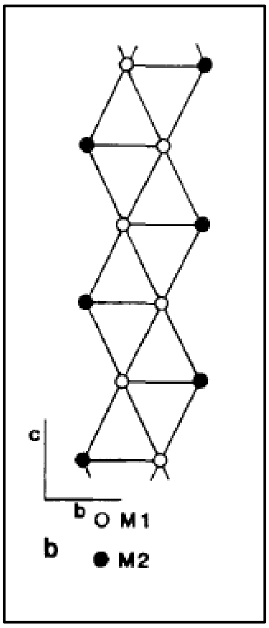

Figure 5.12: metal sites in pyroxenes along cb plane from Redhammer et al., (2010).

Pyroxenes cover a broad class of materials and have shown a variety of different magnetically ordered states. The variety of magnetic ground states found in pyroxene class is large, with compounds with pure antiferromagnetic interactions in and between the M1 chains as in $CaMnGe_2O_6$ (Redhammer et al., 2008), pure ferromagnetic interactions as in $NaCrGe_2O_6$ (Nenert et al., 2009), mixtures between the two, modulated magnetic structure and even compounds with spin-gap behaviour as in $NaTiSi_2O_6$ (Redhammer et al., 2008). The variety of magnetic properties is connected to the features of the crystal structure which allows the existence of competing magnetic exchange interactions.

The quite open architecture of the pyroxene structure allows tailoring geometry and distances within and between the M1 chains by chemical substitutions on M2 and tetrahedral sites while keeping the type of a magnetic active transition metal on the M1 site unchanged. Thereby it is possible to introduce small alterations to the crystal structure, which, however, can cause drastic alterations in magnetic properties. This feature and the discovery of multiferroic behaviour by Jodlauk et al. (2007) have increased interest in pyroxenes also in the fields of solid state physics.

The aim of this study was to determine magnetic properties for this set of compositions from the solid-solution series, and to point out differences between the magnetic properties of other pyroxenes. This offers new magnetic exchange pathways, not studied in detail so far. Furthermore, it was our intention to retrieve at least qualitative information about the nature of the short-range magnetic interactions within the octahedral chains as well as of the long-range order between the ribbons. In addition we intended to quantify the relationships which were expected to exist between the various magnetic parameters and composition (Eeckhout et al., 2001).

In literature, magnetic studies within a solid solution in pyroxenes are not so frequent. Wiedenmann et al. (1986) studied the orthopyroxenes $FeSiO_3$ and $Fe_{0.87}Mg_{0.13}SiO_3$. Eeckhout et al., (2001) investigated the magnetic properties of synthetic $P2_1/c$ (Mg-Fe)SiO_3 clinopyroxenes.

Concerning our solid solution, from the magnetic characterization we can conclude that all the samples may be described by monodimensional long range intrachain antiferromagnetism, due to the cobalt ions always present in M1 site. Another site (M2), in some cases, is involved in the system magnetism for a sufficiently high Co concentration.

Indeed, when the amount of cobalt is below 0.5 a.p.f.u in M2 site, a pure antiferromagnetic response is detected in all the measurements due to the intrachain M1 AFM Co-O-Co collinear interaction. When the cobalt begins to populate the M2 site, gradually a new intrachain order arises on the M2 site, but in this case the AFM Co-O-Co interactions are no more collinear due to the strong structural tetrahedra tilting. As a consequence, a weak ferromagnetism, superimposed to the antiferromagnetism, was detected both in the M(T) at 10 Oe and M(H). The weak ferromagnetism can be observed only for the samples with Co content higher than 0.5 a.p.f.u. in M2, or rather when the concentration is sufficiently high to create a long range order along the M2 chain which is magnetically independent by M1 chain.

In addition, the hysteresis loop measurements confirm the global antiferromagnetic nature of the samples. However, a clear spin-flop process from AFM to FM is observed at a relatively low field (~1.5 T). This mechanism confirms the weakness of the AFM interactions and the monodimensional nature of the magnetic system. Finally, pure spontaneous ferromagnetism does not exist in this join and it can be induced by an external magnetic field through a spin-flop process, even if the paramagnetic Curie temperature (θ) is positive for samples with an amount of cobalt higher than 1.4 a.p.f.u. This could be explained because the type of magnetic order is not simply determined by the sign of the principal exchange interactions (θ), but many silicates order antiferromagnetically despite the fact that their principal exchange interaction is ferromagnetic (Coey and Ghose, 1988).

The average Si-O_{br} bond length, the chain-kinking angle (O3-O3-O3), the average M(1)-O and M(2)-O bond lengths, the M1-M1 and M2-M2 distances influence the magnetic properties within the join. These changes most probably affects the magnetic interaction, as Redahmmer reported for $CaCoGe_2O_6$ (Redhammer et al., 2008), because even small structural, geometric adjustments can cause distinct differences in the magnetic exchange coupling. These changes need to be taken into account in any theoretical treatment of these low-dimensional systems (Redahmmer et al., 2012).

This is the reason why in literature the magnetic studies of a join are not so frequent. However, our end-members $CaCoSi_2O_6$ and $CoCoSi_2O_6$ were studied by Durand et al. (1996) and Sawaoka et al. (1968) respectively. Concerning the calcium pyroxene, the data agree with the literature: the Néel temperature is 10 K and θ is -28 K, while from this work T_N = 13 K and θ = -16 K. For $CoCoSi_2O_6$, Sawaoka et al. (1968) determined a Néel temperature of 50 K and θ +10 K; in our experiments this sample is characterized by two transition temperatures in the M(T) at low field (13 and 45 K) while at high field the data agree with those of literature.

The structure of the analogues Ge pyroxenes, $CaCoGe_2O_6$ and $Co_2Ge_2O_6$ (both in monoclinic (*C*2/*c*) and orthorhombic form), are also known (Redhammer et al., 2008 and 2010 respectively). The calcium pyroxene has positive θ = 20 K, evidence of a strong FM interaction within the M1 chain, which dominates the AFM coupling between the chains. The monoclinic form of $Co_2Ge_2O_6$ orders magnetically below 36 K with a small negative paramagnetic Curie temperature θ_P = - 4.6(2) K. The magnetic structure can be described with a ferromagnetic spin arrangement within the chains of M1 sites, but a dominating antiferromagnetic coupling between the chains. The orthorhombic phase displays transforms to an antiferromagnetically ordered state θ_P = -18.6(2) K below 33 K. The magnetic spin structure is similar to the one of the *C*2/*c* phase except that it is non-collinear in nature, i.e. there are components of the magnetic moment along all three crystallographic axes.

This is the comparison within the end member and if we focus our attention on the join we can affirm that the peculiarity of our system is the presence of two transition temperatures in M(T) a low field in the curve of susceptibility.

$FeSiO_3$ displays also two transition temperatures (Sawaoka et al., 1968). The magnetic susceptibility data on $FeGeO_3$ (Redhammer et al., 2012) show again two maxima in their temperature dependence, one at ~47 K, the second around 12 K, indicative of two magnetic transitions in the compound.

Neutron data shows that for T < 45 K, $FeGeO_3$ orders magnetically, having a simple collinear structure, with space group *C*2/*c*, and with the spins aligned parallel to the crystallographic *b*-axis, both on M1 and M2. The coupling within the M1/M2 band is ferromagnetic, whereas between them it is antiferromagnetic. As the bulk magnetic measurements in the paramagnetic state revealed a dominating ferromagnetic coupling, the intra-chain interactions dominate the inter-chain interaction. At 12 K, additional magnetic reflections appear, revealing a second magnetic phase transition. Spins are rotated away from the *b*-axis toward the *a*-*c* plane. The coupling within the M1 chain is still ferromagnetic and antiferromagnetic between the M1 chains. However, spins on M1 and M2, are no longer collinear. The moment on the M2 site is rotated further away from the *b*-axis than on M1 (Redhammer et al., 2012).

This mechanism might be the same for our compounds with antiferromagnetic behaviour within the chains, but the M(H) measurements indicate that the magnetic general response is antiferromagnetic, and the ferromagnetism arises from a non collinear structure of spins within the M2 chain. The strength of our study is based on different magnetic measurements, as M(T) at low and high field conditions and M(H). The combination of these techniques clarifies the magnetic behavior of the join and points out the differences, while in literature such study has never been done and the magnetic behavior is often predicted by high field thermal magnetization.

Additional experiments, for instance magnetic structure refinement with neutron diffraction of all samples, preferably on single crystals and measurement of the anisotropy of the susceptibility or magnetization in different directions on single crystals, could provide information on the crystal field interaction and are necessary for clarification on the magnetic behaviour, to understand all the mechanisms and to confirm our interpretation.

Chapter VI

CONCLUSIONS AND FUTURE DEVELOPMENTS

In this PhD study, the effects of the cation substitutions on the physical properties of pyroxenes have been discussed. The results of this work extend the knowledge on pyroxenes with different chemical compositions. These properties might be used in the development of ceramic pigments, advanced materials and for the mineralogical phase identification.

First of all, the crystallographic differences between Ge and Si pyroxenes have been examined.

The structure of *C*2/*c* Ca rich Ge clinopyroxenes is very close to the low pressure *C*2/*c* structural configuration found in Ca-rich Si-pyroxenes. The shear of the unit cell is very similar, and the difference between a Ge end member and the corresponding Si-rich one is less than 1°. Instead, a remarkable difference exists between Ca-poor Si and Ge clinopyroxenes. First, Ca-poor Ge pyroxenes do not display a $P2_1/c$ symmetry, but retain the *C*2/*c* symmetry; second, the observed *C*2/c structure shows, at room pressure, the configuration with highly kinked tetrahedral chains characteristic of the high pressure *C*2/*c* symmetry of Si Ca-poor pyroxenes.

In orthopyroxenes, with *Pbca* symmetry, Ge-pyroxenes have volume larger than Si-pyroxenes.

Samples along the system $CaCoGe_2O_6$ - $CoCoGe_2O_6$ have been synthesized at three different temperatures: 1050 °C, 1200 °C and 1250 °C. The aim of these solid state syntheses was to obtain a solid solution at ambient pressure, since the analogues Si-system needs high pressure. Unfortunately, very limited solution occurs because the structure forms of the two end member (high temperature for $CaCoGe_2O_6$ and high pressure $CoCoGe_2O_6$) are incompatible. The phase diagram of this system has been sketched and compared to that of Si. The cobalt end member ($CoCoGe_2O_6$) is stable at ambient pressure in two symmetries: at 1050 °C *C*2/*c* and 1200 °C *Pbca*. The impurity phase formed during these experiments is cobalt spinel.

Raman spectroscopy has been used to investigate the vibrational properties of Ca-pyroxenes $CaCoGe_2O_6$, $CaMgGe_2O_6$, $CaMgSi_2O_6$ and $CaCoSi_2O_6$.

A comparison between silicate and germanate pyroxenes shows significant changes in peak positions of the corresponding modes caused mainly by the difference of the Ge-Si atomic weight along with the distortion and compression of the coordination polyhedra. Red shift in Raman spectra of germanates has been calculated by a rough scale factor calculated by a simple harmonic oscillator model, considering the different bond lengths for 4-coordinated Si ~ 1.60- 1.65 Å *vs* Ge–O distance ~1.70 - 1.80 Å.

The Raman spectra of $CaMgGe_2O_6$ and $CaCoGe_2O_6$ have been classified, in analogy with silicate (Wang et al., 2001) counterparts, in different ranges:

- R1 (880-640 cm^{-1}): strong T-O stretching modes of Ge and non-bridging O1 and O2 atoms within the GeO_4 tetrahedron;
- R2 (640-480 cm^{-1}): stretching/bending modes of Ge-O_{br}-Ge bonds (chain stretching and chain bending);
- R4 (480-360 cm^{-1}): O-Ge-O vibrations;
- R3 (360-240 cm^{-1}): motions of the cations in M2 and M1 sites correlated with tetrahedral chain motion and tilting tetrahedra;
- R5 (below 240 cm^{-1}): lattice modes.

The largest shift with respect to $CaMgSi_2O_6$ - $CaCoSi_2O_6$ is shown by the T-O stretching and chain modes.

High-pressure Raman spectroscopy (up to about 8 GPa) on the same samples of Ca-pyroxenes using an ETH-type diamond anvil cell shows no phase transition within the *P*-ranges investigated, as all the peak positions vary linearly as a function of pressure. Our data confirm previous experimental findings on Si-diopside (Chopelas and Serghiou, 2000). In the investigated samples, all the Raman peaks shift upon compression, but the major changes in wavenumber with pressure are attributed to the chain bending (Ge-O_{br}-Ge bonds) and tetrahedra stretching modes (Ge-O_{nbr}). Upon compression, the kinking angle, the bond lengths and T-T distances between tetrahedra decrease and consequently the wavenumber of the bending chain mode and tetrahedra stretching mode increases. Ge-pyroxenes show the higher *P*-induced peak-position shifts, being more compressible than corresponding silicates.

The vibrational properties of $CaM^{2+}Ge_2O_6$ (M^{2+} =Mg, Mn, Fe, Co, Ni, Zn) are reported for the first time. The wavenumber of Ge-O_{br}-Ge bending modes decreases linearly with increasing ionic radius of the M1 cation. No simple correlation has been found with M1 atomic mass or size or crystallographic parameters for the peak at ~850 cm^{-1} and in the low wavenumber regions.

The magnetic properties of the system $CaCoSi_2O_6$ - $CoCoSi_2O_6$ have been investigated by magnetometry.

The join is always characterized by 1 a.p.f.u. of cobalt in M1 site and this causes a pure collinear antiferromagnetic behaviour of the intra-chain superexchange interaction involving Co ions detected in all the measurements, while the magnetic order developed by the cobalt ions in M2 site (intra-chain) is affected by weak ferromagnetism, due to the non-collinearity of their antiferromagnetic interaction. In magnetically ordered systems, this non-collinearity effect promotes a spin canting of anti-parallel aligned magnetic moments and thus is a source of weak ferromagnetic behaviour in an antiferromagnetic. The weak ferromagnetism can be observed only for the samples with Co content higher than 0.5 a.p.f.u. in M2, when the concentration is sufficiently high to create a long range order along the M2 chain which is magnetically independent of M1 chain. The ferromagnetism was detected both in the M(T) at 10 Oe and M(H).

Further possible investigations, regarding the system $CaCoGe_2O_6$ - $CoCoGe_2O_6$, might be the high pressure synthesis in order to achieve solid solution, and then the study of crystallographic structure and of the possible phase transitions. Furthermore, end-members could be evaluated as ceramic pigments through technological tests.

Concerning Raman spectroscopy, further insight via ab initio quantum mechanical calculations will help to understand the Ge peculiar behaviour with respect to Si and to identify the vibrational role of the cation in M1 site. In order to fully understand the HP Raman data, single crystal X-ray diffraction at high pressure will be needed.

Finally, neutron diffraction and consequent magnetic structure refinement might confirm the hypotheses of the magnetic behaviour in $CaCoSi_2O_6$ - $CoCoSi_2O_6$.

BIBLIOGRAPHY

- Angel R.J., Bujak M., Zhao J., Gatta G.D., Jacobsen S.D., (2007). *Effective hydrostatic limits of pressure media for high-pressure crystallographic studies*. Journal of Applied Crystallography, 40, 26.
- Arlt T., Angel R. J., (2000). *Displacive phase transitions in C-centred clinopyroxenes: spodumene,* $LiScSi_2O_6$ *and* $ZnSiO_3$. Physics and Chemistry of Minerals 27, 10, 719.
- Boyd F.R., Schairer J.F., (1964). *The System* $MgSiO_3$-$CaMgSi_2O_6$*.* Journal of Petrology, 5, 2, 275.
- Brown G. M., (1967). *Pyroxenes from the early and middle stages of fractionation of the Skaergaard Intrusion*. East Greenland. Mineralogical Magazine, 31, 511.
- Burnham C.W., Clark J.R., Papike J.J., Prewitt C.T., (1967). *A proposed crystallographic nomenclature for clinopyroxene structures*. Zeitschrift für Kristallographie - Crystalline Materials, 125, 125, 109.
- Burnham C. W., (1965). *Ferrosilite.* Carnegie Institution of Washington Year Book, 64, 202.
- Cameron M., Papike J.J., (1981). *Structural and chemical variation in pyroxenes.* American Mineralogist, 66, 1.
- Cameron M., Sueno S., Prewitt C. T., Papike J. J., (1973). *High-temperature crystal chemistry of acmite, diopside, hedenbergite, jadeite, spodumene and ureyite*. American Mineralogist, 58, 594.
- Chopelas A., Serghiou G., (2002). *Spectroscopic evidence for pressure-induced phase transitions in diopside.* Physics and Chemistry of Minerals, 29, 6, 403.
- Clark J. R., Appleman D. E., Papike J. J., (1969). *Crystal chemical characterization of clinopyroxenes based on eight new structure refinements*. Mineralogical Society of America Special Paper, 2, 31.
- Coey J. M. D., Ghose S., (1988). *Magnetic phase transitions in silicate minerals.* In Structural and Magnetic Phase Transitions in Minerals, pp. 162. Springer New York.
- Deer W.A., Howie R.A., Zussman J., (1978). *Rock-forming minerals. Vol 2A. Single chain silicate*. John Wiley, New York..
- Durand G., Vilminot S., Rabu P., Derory A., Lambour J.P., Ressouche E., (1996). *Synthesis, Structure, and Magnetic Properties of* $CaMSi_2O_6$*(M= Co, Ni) Compounds and Their Solid Solutions*. Journal of Solid State Chemistry, 124(2): 374.
- Eeckhout S. G., Grave E. D., Lougear A., Gerdan M., McCammon C. A., Trautwein A. X., Vochten R., (2001). *Magnetic properties of synthetic* $P2_1/c$ *(Mg-Fe)*SiO_3 *clinopyroxenes as observed from their low-temperature Mössbauer spectra and from SQUID magnetization measurements.* American Mineralogist, 86, 8-9, 957.

- Freed R. L., Peacor D. R., (1967). *Refinement of the crystal structure of johannsenite.* American Mineralogist, 52, 709.
- Furuhashi H., Inagaki M., Naka S., (1973). *Determination of cation distribution in Spinels by X-ray diffraction method*. Journal of Inorganic and Nuclear Chemistry, 35, 3009.
- Guyot F., Boyer H., Madon M., Velde B., Poirier J. P., (1986). *Comparison of the Raman microprobe spectra of* $(Mg, Fe)_2SiO_4$ *and* Mg_2GeO_4 *with olivine and spinel structures.* Physics and Chemistry of Minerals, 13, 2, 91.
- Gatta G.D., (2008). *Does porous mean soft? On the elastic behaviour and structural evolution of zeolites under pressure*. Zeitschrift für Kristallographie, 223, 160.
- Gatta G.D., (2010). *Extreme deformation mechanisms in open-framework silicates at high pressure: Evidence of anomalous inter-tetrahedral angles.* Microporous and Mesoporous Materials, 128, 78.
- Goldschmidt V. M., Peters C. l., (1931). *Zur Geochemie des Galliums.* Nachrichten von der Gesellschaft der Wissenschaften zu Göttingen, Mathematisch-Physikalische Klasse, 184.
- Ghose S., Wan C., Okamura F.P., (1987). *Crystal structures of* $CaNiSi_2O_6$ *and* $CaCoSi_2O_6$ *and some crystal-chemical relations in C2/c clinopyroxenes.* American Mineralogist, 72, 375.
- Hawthorne F. C., Ito J., (1977). *Synthesis and crystal-structure refinement of transition-metal orthopyroxenes I: orthoenstatite and (Mg, Mn, Co) orthopyroxene*. Canadian Mineralogist, 15, 321.
- Hazen R. M., (1993). *Comparative Compressibilities of Silicate Spinels: Anomalous Behavior of* $(Mg, Fe)_2SiO_4$. Science-New York Then Washington, 259, 206.
- Huang E., Chen C. H., Huang T., Lin E. H., Xu J. A., (2000). *Raman spectroscopic characteristics of Mg-Fe-Ca pyroxenes.* American Mineralogist, 85, 4, 473.
- Hugh-Jones D.A., Woodland A.B., Angel R.J., (1994). *The structure of high-pressure C2/c ferrosilite and crystal chemistry of high-pressure C2/c pyroxenes*. American Mineralogist, 79, (11-12), 1032.
- Jodlauk S., Becker P., Mydosh J. A., Khomskii D. I., Lorenz T., Streltsov S. V., Hezel D. C., Bohatý L., (2007). *Pyroxenes: a new class of multiferroics.* Journal of Physics: Condensed Matter, 19, 43, 432201.
- Lambruschi E., Aliatis I., Mantovani L., Tribaudino M., Bersani D., Redhammer G. J., Lottici P. P., (2015). *Raman spectroscopy of* $CaM^{2+}Ge_2O_6$ $(M^{2+}=$ *Mg, Mn, Fe, Co, Ni, Zn) clinopyroxenes.* Journal of Raman Spectroscopy, 46,586.
- Larson A.C., Von Dreele R.B.G., (2000). *General Structural Analysis System (GSAS*). Los Alamos National Laboratory Report, LAUR: 86-748.
- Levien L., Prewitt C. T., (1981). *High-pressure structural study of diopside*. American

Mineralogist, 66, 3-4, 315.

- Levien L., Prewitt C. T., Weidner D. J., (1980). *Structure and elastic properties of quartz at pressure.* American Mineralogist, 65, 9-10, 920.
- Lindsley D.H., Munoz J.L., (1969). *Subsolidus relations along the join hedenbergite-ferrosilite.* American Journal of Science, 267, 295.
- Mantovani L., Tribaudino M., Dondi M., Zanelli C., (2015). *Synthesis and color performance of* $CaCoSi_2O_6$ *pyroxene, a new ceramic colorant.* Dyes and Pigments, 120, 118.
- Mantovani L., (2014). *Synthesis and characterization of* $CaCoSi_2O_6$ – $Co_2Si_2O_6$ *pyroxenes,* PhD Thesis, University of Parma.
- Mantovani L, Tribaudino M., Bertoni G., Salviati G., Bromiley G., (2014). *Solid solutions and phase transitions in* $(Ca,M^{2+})M^{2+}Si_2O_6$ *pyroxenes* (M^{2+} *= Co, Fe, Mg).* American Mineralogist, 99, 4, 704.
- Mantovani L., Tribaudino M., Aliatis I., Lambruschi E., Lottici P. P., Bersani D., (2014). *Raman spectroscopy of* $CaCoSi_2O_6$–$Co_2Si_2O_6$ *clinopyroxenes.* Physics and Chemistry of Minerals, 42, 3, 179.
- Mao H. K., Xu J., Bell P. M., (1986). *Calibration of the ruby pressure gauge to 800 kbar under quasi-hydrostatic conditions.* Journal of Geophysical Research, 91, 4673.
- Miletich R., Allan D. R., Kuhs W. F., (2000). *High-pressure single crystal techniques in High-temperature and high-pressure crystal chemistry.* Reviews in Mineralogy and Geochemistry, 41, 445.
- Morimoto, N., (1989) Nomenclature of pyroxenes. Canadian Mineralogist, 27: 143-156.
- Morimoto N., Appleman D.E., Evans Jr. H.T., (1960). *The crystal structures of clinoenstatite and pigeonites*. Zeitschrift für Kristallographie, 114, 120.
- Navrotsky A., Coons W.E., (1976). *Thermochemistry of some pyroxenes and related compounds*. Geochimica et Cosmochimica Acta 40, 1281.
- Nenert G., Isobe M., Ritter C., Isnard O., Vasiliev A.-N., Ueda Y., (2009). *Magnetic and crystal structures of the magnetoelectric pyroxene* $LiCrSi_2O_6$*.* Physical Review B: Condensed matter and materials physics, 79, 064416.
- Nenert G., Ritter C., Isobe M., Isnard O., Vasiliev A. N., Ueda Y., (2009). *Magnetic and crystal structures of the one-dimensional ferromagnetic chain pyroxene* $NaCrGe_2O_6$*.* Physical Review B, 80, 2, 024402.
- Nestola F., Redhammer G. J., Pamato M. G., Secco L., Dal Negro A., (2009). *High-pressure phase transformation in* $LiFeGe_2O_6$ *pyroxene.* American Mineralogist, 94, 4, 616.
- Ohashi Y., personal communications. *Re-study on Raman spectroscopy of* $(Ca,Mg)MgSi_2O_6$ *clinopyroxenes.*

- Ohashi H., Sekita M., (1982). *Raman spectroscopic study of the Si-O-Si stretching vibration in clinopyroxenes.* J. Japan. Assoc. Min. Petr. Econ. Geol., 77, 12, 455.
- Ohashi Y., Osawa T., (1981). *The correlation between the Si-O (bridging) distance and the frequency of the Si-O-Si stretching in clinopyroxenes.*,J. Japan. Assoc. Min. Petr. Econ. Geol. 76, 5, 172.
- Oreshonkov A. S., Gerasimova J. V., Ershov A. A., Krylov A. S., Shaykhutdinov K. A., Vtyurin A. N., Molokeev M. S., Terent'ev K. Y., Mihashenok, N. V., (2015). *Raman spectra and phase composition of* $MnGeO_3$ *crystals.* Journal of Raman Spectroscopy. DOI 10.1002/jrs.4816.
- Ozima M., (1983). *Structure of orthopyroxene-type and clinopyroxene-type magnesium germanium oxide* $MgGeO_3$. Acta Crystallographica, Section C: Crystal Structure Communications, 39, 1169.
- Papike J. J., Prewitt C. T., Sueno S., Cameron M., (1973). *Pyroxenes: comparisons of real and ideal structural topologies.* Zeitschrift fiir Kristallographie, 138, 254.
- Peacor D. R. (1968). *The crystal structure of* $CoGeO_3$*.* Zeitschrift für Kristallographie-Crystalline Materials, 126, (1-6), 299.
- Pearson D. G., Brenker F. E., Nestola F., McNeill J., Nasdala L., Hutchison M. T., Matveev S., Mather K., Silversmit G., Schmitz S., Vekemans B., Vincze L., (2014). *Hydrous mantle transition zone indicated by ringwoodite included within diamond.* Nature, 507, 7491, 221.
- Pommier C. J. S., (2003). *Raman spectroscopic study of pyroxenes and other minerals.* PhD thesis, University of Arizona.
- Prencipe M., Maschio L., Kirtman B., Salustro S., Erba A., Dovesi R., (2014). *Raman spectrum of* $NaAlSi_2O_6$ *jadeite. A quantum mechanical simulation.* Journal of Raman Spectroscopy, 45, 8, 703.
- Prencipe M., Mantovani L., Tribaudino M., Bersani D., Lottici P. P., (2012). *The Raman spectrum of diopside: a comparison between ab initio calculated and experimentally measured frequencies.* European Journal of Mineralogy, 24, 3, 457.
- Prencipe M., Tribaudino M., Pavese A., Hoser A., Reehuis M., (2000). *A single-crystal neutron-diffraction investigation of diopside at 10 K.* The Canadian Mineralogist, 38, 1, 183.
- Prewitt C.T, (1980). *Pyroxenes*. Reviews in Mineralogy, Vol. 7, Mineralogical Society of America.
- Putnis, A., (1992). *An introduction to mineral science*. Cambridge University Press.
- Redhammer G. J., Roth G., Senyshyn A., Tippelt G., Pietzonka C., (2013). *Crystal and magnetic spin structure of Germanium-Hedenbergite,* $CaFeGe_2O_6$ *and a comparison with other magnetic/magnetoelectric/multiferroic pyroxenes.* Zeitschrift für Kristallographie - Crystalline Materials, 228, 3, 140.

- Redhammer G. J., Senyshyn A., Tippelt G., Pietzonka C., Treutmann W., Roth G., Amthauer G., (2012). *Magnetic and low-temperature structural behavior of clinopyroxene-type $FeGeO_3$: A neutron diffraction, magnetic susceptibility, and ^{57}Fe Mössbauer study.* American Mineralogist, 97, 4, 694.
- Redhammer G.J., Nestola F., Miletich R., (2012). *Synthetic $LiAlGe_2O_6$: The first pyroxene with $P2_1/n$ symmetry.* American Mineralogist, 97, 7, 1213.
- Redhammer G. J., Senyshyn A., Tippelt G., Roth G., (2011). *Magnetic spin structure of pyroxene-type $MnGeO_3$*. J. Phys.: Condens. Matter, 23, 254202.
- Redhammer G. J., Senyshyn A., Tippelt G., Pietzonka C., Roth G., Amthauer G., (2010). *Magnetic and nuclear structure and thermal expansion of orthorhombic and monoclinic polymorphs of $CoGeO_3$ pyroxene.* Physics and Chemistry of Minerals, 37, 5, 311-332.
- Redhammer G. J., Cámara F., Alvaro M., Nestola F., Tippelt G., Prinz S., Simons J., Roth G., Amthauer G. (2010). *Thermal expansion and high-temperature $P2_1/c$–$C2/c$ phase transition in clinopyroxene-type $LiFeGe_2O_6$ and comparison to $NaFe(Si,Ge)_2O_6$.* Physics and Chemistry of Minerals, 37*, 10, 685.*
- Redhammer G. J., Roth G., Treutmann W., Paulus W., André G., Pietzonka C., Amthauer G., (2008). *Magnetic Ordering and Spin Structure in Ca-Bearing Clinopyroxenes $CaM^{2+}(Si, Ge)_2O_6$, M=Fe, Ni, Co, Mn.* Journal of Solid State Chemistry, 181, 11, 3163.
- Redhammer G. J., Amthauer G., Roth G., Tippelt G., Lottermoser W., (2006). *Single-crystal X-ray diffraction and temperature dependent 57Fe Mössbauer spectroscopy on the hedenbergite-aegirine $(Ca,Na)(Fe^{2+},Fe^{3+})Si_2O_6$ solid solution.* American Mineralogist, 91, 8-9, 1271.
- Redhammer G. J., Roth G., (2005). *A comparison of the clinopyroxene compounds $CaZnSi_2O_6$ and $CaZnGe_2O_6$*. Acta Crystallographica Section C61, i20.
- Rietveld H., (1969). *A profile refinement method for nuclear and magnetic structures.* Journal of Applied Crystallography, 2, 2, 65.
- Ringwood A. E., (1975). *Composition and petrology of the earth's mantle*. McGraw-Hill international series in the earth and planetary sciences.
- Ringwood A. E., Seabrook M., (1963). *High-pressure phase transformations in germanate pyroxenes and related compound*s. J. Geophys. Res., 68, 4601.
- Rutstein M. S., White W. B., (1971). *Vibrational spectra of high-calcium pyroxenes and pyroxenoids.* American Mineralogist, 56, 5-6, 877.
- Sawaoka A., Miyahara S., Akimoto S. I., (1968). *Magnetic properties of several metasilicates and metagermanates with pyroxene structure*. Journal of the Physical Society of Japan, 25, 5, 1253.
- Serghiou G., Chopelas A., Boehler R., (2000). *Explanation of pressure-induced*

transformations in chain silicates based on their modular structures. Journal of Physics: Condensed Matter, 12, 42, 8939.

- Shannon R., (1976). *Revised effective ionic radii and systematic studies of interatomic distances in halides and chalcogenides*. Acta Crystallographica Section A, 32, 5, 751.
- Stishov S. M., (1995). *Memoir on the discovery of high-density silica.* International Journal of High Pressure Research, 13, 5, 245.
- Stishov S. M., Popova S. V., (1961). *Geokhimiya*.
- Sueno S., Cameron M., Prewitt C. T., (1976). *Orthoferrosilite: high temperature crystal chemistry*. American Mineralogist, 61, 38.
- Tauber A., Kohn J. A., (1965). *Orthopyroxene and clinopyroxene polymorphs of* $CoGeO_3$. American Mineralogist 50, 1-2, 13.
- Tribaudino M., Mantovani L., Bersani D., Lottici P.P., (2012). *Raman spectroscopy of* $(Ca,Mg)MgSi_2O_6$ *clinopyroxenes*. American Mineralogist, 97, 1339.
- Tribaudino M., Nestola F., Meneghini C., (2005). *The structure behaviour of intermediate pyroxenes along the diopside-enstatite join.* Canadian Mineralogist, 43, 1411.
- Tribaudino M., Prencipe M., Nestola F., Hanfland M., (2001). *A* $P2_1/c$-$C2/c$ *high-pressure phase transition in* $Ca_{0.5}Mg_{1.5}Si_2O_6$ *clinopyroxene.* American Mineralogist, 86, 7-8, 807.
- Tribaudino M., Prencipe M., Bruno M., Levy D., (2000). *High pressure behaviour of Ca-rich C2/c clinopyroxenes along the join diopside-enstatite* $(CaMgSi_2O_6$-$Mg_2Si_2O_6)$*.* Physics and Chemistry of Minerals, 27, 656.
- Wang Y., Song J., Gies H., (2003). T*he substitution of germanium for silicon in AST-type zeolite*. Solid state sciences, 5, 11, 1421.
- Wang A., Jolliff B.L., Haskin L.A., Kuebler, K.E., Viskupic K.M., (2001). *Characterization and comparison of structural and compositional features of planetary quadrilateral pyroxenes by Raman spectroscopy.* American Mineralogist, 86, 7-8, 790.
- Wiedenmann A, Regnard J.R., Fillion G., Hafner S. S., (1986). *Magnetic properties and magnetic ordering of the orthopyroxenes* $Fe_XMg_{1-x}SiO_3$ J. Phys. C: Solid State Phys., 19, 3683.
- Yang H., Finger L.W., Conrad P.G., Prewitt C.T., Hazen R.M., (1999). *A new pyroxene structure at high pressures: Single crystal X-ray and Raman study of the* $Pbcn$-$P2_1cn$ *phase transition in protopyroxene.* American Mineralogist, 84, 245.
- Zhang L., Ahsbahs H., Hafner S. S., Kutoglu A., (1997). *Single-crystal compression and crystal structure of clinopyroxene up to 10 GPa.* American Mineralogist, 82, 3, 245.

Acknowledgements

I would like to thank my supervisors, Prof. Pier Paolo Lottici and Prof. Mario Tribaudino.

I would like to acknowledge also Prof. Danilo Bersani, Professor Gunther Redhammer, Prof. Giacomo Diego Gatta, who worked with me during these years.

Thanks to Prof. Massimo Solzi and Chiara Pernechele for the magnetic measurements. I will be always grateful to Davide Delmonte for his special help for the interpretation of the magnetic data.

Special thanks to our pyroxene research group, in particular Luciana Mantovani, Claudia Gori and Claudia Stangarone.

My special thanks go to my dear colleague Irene Aliatis. I would like to thank her for support, ideas, technical suggestions, help, improvement, kindness, intelligence. I cannot imagine this experience without her presence and I will be always grateful to have met her.